博士論文

Estimation of entropy production by machine learning

（機械学習によるエントロピー生成の推定）

大坪　舜

Abstract

In the last two decades, our understanding of thermodynamics of small systems has developed substantially, being formulated as stochastic thermodynamics. For example, when a pulling experiment of a folded RNA is conducted, the dissipated work fluctuates from sample to sample even if the experimental condition is fixed. This is in contrast to conventional thermodynamics. To take such stochasticity into account, thermodynamic quantities are defined at the level of single realizations. This formulation has enabled us to discover universal laws that hold for nonequilibrium processes far from equilibrium.

Among such laws, a notable example is the fluctuation theorem, which states that the entropy production is the logarithm of the ratio between forward and backward transition probabilities, representing the time-reversal symmetry breaking. A closely related concept is information thermodynamics, which reveals the interplay between the thermodynamic entropy and information flow. Finally, yet another fundamental relation called the thermodynamic uncertainty relation (TUR) has been discovered recently. The TUR is a tradeoff relation between the entropy production and the fluctuation of currents, and thus gives a tight constraint on possible realization of currents.

On another front, living systems are primary examples where nonequilibrium is essential. Especially, cellular processes are often enhanced by nonequilibrium driving to perform their function. Recent developments in experiments enable us to observe such cellular activities at the level close to elementary stochastic processes. For example, primary cilia, hairlike organelles protruding from the surface of eukaryotic cells, show apparently random behavior. A recent study has shown that its nonequilibrium activity is detectable as circulating probability currents in some phase space mapped from the real space dynamics, and thus the motion of primary cilia is not thermal.

To quantify such nonequilibrium activity beyond the qualitative classification of thermal or active, the estimation of the entropy production is demanded. However, its estimation from experimental data is still not an easily tractable problem. For example, the estimation of the forward and backward transition probabilities requires full details of the stochastic dynamics, and thus the direct use of the fluctuation theorem is not practical.

The present thesis is devoted to develop a framework for estimating the entropy production solely on the basis of time-series data using variational approaches with machine learning. Especially, we consider to apply the TUR for the estimation. This approach has

been recently proposed, where the main idea is as follows: (i) view the TUR as an inequality that gives a lower bound on the entropy production, (ii) find an optimal current that maximizes the lower bound, and (iii) use the lower bound as an estimate of the entropy production. This variational approach is expected to be data efficient since it requires only the mean and the variance of a single fluctuating current. In addition, it has been numerically suggested that this method can give the exact estimate by taking the short-time limit of the optimizing current (the short-time TUR).

There are three fundamental remaining issues in the previous researches. First, the equality condition of the short-time TUR has not been analytically studied, and thus its range of applicability has been unclear. Second, only a few previous studies actually consider the maximization process in numerical setups that are applicable to practical situations. Third, its practical effectiveness is not well understood: for example, whether this approach works well at high-dimensional or non-stationary setups.

To overcome these issues and to go beyond, we present two main results in this thesis. In the first part, we resolve the above issues and develop a practical estimation method for stationary dynamics. In the second part, we theoretically reveal the relationship between several variational representations of the entropy production including the short-time TUR. Then, an estimation method for non-stationary dynamics is provided. Our method is of practical significance since all it requires are trajectory data without prior knowledge of the system parameters. In addition, we find that our method performs well even in high-dimensional, non-linear, and non-stationary dynamics. Below, we explain these points in more detail.

In the first part of this thesis, we formulate the short-time TUR and analytically study the equality condition. As a result, we show that the short-time TUR can give the exact estimate of the entropy production in overdamped Langevin dynamics, while this is not the case in general Markov jump processes. In addition, we show that the short-time TUR holds for the partial entropy production of subsystems under autonomous interaction, which reveals the hierarchy of the estimation when the optimizing currents are partially masked.

On the basis of the above theoretical result, we develop a practical estimator of the entropy production for overdamped Langevin dynamics in the stationary state by combining the short-time TUR with machine learning techniques such as the gradient ascent. The learning estimator works solely on the basis of trajectory data without requiring prior knowledge of the parameters of the underlying dynamics. We numerically demonstrate that the learning estimator performs well even in nonlinear and high-dimensional Langevin dynamics. We also discuss the estimation in Markov jump processes and develop a learning estimator for them. It is found that the learning estimator is robust against the choice of the sampling interval of trajectory data, while the exact estimation is shown to be impossible in general.

The estimation of the entropy production in non-stationary dynamics is yet another important but largely unexplored issue. In the second part of this thesis, we extend the learning algorithm developed in the first part to non-stationary dynamics. First, we establish the theoretical relationship between two variational representations of the entropy production: one is the short-time TUR, and the other is Neural Estimator for Entropy Production (NEEP) which has been proposed after the short-time TUR. Especially, we

show that the short-time TUR gives a tighter bound on the entropy production than the NEEP in Langevin dynamics by deriving an intermediate variational representation of them. In addition, we reveal that the NEEP is related to a dual representation of the Kullback-Leibler divergence, and show that the NEEP is also applicable to non-stationary dynamics.

Next, we develop an efficient algorithm for the non-stationary estimation on the basis of the variational representations. For the non-stationary estimation, an ensemble of trajectories sampled from repeated experiments is necessary, in contrast to the stationary case where a single long trajectory is enough. To take advantage of this setup, we propose a method that finds the optimal currents continuously in time using a feedforward neural network, namely using the optimal current at one time to help finding the optimal currents in the near time. Indeed, we numerically find that the estimate of our method converges not only by increasing the number of trajectories but also by increasing the number of time instances contained in each trajectory, which is of practical importance since preparing a large number of trajectories may not be easy.

Meanwhile, as a side issue to the foregoing main two results, we study information-thermodynamic efficiencies of F_1-ATPase (or F_1). F_1 is a molecular motor, which rotates and converts chemical energy into mechanical work reversibly and very efficiently. According to recent experiments, the F_1 keeps the internal heat dissipation close to zero. A theoretical study has shown that a reaction-diffusion model of the F_1 reproduces its energetics, suggesting that the feedback structure plays a certain role. Since a feedback usually entails information flow, F_1 is interesting from the information-thermodynamic perspective. However, a quantitative understanding of the interplay between heat dissipation and information flow has been lacking. In this thesis, we numerically study the information flow and the information-thermodynamic dissipation, which is a partial entropy production defined by heat dissipation minus information flow, on the basis of the reaction-diffusion model. We show that in the free rotation setup, the rotational degree of freedom plays a role of Maxwell's demon, which acquires information of the internal state. From this perspective, the small internal heat dissipation can be understood as a consequence of the feedback control by Maxwell's demon.

In summary, we have made a platform for applying machine learning to the estimation of the entropy production by variational methods. Our method has been shown to perform well even in high-dimensional, non-linear and non-stationary dynamics, and thus is applicable to a broad class of stochastic dynamics. Its application to real experimental data including biological ones is an important future issue. In addition, we have theoretically established the variational representations of the entropy production. We expect that these representations are useful for the future searching of universal laws regarding the entropy production far from equilibrium.

List of publication

This thesis is based on the following three publications:

1. S. Otsubo, S. Ito, A. Dechant, and T. Sagawa, "Estimating entropy production by machine learning of short-time fluctuating currents", Phys. Rev. E **101**, 062106 (2020).

2. S. Otsubo, S. K. Manikandan, T. Sagawa, and S. Krishnamurthy, "Estimating entropy production along a single non-equilibrium trajectory", arXiv:2010.03852 (2020).

3. S. Otsubo, S. Bo, C.-B. Li, and T. Sagawa, "Information thermodynamics of F_1-ATPase", Manuscript in preparation (2021).

The following publication is not directly related to this thesis.

4. S. Otsubo, and T. Sagawa, "Information-thermodynamic characterization of stochastic Boolean networks", arXiv:1803.04217 (2018).

Acknowledgements

I am very grateful to my supervisor Takahiro Sagawa. It has been a wonderful experience for me to work under his supervision as a PhD student, and I have learned a lot about doing research. Without his dedicate support and encouragement, this work would never have been accomplished.

I would like to thank all the members in our and neighboring groups for daily communications. I am grateful to Yuto Ashida and Eiki Iyoda for having a lot of short discussions and giving me advice on my research. Special thanks to Kazuya Kaneko and Hiroki Yamaguchi for their helps in so many situations of my graduate school life. I thank Shotaro Baba for setting up the computing environment. I also thank Sachiko Seto for her support in our research activities as a secretary of our group.

One of the happiest things I experienced was to meet great researchers from all over the world through Takahiro. First, I would like to thank all of my collaborators of this work. I am grateful to Sosuke Ito and Andreas Dechant for their kind support in the results of Chapter 5. I am grateful to Sreekanth K Manikandan and Supriya Krishnamurthy for many discussions and support in writing the paper for the results in Chapter 6. I am grateful to Chun-Biu Li and Stefano Bo for suggesting me to work on information thermodynamics of F_1-ATPase presented in Appendix A and having many discussions. For the third collaboration, Takahiro and I had an opportunity to visit Nordita in Stockholm. I appreciate a lot Chun-biu, Stefano, Joanna Tyrcha, and Sreekanth for their great hospitality during our stay. This stay let me realize that Sreekanth and I had a common research interest of the short-time TUR, leading to the second collaboration. I also thank Sreekanth for pleasant chats and discussions through a message app almost every week.

I would like to thank David H. Wolpert, Tan Van Vu, and Yoshihiko Hasegawa for having discussions when David visited us. I would like to thank Jo Junghyo and Changbong Hyeon for their great hospitality when I visited KIAS in Seoul. I thank Tetsuya J. Kobayashi, Tetsuhiro Hatakeyama, and Koichi Fujimoto for pleasant conversations and giving me inspiration on research during the stay. I would also like to thank Lei-Han Tang and his group members for their great hospitality when Takahiro and I visited CSRC in Beijing.

I greatly acknowledge the financial support by SEUT-RA, a research assistant program by School of Engineering, the University of Tokyo. I also thank office staffs of Applied Physics for their support in my graduate school life.

Finally, I would like to express my special thanks to my family and relatives for their continuous support and encouragement throughout my life.

Contents

Chapter 1

Introduction

First of all, we give a brief overview of the background of our research. Then, we summarize the outline of this thesis.

1.1 Background

Stochastic thermodynamics [1–6] is a recently developed framework for thermodynamics of small systems such as colloidal particles [7], quantum dots [8], molecular motors [9], and biochemical networks [10, 11]. In such small systems, thermodynamic quantities fluctuate due to thermal noise even if we repeat an experiment with the same protocol. Figure 1.1 shows an experiment [12] that repeatedly measures the dissipated work $W_{\rm diss} := W - \Delta G$ associated with the pulling of a folded RNA molecule. Here, W is the work done on the molecule, and ΔG is the free energy change. In conventional thermodynamics, $W_{\rm diss}$ takes a deterministic value when the protocol is fixed, and satisfies the second law of thermodynamics represented as $W_{\rm diss} \geq 0$. On the other hand, in the setup of stochastic thermodynamics, $W_{\rm diss}$ fluctuates from sample to sample, and occasionally takes even negative values as shown in Fig. 1.1(b). Given that, in stochastic thermodynamics, the second law is satisfied at the ensemble level, $\langle W_{\rm diss} \rangle \geq 0$, where the bracket denotes the ensemble average. To take such stochasticity into account, thermodynamic quantities are defined at the level of individual realizations, which enables us to explore the universal laws that hold in non-equilibrium processes far from equilibrium.

A notable example of such universal laws is the fluctuation theorem (or the Jarzynski equality) [1–3, 6, 12–14], which states that the entropy production S ($:= W_{\rm diss}/T$ with temperature T) satisfies the equality $\langle \exp(-S) \rangle = 1$, if the system is driven from equilibrium to far-from-equilibrium. This relation essentially comes from the fact that the entropy production can be written as the logarithm of the ratio between the forward and backward transition probabilities, which quantifies the breaking of time-reversal symmetry. The fluctuation theorem is regarded as a generalization of the second law including the higher-order statistics, and the second law $\langle S \rangle \geq 0$ can be derived by the convex inequality $\langle \exp(-S) \rangle \geq \exp\left(-\langle S \rangle\right)$.

As a closely related concept, information thermodynamics has attracted much attention recently [15–21]. Information thermodynamics has been originally considered in the

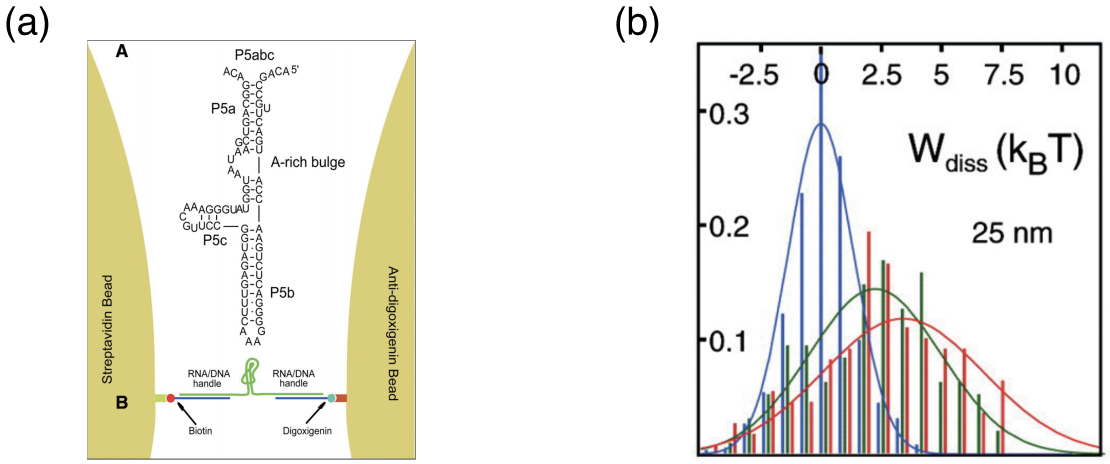

Figure 1.1: Pulling experiment of a folded RNA molecule. (a) Schematic of the experiment. An RNA hairpin is pulled by the two beads attached to it. (b) Histogram of the dissipated work with different pulling speeds from blue (slow) to red (fast). From Ref. [12] (DOI: 10.1126/science.1071152). Reprinted with permission from AAAS.

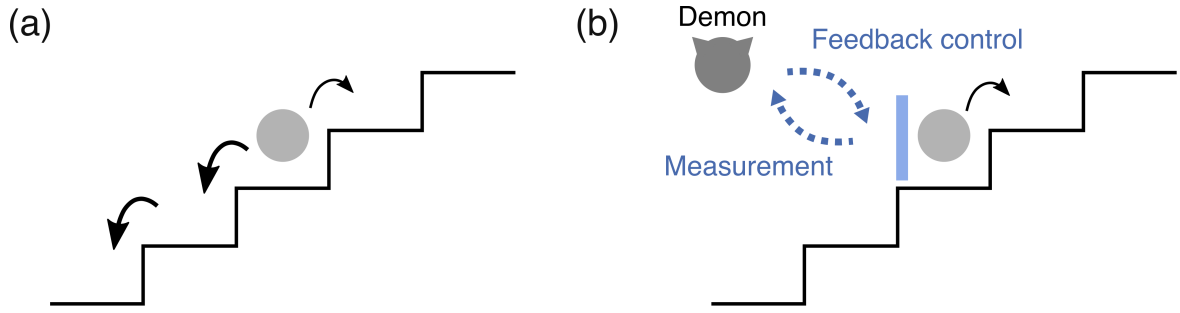

Figure 1.2: Schematic of Maxwell's demon. (a) Brownian particle under a staircase potential with the step height comparable to k_BT. The particle typically goes down the stairs, while it sometimes climbs due to thermal fluctuations. (b) Maxwell's demon enables the particle to steadily climb by measurement and feedback control. When the particle jumps upward, the demon places a thin barrier behind the particle.

context of Maxwell's demon [22, 23]. For example, let us consider a Brownian particle under a staircase potential as illustrated in Fig. 1.2(a). The particle typically goes down the stairs dissipating heat into the environment, while it can climb the stairs with a certain small probability due to thermal fluctuations if the stair height is comparable to k_BT (k_B is the Boltzmann constant). However, if there is a demon that observes the position of the particle and places a barrier behind the particle right after the upward jump, the particle can steadily climb the stairs absorbing heat from the environment as illustrated in Fig. 1.2(b). This can be regarded as a measurement-feedback process at the level of thermal fluctuations. Since the placement of the barrier does not perform any work on the particle, this phenomenon apparently violates the second law. Information thermodynamics reveals that information entropy associated with the measurement outcome should be equally treated as thermodynamic entropy, which compensates for the apparent entropy decrease to recover the second law in the total system of the particle and the demon. Information thermodynamics has been demonstrated in various experiments [24–29]. It has also theoretically been extended to autonomous processes, where measurement and feedback control are not separated in time [19, 20, 30–34].

Meanwhile, another fundamental relation called the thermodynamic uncertainty relation (TUR) has been discovered recently [35–38]. The TUR is a tradeoff relation between the dissipation and the fluctuation of currents J_d:

$$\langle S \rangle \geq \frac{2k_B \langle J_d \rangle^2}{\mathrm{Var}(J_d)}, \tag{1.1}$$

where J_d depends on the choice of the coefficient d and is called the generalized current (see Sec. 3.1.1 for the definition), and $\mathrm{Var}(J_d)$ is the variance of J_d. The TUR has been one of the hottest topics in stochastic thermodynamics over the past few years, since the TUR gives a strictly tighter constraint on the entropy production than the second law, and thus has a lot of applications. In this thesis, our primary interest lies in its application to the estimation of the entropy production as described later.

The estimation of the entropy production in biological systems has been gaining much interest in recent years [39–41]. This is because recent developments in experimental techniques have enabled us to observe dynamics of biological systems at the level close to elementary stochastic processes, and the entropy production can ideally quantify the energy consumption of the dynamics [42]. For example, as shown in Fig. 1.3, the entropy production has been used to quantitatively study the relation between the dynamical stability and the energy consumption rate of a contractile actomyosin network [39], which is driven out of equilibrium by the myosin activity. It is concluded that the entropy production rate is maximized before the contraction (denoted as S_1), while it decreases during the contraction (denoted as C) because of the mechanical relaxation such as polarity sorting and filament severing.

The TUR is expected to be useful for the estimation of the entropy production on the basis of trajectory data [43–45], which is still not an easily tractable problem. For example, the estimation of the forward and backward transition probabilities requires full details of the stochastic dynamics, and thus the direct use of the fluctuation theorem is not practical. On the other hand, the TUR provides a variational estimation method as follows: (i) find the optimal current J_d^* (or optimal coefficient d^*) that maximizes the lower bound of the

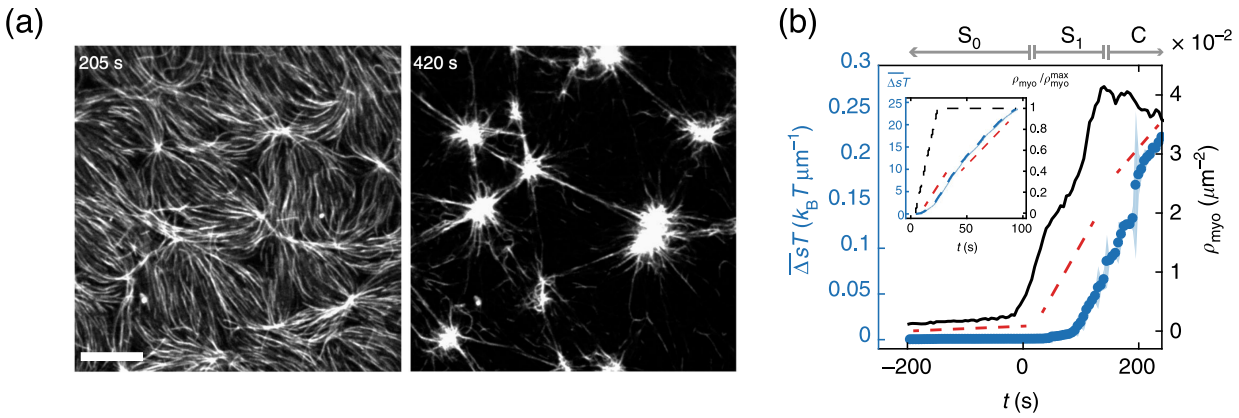

Figure 1.3: Contraction of actomyosin and the entropy production. (a) Filamentous actin network contracts due to the myosin activity. (b) Ensemble averaged entropy production per unit length of a single myosin filament. The dynamics is classified as S_0 (stable state before myosin thick filament formation), S_1 (stable state as myosin thick filament accumulates), and C (contractile state). The entropy production rate, which is the slope of the blue dots, is maximized at S_1. Reprinted figure from Ref. [39] (DOI: 10.1038/s41467-018-07413-5). Figure is available under the terms of the Creative Commons Attribution 4.0 International license.

TUR (Eq. (1.1)), and (ii) use the lower bound as an estimate of the entropy production. This approach is expected to be data efficient, since it only requires the mean and the variance of a single fluctuating current J_d, which can be estimated with trajectory data. Moreover, this approach has turned out to be promising because it has been numerically suggested that the TUR can give the exact estimate, not only a lower bound, of the entropy production by taking the short-time limit for the generalized current (which we refer to as the short-time TUR) [45].

There are three fundamental remaining issues in this approach. First, the equality condition of the short-time TUR has not been analytically studied, and its range of applicability has been unclear. Second, the previous studies have not considered the maximization in practical setups. Third, the practical effectiveness of this approach has been still unclear, for example, whether this approach is good at high-dimensional data as suggested in Ref. [44].

In this thesis, we present two main results to establish the variational estimation method. In the first part, we resolve these issues. First, we formulate the short-time TUR and reveal the equality condition analytically. Next, we develop a platform for applying machine learning to this variational approach, and construct practical estimators, which leverage the benefit of maximization, for stationary dynamics. Then, we numerically demonstrate the effectiveness of our method, especially in high-dimensional and non-linear setups.

In the second part, we extend the variational method developed in the first part to non-stationary dynamics. For the non-stationary estimation, an ensemble of trajectories

sampled from repeated experiments is necessary, in contrast to the stationary case where a single long trajectory is enough. Thus, it is desirable to consider a method that can reduce the number of necessary trajectories. With this motivation, we propose the continuous-time estimation scheme that learns the thermodynamic force continuously in time. We show that the continuous-time estimation is data efficient since the estimate converges not only by increasing the number of trajectories but also by increasing the sampling frequency of the trajectories.

Our method is of practical significance since it is solely based on trajectory data and applicable to a broad class of stochastic dynamics out of equilibrium. More details of our main results will be summarized in the next section below.

1.2 Outline of the thesis

This thesis is organized as follows. In Chapters 2, 3, and 4, we review fundamental concepts and previous results related to this study. In Chapters 5, 6, and Appendix A, we show our main results.

In Chapter 2, we review the framework of stochastic thermodynamics both for Langevin dynamics and Markov jump processes. We also introduce the partial entropy production to formulate information thermodynamics. In Chapter 3, we review the TUR. We especially explain in detail a jump process approximation of Langevin dynamics and the equality condition of the TUR. In Chapter 4, we review previous studies on the estimation of the entropy production, especially focusing on non-invasive methods. In the review part, we assume a little prior knowledge of stochastic calculus and information theory.

In Chapter 5, we establish the variational estimation method of the entropy production in stationary dynamics using the short-time TUR along with machine learning techniques. First, we formulate the short-time TUR both for Markov jump processes and overdamped Langevin dynamics, and reveal the equality condition analytically. We find that the equality is always achievable in Langevin dynamics, while this is not the case in general Markov jump processes. Next, we propose a variational estimation method by employing ideas from machine learning such as the gradient ascent and the data splitting scheme. Then, we construct practical learning estimators and numerically demonstrate our method. As a result, we find that the learning estimators outperform a previous method in high-dimensional and non-linear Langevin dynamics. In addition, the learning estimator in Markov jump processes is shown to be robust against the sampling interval of trajectories.

In Chapter 6, we develop an estimation method of the entropy production in non-stationary dynamics by extending the learning algorithm developed in Chapter 5. First, we establish the theoretical relationship between the variational representations including the short-time TUR. Next, we propose the continuous-time estimation scheme that learns the time-dependent thermodynamic force by using an ensemble of trajectories. We implement our method using neural networks, and demonstrate it with two linear Langevin models by comparing the estimation results with the analytical solutions. We show that the continuous-time estimation method gives an exact estimate of the entropy production and the thermodynamic force, and that it is data efficient since the estimate converges not only by increasing the number of trajectories but also by increasing the number of time

instances contained in each trajectory. We also demonstrate the practical effectiveness of our method by considering various perturbations to the setup.

In Chapter 7, we summarize the above results and give some remarks on future perspectives.

In Appendix A, we study information thermodynamics of a molecular motor called F_1-ATPase (or F_1), which is a side issue and rather independent of the foregoing main results. After we introduce the reaction-diffusion model of F_1, we formulate information thermodynamics of the model. Then, we numerically study the behavior of information-thermodynamic quantities. We show that F_1 is information-thermodynamically efficient, and even negative internal heat dissipation is realized as a result of the (demon-like) feedback structure underlying the dynamics.

Chapter 2

Stochastic thermodynamics

In this chapter, we review the framework of stochastic thermodynamics [1–6]. We explain its formulation in Langevin dynamics in Sec. 2.1, and Markov jump processes in Sec. 2.2. In Sec. 2.3, we introduce the partial entropy production, and explain information thermodynamics [15–21].

2.1 Dynamics on continuous state spaces

In this section, we review the framework of stochastic thermodynamics in Langevin dynamics. We first explain how thermodynamic quantities are defined at the level of single trajectories using a simple example, and introduce the first and second laws of thermodynamics. Then, we introduce a general formulation, and derive the fluctuation theorem and the expression of the entropy production rate. In the last subsection, we get back to the first example, and check the consistency of the general formulation.

2.1.1 Stochastic energetics in Langevin dynamics

Let us consider a Brownian particle moving under external force $f(t)$. The dynamics of the particle can be described by an underdamped Langevin equation:

$$\dot{x}(t) = v(t), \tag{2.1}$$

$$m\dot{v}(t) = -\gamma v(t) + f(t) + \sqrt{2\gamma T}\eta(t), \tag{2.2}$$

where m is the mass, γ is the viscous damping coefficient, T is the temperature, and $\eta(t)$ is the Gaussian white noise satisfying $\langle \eta(t)\eta(t')\rangle = \delta(t-t')$. Here, the noise intensity $\sqrt{2\gamma T}$ is determined by the condition that the velocity should relax to the Boltzmann distribution, which is often referred to as the second fluctuation-dissipation theorem. Since the inertia term $m\dot{v}_t$ is known to be negligibly small in many experimental setups, the following equation that drops the inertia term is often used:

$$\gamma\dot{x}(t) = f(t) + \sqrt{2\gamma T}\eta(t), \tag{2.3}$$

which is called the overdamped Langevin equation.

The central task to formulate stochastic thermodynamics is to define the heat dissipated

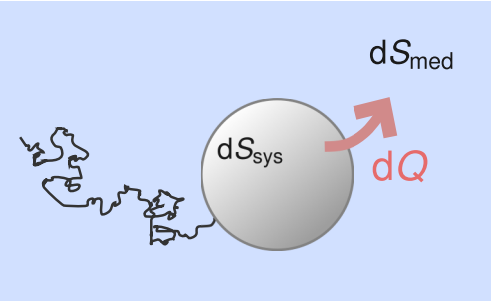

Figure 2.1: Schematic of a Brownian particle and the entropy change. The dissipated heat is associated with the entropy change of the medium.

into the environment. Since the particle feels the force $(-\gamma\dot{x}(t) + \sqrt{2\gamma T}\eta(t))$ from the environment through the friction and the noise, we can consider that the particle does the equivalent work against the environment by action-reaction principle. Thus, the heat dissipated into the environment is identified as [5]

$$\mathrm{d}Q := \mathrm{d}x(t) \circ \left(\gamma\dot{x}(t) - \sqrt{2\gamma T}\eta(t)\right), \tag{2.4}$$

where $\circ$ is the Stratonovich product.

We can formulate the first law of thermodynamics by substituting Eq. (2.4) into Eq. (2.2). A proper definition of the internal energy E depends on the case, and the definition of the work changes accordingly. For example, if we define the internal energy as $E = \frac{1}{2}mv^2$, the extracted work is identified as $\mathrm{d}W = -f\mathrm{d}x$, leading to the first law of thermodynamics:

$$\mathrm{d}E = -\mathrm{d}Q - \mathrm{d}W. \tag{2.5}$$

In another case in which the external force is conservative and described by some potential $f(x,t) = -\partial_x U(x,a)$ with parameter $a(t)$, it is natural to define the internal energy as $E = \frac{1}{2}mv^2 + U(x,a)$, and the extracted work becomes $-\partial_a U(x,a) \circ \mathrm{d}a$ in this case. We note that these expressions hold straightforwardly in overdamped Langevin dynamics by setting $m = 0$.

Next, we introduce the entropy production. The entropy change in the system is defined by

$$\mathrm{d}S_{\mathrm{sys}} := -\mathrm{d}\ln p(x(t), v(t), t), \tag{2.6}$$

where $p(x,v,t)$ is the probability density. The system entropy change quantifies the displacement of the Shannon entropy $-\int \mathrm{d}x\mathrm{d}v p(x,v,t)\ln p(x,v,t)$ when ensemble averaged. We note that the Boltzmann constant is set to unity $k_B = 1$ hereafter. In overdamped Langevin dynamics, the velocity does not appear in the probability density, and the system entropy change is defined by $\mathrm{d}S_{\mathrm{sys}} := -\mathrm{d}\ln p(x(t), t)$. The dissipated heat can be regarded as the entropy change in the environment, or the medium, $\mathrm{d}S_{\mathrm{med}}$, and the total entropy production $\mathrm{d}S$ is defined as the summation of these terms (see Fig. 2.1 for a schematic):

$$\mathrm{d}S_{\mathrm{med}} := \frac{\mathrm{d}Q}{T}, \tag{2.7}$$

$$\mathrm{d}S := \mathrm{d}S_{\mathrm{sys}} + \mathrm{d}S_{\mathrm{med}}. \tag{2.8}$$

We emphasize that the thermodynamic quantities defined in this section are stochastic quantities at the level of single trajectories. In contrast to the first law, which holds at the trajectory level by definition, the second law of thermodynamics holds in the ensemble level as

$$\langle \mathrm{d}S \rangle \geq 0. \tag{2.9}$$

It means that the entropy production can be negative with a certain small probability, while its ensemble average always takes non-negative values. Here, the entropy production was defined as an infinitesimal displacement, and the entropy production along a trajectory is defined by its integral

$$S := \int_0^t \mathrm{d}S, \tag{2.10}$$

which also satisfies the second law $\langle S \rangle \geq 0$. Note that we use d to denote an infinitesimal displacement in time, but not necessarily the total differentiation, and S is not a state variable in this thesis.

In the following subsections, we reformulate these thermodynamic quantities in a general setup, and show that the entropy production satisfies the second law as a consequence of the fluctuation theorem.

2.1.2 Setup for a general formulation

We consider an n-dimensional Langevin equation with multiplicative noise:

$$\dot{\boldsymbol{x}}(t) = \boldsymbol{A}(\boldsymbol{x}(t), t) + \boldsymbol{B}(\boldsymbol{x}(t), t) \cdot \boldsymbol{\eta}(t), \tag{2.11}$$

where $\boldsymbol{A}(\boldsymbol{x}, t)$ is the drift vector and $\boldsymbol{B}(\boldsymbol{x}, t)$ is an $n \times n$ matrix, and $\boldsymbol{\eta}(t)$ is the Gaussian white noise satisfying $\langle \eta_i(t)\eta_j(t') \rangle = \delta_{ij}\delta(t - t')$. The noise is multiplicative, and the product $\cdot$ is taken in the Ito sense. Note that when the diffusion matrix depends on the state variables, the noise is called multiplicative. If it does not, the noise is called additive.

The variables x_i can be either even or odd under time reversal. We define the time reversal operation $\boldsymbol{\varepsilon x} = (\varepsilon_1 x_1, \varepsilon_2 x_2, ..., \varepsilon_N x_N)$ with $\varepsilon_i = \pm 1$ for even and odd variables x_i, respectively. It is convenient to decompose the drift term $\boldsymbol{A}(\boldsymbol{x}, t)$ into reversible and irreversible components as

$$A_i^{\mathrm{ir}}(\boldsymbol{x}, t) := \frac{1}{2}\left[A_i(\boldsymbol{x}, t) + \varepsilon_i A_i(\boldsymbol{\varepsilon x}, t)\right] = \varepsilon_i A_i^{\mathrm{ir}}(\boldsymbol{\varepsilon x}, t), \tag{2.12}$$

$$A_i^{\mathrm{rev}}(\boldsymbol{x}, t) := \frac{1}{2}\left[A_i(\boldsymbol{x}, t) - \varepsilon_i A_i(\boldsymbol{\varepsilon x}, t)\right] = -\varepsilon_i A_i^{\mathrm{rev}}(\boldsymbol{\varepsilon x}, t). \tag{2.13}$$

Next, we introduce the Fokker-Planck equation corresponding to the Ito-type Langevin equation (2.11):

$$\partial_t p(\boldsymbol{x}, t) = -\boldsymbol{\nabla}\, \boldsymbol{j}(\boldsymbol{x}, t), \tag{2.14}$$

$$\boldsymbol{j}(\boldsymbol{x}, t) := \boldsymbol{A}(\boldsymbol{x}, t)p(\boldsymbol{x}, t) - \boldsymbol{\nabla}\left[\boldsymbol{D}(\boldsymbol{x}, t)p(\boldsymbol{x}, t)\right], \tag{2.15}$$

where $p(\boldsymbol{x},t)$ is the probability density, and $\boldsymbol{D}(\boldsymbol{x},t)$ is the diffusion matrix defined by

$$\boldsymbol{D}(\boldsymbol{x},t) := \frac{1}{2}\boldsymbol{B}(\boldsymbol{x},t)\boldsymbol{B}(\boldsymbol{x},t)^{\mathsf{T}}. \tag{2.16}$$

The diffusion matrix is assumed to be symmetric under time reversal $D_i(\boldsymbol{\varepsilon x}) = D_i(\boldsymbol{x})$.

The Fokker-Planck equation describes the time-evolution of the probability density, and is useful for discussing thermodynamic quantities at the ensemble level. For the latter convenience, we define the reversible and irreversible components of the probability current $\boldsymbol{j}(\boldsymbol{x},t)$ as

$$\begin{aligned}
\boldsymbol{j}(\boldsymbol{x},t) &= \boldsymbol{j}^{\mathrm{ir}}(\boldsymbol{x},t) + \boldsymbol{j}^{\mathrm{rev}}(\boldsymbol{x},t), && (2.17)\\
\boldsymbol{j}^{\mathrm{ir}}(\boldsymbol{x},t) &:= \boldsymbol{A}^{\mathrm{ir}}(\boldsymbol{x},t)p(\boldsymbol{x},t) - \boldsymbol{\nabla}\left[\boldsymbol{D}(\boldsymbol{x},t)p(\boldsymbol{x},t)\right], && (2.18)\\
\boldsymbol{j}^{\mathrm{rev}}(\boldsymbol{x},t) &:= \boldsymbol{A}^{\mathrm{rev}}(\boldsymbol{x},t)p(\boldsymbol{x},t). && (2.19)
\end{aligned}$$

In the next subsection, we see that only the irreversible current appears in the expression of the entropy production rate, which is the reason why it is called irreversible.

2.1.3 Entropy production

Here, we define the entropy production in a general manner, and derive the fluctuation theorem and the second law of thermodynamics. Its consistency to the definition in Sec. 2.1.1 is discussed in Sec. 2.1.5. We also introduce the expression of the entropy production rate.

First, the single-step entropy production $\mathrm{d}S$ associated with a jump from $\boldsymbol{x}$ to $\boldsymbol{x}'$ during a time interval $[t, t+\mathrm{d}t]$ is defined as

$$\begin{aligned}
\mathrm{d}S &= \mathrm{d}S_{\mathrm{sys}} + \mathrm{d}S_{\mathrm{med}}, && (2.20)\\
\mathrm{d}S_{\mathrm{sys}} &:= \ln\frac{p(\boldsymbol{x},t)}{p(\boldsymbol{x}',t+\mathrm{d}t)}, && (2.21)\\
\mathrm{d}S_{\mathrm{med}} &:= \ln\frac{p(\boldsymbol{x}',t+\mathrm{d}t|\boldsymbol{x},t)}{p(\boldsymbol{\varepsilon x},t+\mathrm{d}t|\boldsymbol{\varepsilon x}',t)}, && (2.22)
\end{aligned}$$

where $\mathrm{d}S_{\mathrm{sys}}$ is the single-step entropy change of the system, and $\mathrm{d}S_{\mathrm{med}}$ is that of the environment, and $p(\boldsymbol{x}',t+dt|\boldsymbol{x},t)$ is the transition probability density from $\boldsymbol{x}$ to $\boldsymbol{x}'$ at time t. Then, the entropy production along a stochastic trajectory $S[\boldsymbol{x}(\cdot),t]$ is defined by the integral of $\mathrm{d}S$:

$$S := \int_0^\tau \mathrm{d}S. \tag{2.23}$$

The definition of $\mathrm{d}S_{\mathrm{sys}}$ is the same as in Sec. 2.1.1, while $\mathrm{d}S_{\mathrm{med}}$ is more abstract. If we accept this definition, it is easy to derive the fluctuation theorem:

$$\langle\exp\left(-S\right)\rangle = 1. \tag{2.24}$$

As a consequence, the entropy production becomes non-negative on average:

$$\langle S\rangle \geq 0. \tag{2.25}$$

The derivation is as follows. By definition, the entropy production S can be written as the logarithm of the ratio between the forward and backward transition probability densities:

$$S = \ln \frac{p(\boldsymbol{x}(0), 0)}{p(\boldsymbol{x}(\tau), \tau)} + \ln \frac{\mathcal{P}\left[\boldsymbol{x}(\tau)|\boldsymbol{x}(0)\right]}{\mathcal{P}^\dagger\left[\boldsymbol{\varepsilon x}(0)|\boldsymbol{\varepsilon x}(\tau)\right]}, \tag{2.26}$$

where $\mathcal{P}$ is the probability density of the forward transition, $\mathcal{P}^\dagger$ is that of the backward transition under the time reversed protocol, and $\mathcal{P}^\dagger\left[\boldsymbol{\varepsilon x}(0)|\boldsymbol{\varepsilon x}(\tau)\right]$ can be explicitly written by the product of $p(\boldsymbol{\varepsilon x}(t), t + \mathrm{d}t|\boldsymbol{\varepsilon x}(t + \mathrm{d}t), t)$ for a given path $\boldsymbol{x}(t)$. Then, the fluctuation theorem can be derived as follows:

$$\begin{aligned}
\langle \exp(-S) \rangle &= \int \mathrm{d}\Gamma p(\boldsymbol{x}(0), 0) \mathcal{P}\left[\boldsymbol{x}(\tau)|\boldsymbol{x}(0)\right] \exp(-S) && (2.27)\\
&= \int \mathrm{d}\Gamma p(\boldsymbol{x}(\tau), \tau) \mathcal{P}^\dagger\left[\boldsymbol{\varepsilon x}(0)|\boldsymbol{\varepsilon x}(\tau)\right] && (2.28)\\
&= 1, && (2.29)
\end{aligned}$$

where $\mathrm{d}\Gamma$ is the volume element of the forward trajectory, and we used $\int \mathrm{d}\boldsymbol{x}(t) p(\boldsymbol{\varepsilon x}(t), t + \mathrm{d}t|\boldsymbol{\varepsilon x}(t + \mathrm{d}t), t) = 1$. Then, the non-negativity of the mean entropy production directly follows from the convex inequality $\langle \exp(-S) \rangle \geq \exp(-\langle S \rangle)$.

Next, we introduce the entropy production rate. The entropy production rate defined by $\sigma(t) := \langle \mathrm{d}S \rangle / \mathrm{d}t$ has the following expression:

$$\sigma(t) = \int \mathrm{d}\boldsymbol{x} \, \frac{\boldsymbol{j}^{\mathrm{ir}}(\boldsymbol{x}, t)^\mathsf{T} \boldsymbol{D}(\boldsymbol{x}, t)^{-1} \boldsymbol{j}^{\mathrm{ir}}(\boldsymbol{x}, t)}{p(\boldsymbol{x}, t)}. \tag{2.30}$$

The derivation is explained in the next subsection. From this expression, it is clear that the entropy production rate is non-negative $\sigma(t) \geq 0$. We note that the entropy production rate is always an averaged quantity, since the variance of $\mathrm{d}S/\mathrm{d}t$ diverges.

In overdamped Langevin dynamics, the irreversible current equals the probability current. In this case, the entropy production rate can be written as

$$\sigma(t) = \int \mathrm{d}\boldsymbol{x} \, \boldsymbol{F}(\boldsymbol{x}, t) \boldsymbol{j}(\boldsymbol{x}, t), \tag{2.31}$$

where $\boldsymbol{F}(\boldsymbol{x}, t)$ is the thermodynamic force defined using the mean local velocity $\boldsymbol{\nu}(\boldsymbol{x}, t)$ as

$$\begin{aligned}
\boldsymbol{F}(\boldsymbol{x}, t) &:= \boldsymbol{\nu}(\boldsymbol{x}, t)^\mathsf{T} \boldsymbol{D}(\boldsymbol{x}, t)^{-1}, && (2.32)\\
\boldsymbol{\nu}(\boldsymbol{x}, t) &:= \boldsymbol{j}(\boldsymbol{x}, t) / p(\boldsymbol{x}, t). && (2.33)
\end{aligned}$$

The thermodynamic force quantifies the local dissipation, and contains information of the system and the medium entropy changes. For example, if the diffusion matrix is independent of the state variables, the thermodynamic force is explicitly written as

$$\boldsymbol{F}(\boldsymbol{x}, t) = \boldsymbol{D}^{-1} \boldsymbol{A}(\boldsymbol{x}, t) - \boldsymbol{\nabla} \ln p(\boldsymbol{x}, t). \tag{2.34}$$

Here, the first term quantifies the local medium entropy change, and the second term quantifies the local system entropy change.

2.1.4 Derivation of the entropy production rate

In this subsection, we derive the expression (2.30), generalizing the derivation in Ref. [46] where the diffusion matrix is assumed to be diagonal.

Transition probability density

Here, we derive the transition probability density $p(\boldsymbol{x}', t+\mathrm{d}t|\boldsymbol{x}, t)$, which is necessary for calculating $\mathrm{d}S$. The transition probability density for the Fokker-Planck equation (2.14) can be obtained as

$$p(\boldsymbol{x}', t+\mathrm{d}t|\boldsymbol{x}, t) = \mathcal{N} \exp\left[-\frac{1}{4\mathrm{d}t}\boldsymbol{P}^{\mathsf{T}}\boldsymbol{D}^{-1}\boldsymbol{P} - a\boldsymbol{\nabla}\boldsymbol{A}(\boldsymbol{z})\mathrm{d}t + a^2 Q\mathrm{d}t\right], \tag{2.35a}$$

$$\mathcal{N} := \frac{1}{\sqrt{(4\pi\mathrm{d}t)^n \det(\boldsymbol{D}(\boldsymbol{z}))}} \tag{2.35b}$$

$$\boldsymbol{P} := \boldsymbol{x}' - \boldsymbol{x} - \boldsymbol{A}(\boldsymbol{z})\mathrm{d}t + 2a\boldsymbol{\nabla}\boldsymbol{D}(\boldsymbol{z})\mathrm{d}t, \tag{2.35c}$$

$$Q := \sum_{i,j} \nabla_i \nabla_j D_{ij}(\boldsymbol{x})\big|_{\boldsymbol{x}=\boldsymbol{z}}, \tag{2.35d}$$

where the time dependence of each term is omitted for simplicity. The parameter a can be chosen arbitrarily ranging from 0 to 1, which determines the evaluation point $\boldsymbol{z} := a\boldsymbol{x}' + (1-a)\boldsymbol{x}$.

We give some remarks for the free parameter a. The transition probability density is correct up to the order of $\mathrm{d}t$, whatever value is used for a. It can be determined independently of the underlying dynamics, and thus we need not choose $a = 0$ even if the underlying dynamics is the Ito-type Langevin equation (2.11).

However, the choice of a is important when we calculate the entropy production. Let us say that the evaluation point for the backward transition probability density $p(\boldsymbol{\varepsilon}\boldsymbol{x}, t+\mathrm{d}t|\boldsymbol{\varepsilon}\boldsymbol{x}', t)$ is $\boldsymbol{z}' = b\boldsymbol{x} + (1-b)\boldsymbol{x}'$. Then, it is shown that $a + b = 1$ should be satisfied so that the entropy production becomes independent of the free parameters a and b [46]. This condition means that both the forward and backward transition probability densities should be evaluated at the same point, i.e., $\boldsymbol{z}' = \boldsymbol{z}$.

Here, we derive the transition probability density (2.35a). We first rewrite the Fokker-Planck equation (2.14) using the time-evolution operator $L_{\mathrm{FP}}(\boldsymbol{x})$ as

$$\partial_t p(\boldsymbol{x}, t) = L_{\mathrm{FP}}(\boldsymbol{x}) p(\boldsymbol{x}, t), \tag{2.36}$$

$$L_{\mathrm{FP}}(\boldsymbol{x}) := -\boldsymbol{\nabla}\boldsymbol{A}(\boldsymbol{x}) + \sum_{i,j} \nabla_i \nabla_j D_{ij}(\boldsymbol{x}). \tag{2.37}$$

Since Eq. (2.36) means $p(\boldsymbol{x}, t+\mathrm{d}t) = [1 + L_{\mathrm{FP}}(\boldsymbol{x})\mathrm{d}t]\, p(\boldsymbol{x}, t)$, we can derive the transition probability density by dividing the both sides by $p(\boldsymbol{x}_0, t)$ as

$$p(\boldsymbol{x}, t+\mathrm{d}t|\boldsymbol{x}_0, t) = \left[1 + L_{\mathrm{FP}}(\boldsymbol{z})\mathrm{d}t + O(\mathrm{d}t^2)\right] \delta(\boldsymbol{x} - \boldsymbol{x}_0), \tag{2.38}$$

$$L_{\mathrm{FP}}(\boldsymbol{z}) = -\boldsymbol{\nabla}\boldsymbol{A}(\boldsymbol{z}) + \sum_{i,j} \nabla_i \nabla_j D_{ij}(\boldsymbol{z}) \tag{2.39}$$

$$= -\left[a\boldsymbol{\nabla}\boldsymbol{A}(\boldsymbol{z})\right] - \boldsymbol{A}(\boldsymbol{z})\boldsymbol{\nabla} + \left[a^2 \nabla_i \nabla_j D_{ij}(\boldsymbol{z})\right] + 2a\left[\nabla_i D_{ij}(\boldsymbol{z})\right]\nabla_j + D_{ij}(\boldsymbol{z})\nabla_i \nabla_j, \tag{2.40}$$

where we replaced $\boldsymbol{x}$ with $\boldsymbol{z}$ since the change of $L_{\rm FP}(\boldsymbol{z},t)\mathrm{d}t$ is just $O(\mathrm{d}t^2)$. Then, we can get Eq. (2.35a) by using the Fourier transformation of $\delta(\boldsymbol{x}-\boldsymbol{x}_0)$ and conducting the Gaussian integral [47].

Derivation of Eq. (2.30)

We derive the expression (2.30) of the entropy production rate. The evaluation point is set to $a=0$ and $b=1$ here for simplicity. In this case, the forward transition probability density becomes

$$
\begin{aligned}
p(\boldsymbol{x}',t+\mathrm{d}t|\boldsymbol{x},t) &= \mathcal{N}\ \exp\left[-\frac{1}{4\mathrm{d}t}\boldsymbol{P}^{\mathsf{T}}\boldsymbol{D}^{-1}\boldsymbol{P}\right] && \text{(2.41a)}\\
\boldsymbol{P} &:= \boldsymbol{x}'-\boldsymbol{x}-\left(\boldsymbol{A}^{\rm rev}(\boldsymbol{x})+\boldsymbol{A}^{\rm ir}(\boldsymbol{x})\right)\mathrm{d}t, && \text{(2.41b)}
\end{aligned}
$$

while the backward transition probability density becomes

$$
\begin{aligned}
p(\boldsymbol{\varepsilon x},t+\mathrm{d}t|\varepsilon\boldsymbol{x}',t) &= \mathcal{N}\ \exp\left[-\frac{1}{4\mathrm{d}t}\boldsymbol{P'}^{\mathsf{T}}\boldsymbol{D}^{-1}\boldsymbol{P'}-\boldsymbol{\varepsilon\nabla}\left(\boldsymbol{A}^{\rm rev}(\boldsymbol{\varepsilon x})+\boldsymbol{A}^{\rm ir}(\boldsymbol{\varepsilon x})\right)\mathrm{d}t+Q\mathrm{d}t\right] && \text{(2.42a)}\\
&= \mathcal{N}\ \exp\left[-\frac{1}{4\mathrm{d}t}\boldsymbol{P'}^{\mathsf{T}}\boldsymbol{D}^{-1}\boldsymbol{P'}-\boldsymbol{\nabla}\left(-\boldsymbol{A}^{\rm rev}(\boldsymbol{x})+\boldsymbol{A}^{\rm ir}(\boldsymbol{x})\right)\mathrm{d}t+Q\mathrm{d}t\right], && \text{(2.42b)}\\
\boldsymbol{P'} &:= -\boldsymbol{\varepsilon}(\boldsymbol{x}'-\boldsymbol{x})-\left(\boldsymbol{A}^{\rm rev}(\boldsymbol{\varepsilon x})+\boldsymbol{A}^{\rm ir}(\boldsymbol{\varepsilon x})\right)\mathrm{d}t+2\boldsymbol{\varepsilon\nabla D}(\boldsymbol{\varepsilon x})\mathrm{d}t && \text{(2.42c)}\\
&= \boldsymbol{\varepsilon}\left\{-(\boldsymbol{x}'-\boldsymbol{x})-\left(-\boldsymbol{A}^{\rm rev}(\boldsymbol{x})+\boldsymbol{A}^{\rm ir}(\boldsymbol{x})\right)\mathrm{d}t+2\boldsymbol{\nabla D}(\boldsymbol{x})\mathrm{d}t\right\} && \text{(2.42d)}\\
&= -(\boldsymbol{x}'-\boldsymbol{x})-\left(-\boldsymbol{A}^{\rm rev}(\boldsymbol{x})+\boldsymbol{A}^{\rm ir}(\boldsymbol{x})\right)\mathrm{d}t+2\boldsymbol{\nabla D}(\boldsymbol{x})\mathrm{d}t, && \text{(2.42e)}\\
Q &:= \sum_{i,j}\varepsilon_i\nabla_i\varepsilon_j\nabla_j D_{ij}(\boldsymbol{\varepsilon x}) && \text{(2.42f)}\\
&= \sum_{i,j}\nabla_i\nabla_j D_{ij}(\boldsymbol{\varepsilon x}), && \text{(2.42g)}
\end{aligned}
$$

where in the third line of $\boldsymbol{P'}$ and in the second line of Q, we used the fact that $\boldsymbol{\varepsilon}$ cancels at $\boldsymbol{P'}^{\mathsf{T}}\boldsymbol{D}^{-1}\boldsymbol{P'}$. The medium entropy change is evaluated as the logarithm of the ratio between these two probability densities. On the other hand, the system entropy change is evaluated as

$$
\begin{aligned}
\mathrm{d}S_{\rm sys} &= -\mathrm{d}\left[\ln p\right] && \text{(2.43a)}\\
&= -\frac{1}{p}\partial_t p\ \mathrm{d}t-\frac{1}{p}\left(\boldsymbol{\nabla}p\right)\ \mathrm{d}\boldsymbol{x}-\frac{1}{2}\sum_{i,j}\nabla_i\nabla_j\ln p\ \mathrm{d}x_i\mathrm{d}x_j && \text{(2.43b)}\\
&= -\frac{1}{p}\partial_t p\ \mathrm{d}t-\frac{1}{p}\left(\boldsymbol{\nabla}p\right)\ \mathrm{d}\boldsymbol{x}-\sum_{i,j}D_{ij}\nabla_i\nabla_j\ln p\ \mathrm{d}t. && \text{(2.43c)}
\end{aligned}
$$

Then, we calculate the entropy production rate by taking the average:

$$
\begin{aligned}
\sigma(t) &= \frac{\langle\mathrm{d}S\rangle}{\mathrm{d}t} && \text{(2.44a)}\\
&= \frac{1}{\mathrm{d}t}\int\mathrm{d}\boldsymbol{x}\int\mathrm{d}\boldsymbol{x}'p(\boldsymbol{x},t)p(\boldsymbol{x}',t+\mathrm{d}t|\boldsymbol{x},t)\mathrm{d}S && \text{(2.44b)}\\
&=: \frac{1}{\mathrm{d}t}\int\mathrm{d}\boldsymbol{x}\ p(\boldsymbol{x},t)\left\langle\mathrm{d}S|\boldsymbol{x}\right\rangle, && \text{(2.44c)}
\end{aligned}
$$

where $\langle \mathrm{d}S|\boldsymbol{x}\rangle := \int \mathrm{d}\boldsymbol{x}' p(\boldsymbol{x}', t+\mathrm{d}t|\boldsymbol{x}, t)\mathrm{d}S$ is the conditional average. It is straightforward to calculate $\sigma(t)$ by noticing the fact that the conditional average $\langle \mathrm{d}S|\boldsymbol{x}\rangle$ can be evaluated just by replacing $\boldsymbol{x}' - \boldsymbol{x}$ with $\left(\boldsymbol{A}^{\mathrm{rev}} + \boldsymbol{A}^{\mathrm{ir}}\right)\mathrm{d}t$. The conditional averages of the system and medium entropy change rates are evaluated as

$$\begin{aligned}
\frac{\langle \mathrm{d}S_{\mathrm{med}}|\boldsymbol{x}\rangle}{\mathrm{d}t} &= \frac{1}{\mathrm{d}t}\left\langle \ln \frac{p(\boldsymbol{x}', t+\mathrm{d}t|\boldsymbol{x}, t)}{p(\boldsymbol{\varepsilon}\boldsymbol{x}, t+\mathrm{d}t|\varepsilon\boldsymbol{x}', t)} \middle| \boldsymbol{x} \right\rangle, && \text{(2.45a)}\\
&= (\boldsymbol{\nabla}\, \boldsymbol{D})^{\mathsf{T}} \boldsymbol{D}^{-1}(\boldsymbol{\nabla}\boldsymbol{D}) - \boldsymbol{A}^{\mathrm{ir}}\boldsymbol{D}^{-1}\boldsymbol{\nabla}\boldsymbol{D} - (\boldsymbol{\nabla}\boldsymbol{D})^{\mathsf{T}}\, \boldsymbol{D}^{-1}\boldsymbol{A}^{\mathrm{ir}} + \boldsymbol{A}^{\mathrm{ir}}\boldsymbol{D}^{-1}\boldsymbol{A}^{\mathrm{ir}}\\
&\quad + \boldsymbol{\nabla}\, \boldsymbol{A}^{\mathrm{ir}} - \boldsymbol{\nabla}\, \boldsymbol{A}^{\mathrm{rev}} - \sum_{i,j} \nabla_i \nabla_j D_{ij}, && \text{(2.45b)}\\
\frac{\langle \mathrm{d}S_{\mathrm{sys}}|\boldsymbol{x}\rangle}{\mathrm{d}t} &= -\frac{1}{p}\partial_t p - \frac{1}{p}\left(\boldsymbol{\nabla} p\right)\left(\boldsymbol{A}^{\mathrm{rev}} + \boldsymbol{A}^{\mathrm{ir}}\right) - \sum_{i,j} D_{ij}\nabla_i \nabla_j \ln p. && \text{(2.45c)}
\end{aligned}$$

Then, we get the expression (2.30) of the entropy production rate by substituting the sum of these terms into Eq. (2.44c), and assuming $p(\boldsymbol{x}, t)$ and $\nabla_i\, p(\boldsymbol{x}, t)$ vanish at the boundaries.

2.1.5 Consistency of the general formulation

In this subsection, we get back to the first example, and check the consistency of the general formulation. In the general formulation, the medium entropy change is defined as the logarithm of the ratio between forward and backward transition probabilities. Its connection to the heat dissipation (Eq. (2.7)) is actually guaranteed by the second fluctuation-dissipation theorem, which determines the noise intensity. In the following, we see this connection by evaluating Eq. (2.22).

If we adopt the underdamped Langevin equation (2.2), the drift term is decomposed into $A_v^{\mathrm{ir}} = -\gamma v/m$ and $A_v^{\mathrm{rev}} = f/m$. Then, the medium entropy change is evaluated as

$$\begin{aligned}
\ln \frac{p(v', t+\mathrm{d}t|v, t)}{p(-v, t+\mathrm{d}t|-v', t)} &= A_v^{\mathrm{ir}} D^{-1}(v' - v - A_v^{\mathrm{rev}}\mathrm{d}t) + \partial_v A_v^{\mathrm{ir}} && \text{(2.46a)}\\
&= -\frac{mv}{T}\left(\mathrm{d}v - \frac{f}{m}\mathrm{d}t\right) - \frac{\gamma}{m}\mathrm{d}t && \text{(2.46b)}\\
&= \frac{1}{T}\left(\gamma v^2 \mathrm{d}t - v\sqrt{2\gamma T}\eta - \frac{\gamma T}{m}\mathrm{d}t\right). && \text{(2.46c)}
\end{aligned}$$

On the other hand, the dissipated heat is evaluated as

$$\begin{aligned}
\mathrm{d}Q &= \mathrm{d}x \circ (\gamma \dot{x} - \sqrt{2\gamma T}\eta) && \text{(2.47a)}\\
&= \gamma v^2 \mathrm{d}t - \frac{v + v'}{2}\sqrt{2\gamma T}\eta && \text{(2.47b)}\\
&= \gamma v^2 \mathrm{d}t - v\sqrt{2\gamma T}\eta - \frac{\mathrm{d}v}{2}\sqrt{2\gamma T}\eta && \text{(2.47c)}\\
&= \gamma v^2 \mathrm{d}t - v\sqrt{2\gamma T}\eta - \frac{\gamma T}{m}\mathrm{d}t. && \text{(2.47d)}
\end{aligned}$$

Therefore, $\mathrm{d}S_{\mathrm{med}} = \mathrm{d}Q/T$ holds. It is important to notice that the Stratonovich product in $\mathrm{d}Q$ is essential to derive this relation.

Even if the overdamped Langevin equation (2.3) is adopted, we can get the same relation. In this case, the drift term is decomposed into $A_x^{\rm ir} = f/\gamma$ and $A_x^{\rm rev} = 0$. Then, the medium entropy change is evaluated as

$$\begin{aligned} \ln \frac{p(x', t+\mathrm{d}t|x,t)}{p(x, t+\mathrm{d}t|x',t)} &= A_x^{\rm ir} D^{-1}(x' - x - A_x^{\rm rev}\mathrm{d}t) && (2.48a)\\ &= \frac{f}{T}\mathrm{d}x && (2.48b)\\ &= (\gamma\dot{x} - \sqrt{2\gamma T}\eta)\mathrm{d}x. && (2.48c) \end{aligned}$$

Thus, $\mathrm{d}S_{\rm med} = \mathrm{d}Q/T$ holds. We note that the Stratonovich product is equivalent to the normal product in this case as can be seen from Eq. (2.48b).

2.2 Dynamics on discrete state spaces

In this section, we briefly review the framework of stochastic thermodynamics in Markov jump processes. We consider a system with a finite number of states, whose jump dynamics is described by a continuous-time Markov jump process. If we write the transition rate from y to z as $r_t(y,z)$, the probability distribution $p_t(x)$ evolves according to the master equation:

$$\begin{aligned} \partial_t p_t(x) &= \sum_y j(y,x;t) && (2.49)\\ &:= \sum_y p_t(y) r_t(y,x) - p_t(x) r_t(x,y), && (2.50) \end{aligned}$$

where $j(y,z;t)$ is the probability current from y to z.

We assume that each transition is coupled to a bath at temperature T, and satisfies the local detailed balance condition:

$$\frac{Q(y,z;t)}{T} = \ln \frac{r_t(y,z)}{r_t(z,y)}, \tag{2.51}$$

where $Q(y,z;t)$ is the heat dissipation associated with the transition from y to z. This condition guarantees that the logarithm of the ratio between forward and backward transition probabilities corresponds to the heat dissipation, and Eq. (2.51) can be regarded as the medium entropy change.

We define the total entropy production. Let us consider the case that jumps occur N times at $t_1, ..., t_N$ during a time interval $[0, \tau]$ ($t_0 := 0$, $t_{N+1} := \tau$). The entropy production along this trajectory is defined by

$$\begin{aligned} S &:= \frac{1}{T}\sum_{i=1}^{N} Q(x_{i-1}, x_i; t_i) + \Delta s, && (2.52)\\ \Delta s &:= \ln p_0(x_0) - \ln p_\tau(x_N), && (2.53) \end{aligned}$$

where x_i is the state during $[t_i, t_{i+1}]$, and Δs is the system entropy change. Then, it is easy to show that the entropy production satisfies the fluctuation theorem, and thus $\langle S \rangle \geq 0$ holds.

2.3 Partial entropy production

In this section, we introduce the partial entropy production [48, 49] for Markov jump processes using the setup in Sec. 2.2. The partial entropy production is a proper definition of the entropy production of subsystems under autonomous interaction. If it is applied to a bivariate system and ensemble-averaged, it gives an information-thermodynamic dissipation. In the following, we introduce the partial entropy production, and briefly explain information thermodynamics.

Here, we consider to define the partial entropy production in a hierarchical manner. We first define the partial entropy production on a transition from y to z (written as $S_{y\to z}$), and then on a set of transitions Ω (written as S_Ω). There are two requirements for the definition.

- (i)Additivity : $S_\Omega = \sum_{y\to z\in\Omega} S_{y\to z}$ and $S = S_G$, where G is all the transitions.
- (ii)Fluctuation theorem : $\langle \exp(-S_\Omega)\rangle = 1$ holds for any set of transitions Ω.

It is nontrivial that there is such a decomposition of the total entropy production. However, it is shown in Ref. [48] that the partial entropy production defined below satisfies these conditions.

The partial entropy production associated with a transition from y to z (hereafter denoted by $y \to z$) is defined as

$$S_{y\to z} := \frac{1}{T} Q_{y\to z} + \Delta s_{y\to z}, \tag{2.54}$$

where $Q_{y\to z}$ is the heat dissipation that occurred on the transition $y \to z$:

$$Q_{y\to z} := \sum_{i=1}^{N} Q(x_{i-1}, x_i; t_i)\delta_{y,x_{i-1}}\delta_{z,x_i}\ , \tag{2.55}$$

and $\Delta s_{y\to z}$ is the system entropy change that occurred on the transition $y \to z$:

$$\Delta s_{y\to z} := s_{y\to z,\mathrm{jump}} - \int_0^\tau \frac{j(y,z;t)\delta_{x(t),z}}{p_t(z)}\mathrm{d}t, \tag{2.56}$$

$$s_{y\to z,\mathrm{jump}} := \sum_{i=1}^{N} \{\ln p_{t_i}(x_{i-1}) - \ln p_{t_i}(x_i)\}\, \delta_{y,x_{i-1}}\delta_{z,x_i}. \tag{2.57}$$

Here, $Q_{y\to z}$ and $s_{y\to z,\mathrm{jump}}$ are associated with jumps on the transition, while the second term of $\Delta s_{y\to z}$ changes between jumps. The meaning of $\Delta s_{y\to z}$ becomes clear by considering the derivative of $-\ln p_t(x(t))$ as

$$\begin{aligned}
\mathrm{d}\left[-\ln p_t(x(t))\right] &= \ln p_t(x(t)) - \ln p_{t+\mathrm{d}t}(x(t+\mathrm{d}t)) && \text{(2.58a)}\\
&= -\frac{\partial_t p_t(x)}{p(x)}\mathrm{d}t\bigg|_{x=x(t)} + \ln p_t(x(t)) - \ln p_t(x(t+\mathrm{d}t)) && \text{(2.58b)}\\
&= -\sum_y \frac{j(y,z;t)}{p_t(z)}\mathrm{d}t\bigg|_{z=x(t)} + \ln p_t(x(t)) - \ln p_t(x(t+\mathrm{d}t)). && \text{(2.58c)}
\end{aligned}$$

Thus, $\Delta s_{y\to z}$ quantifies the contribution of the transition $y \to z$ to $\mathrm{d}[-\ln p_t(x(t))]$ during the time interval $[0, \tau]$, and satisfies

$$\sum_{y\to z\in G} \Delta s_{y\to z} = \int_0^\tau \mathrm{d}\left[-\ln p_t(x(t))\right] \tag{2.59a}$$

$$= \ln p_0(x_0) - \ln p_\tau(x_N). \tag{2.59b}$$

The partial entropy production for a set of transitions Ω is then defined by summing $S_{y\to z}$

$$S_\Omega := \sum_{y\to z\in\Omega} S_{y\to z}. \tag{2.60}$$

It is shown in Ref. [48] that S_Ω satisfies the fluctuation theorem $\langle \exp(-S_\Omega)\rangle = 1$, and thus $\langle S_\Omega\rangle \geq 0$ holds.

In the following, we study the average of the partial entropy production for two cases: (i) on a transition edge, i.e., $\Omega = \{y \to z, z \to y\}$, and (ii) on a subsystem of a bipartite system, where the partial entropy production corresponds to the information-thermodynamic dissipation (see Fig. 2.2 for schematics).

A transition edge

We define the partial entropy production rate associated with a transition edge between y and z as $\sigma_{(y,z)} := \left(\langle \mathrm{d}S_{y\to z}\rangle + \langle \mathrm{d}S_{z\to y}\rangle\right)/\mathrm{d}t$. The partial entropy production rate can be explicitly obtained as follows:

$$\sigma_{(y,z)} = j(y,z;t)\ln\frac{p_t(y)r_t(y,z)}{p_t(z)r_t(z,y)}. \tag{2.61}$$

In the derivation, we use the fact that the second term of Δs cancels with each other when averaged:

$$\left\langle \frac{j(y,z;t)\delta_{x(t),z}}{p_t(z)} \right\rangle + \left\langle \frac{j(z,y;t)\delta_{x(t),y}}{p_t(y)} \right\rangle = j(y,z;t) + j(z,y;t) \tag{2.62a}$$

$$= 0. \tag{2.62b}$$

This means that the second term is relevant only for the higher order cumulants of the partial entropy production when both directions of each transition are included in Ω.

Bipartite system

Here, we consider the partial entropy production of a bipartite system. Let us assume that the system is described as a direct product of subsystems X and Y, whose state is written as $\{x, y\}$. Note that we use X, Y to denote the stochastic variables, and x, y to denote their states here. It is called bipartite when the transition rate from $\{x, y\}$ to $\{x', y'\}$ satisfies the following condition:

$$r_t\left(\{x,y\},\{x',y'\}\right) = 0 \text{ if } x \neq x' \text{ and } y \neq y'. \tag{2.63}$$

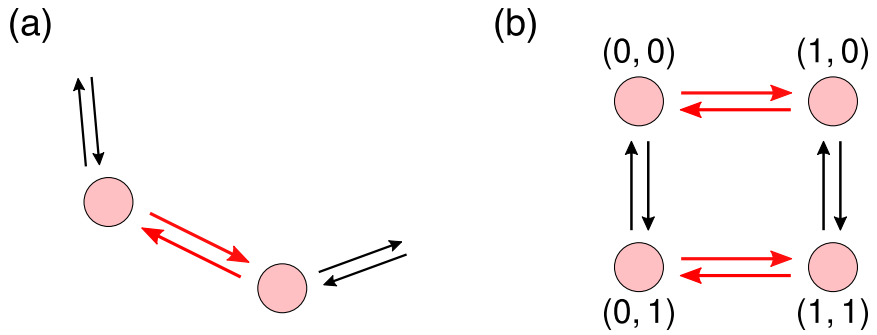

Figure 2.2: Schematics of the set of transitions described by the red arrows: (a) a transition edge, (b) a subsystem of a bipartite system. In (a), only a part of a whole network is drawn. In (b), we show a four state model with states (x, y), where the subsystems take two values 0 or 1.

This means that the two variables do not jump simultaneously, or its probability is negligibly small. With the bipartite condition, the probability current is decomposed into two parts:

$$\partial_t p_t(x,y) = \sum_{x',y'} j\left(\{x',y'\},\{x,y\};t\right) \tag{2.64a}$$

$$= \sum_{x'} j\left(\{x',y\},\{x,y\};t\right) + \sum_{y'} j\left(\{x,y'\},\{x,y\};t\right). \tag{2.64b}$$

We define S_X (resp. S_Y) as the partial entropy production associated with transitions by the subsystem X (resp. Y). Then, their rates are explicitly obtained as follows [19]:

$$\sigma_X = \sum_{x>x',y} j\left(\{x',y\},\{x,y\};t\right) \ln \frac{p_t(x',y) r_t\left(\{x',y\},\{x,y\}\right)}{p_t(x,y) r_t\left(\{x,y\},\{x',y\}\right)}, \tag{2.65}$$

$$\sigma_Y = \sum_{x,y>y'} j\left(\{x,y'\},\{x,y\};t\right) \ln \frac{p_t(x,y') r_t\left(\{x,y'\},\{x,y\}\right)}{p_t(x,y) r_t\left(\{x,y\},\{x,y'\}\right)}. \tag{2.66}$$

σ_X can be decomposed into three parts:

$$\sigma_X = \sigma_X^{\rm sys} + \sigma_X^{\rm med} - l_X, \tag{2.67}$$

$$\sigma_X^{\rm sys} := \sum_{x>x',y} j\left(\{x',y\},\{x,y\};t\right) \ln \frac{p_t(x')}{p_t(x)}, \tag{2.68}$$

$$\sigma_X^{\rm med} := \sum_{x>x',y} j\left(\{x',y\},\{x,y\};t\right) \ln \frac{r_t\left(\{x',y\},\{x,y\}\right)}{r_t\left(\{x,y\},\{x',y\}\right)}, \tag{2.69}$$

$$l_X := \sum_{x>x',y} j\left(\{x',y\},\{x,y\};t\right) \ln \frac{p_t(y|x)}{p_t(y|x')}, \tag{2.70}$$

where $p_t(y|x)$ is the conditional probability defined by $p_t(y|x) := p_t(x,y)/p_t(x)$. The partial entropy production rate σ_Y can also be decomposed into three parts $\sigma_Y^{\rm sys}, \sigma_Y^{\rm med}$, and l_Y in

the same manner. We call σ_X and σ_Y information-thermodynamic dissipation.

In addition to the conventional entropy production $\sigma_X^{\rm sys}+\sigma_X^{\rm med}$, an information-theoretic term l_X called learning rate [30,31,33,34] appears in σ_X. To illustrate the meaning of l_X, we introduce the mutual information $I(X,Y;t)$ defined by

$$I(X,Y;t) := \sum_{x,y} p_t(x,y) \ln \frac{p_t(x,y)}{p_t(x)p_t(y)} \geq 0. \tag{2.71}$$

The mutual information quantifies the correlation between X and Y. For example, it becomes zero if and only if the two variables are independent, i.e., $p_t(x,y) = p_t(x)p_t(y)$ for any pair of x and y. The learning rate of X (resp. Y) quantifies the increase of the mutual information by the transitions of X (resp. Y), and their sum equals the time derivative of the mutual information:

$$\begin{aligned}
\partial_t I(X,Y;t) &= \sum_{x,y} \left\{ \partial_t p_t(x,y) \ln \frac{p_t(x,y)}{p_t(x)p_t(y)} + p_t(x,y)\partial_t \left(\ln \frac{p_t(x,y)}{p_t(x)p_t(y)} \right) \right\} && \text{(2.72a)} \\
&= \sum_{x,y} \partial_t p_t(x,y) \ln \frac{p_t(x,y)}{p_t(x)p_t(y)} && \text{(2.72b)} \\
&= \sum_{x,y} \sum_{x'} j\left(\{x',y\},\{x,y\};t\right) \ln \frac{p_t(x,y)}{p_t(x)p_t(y)} \\
&\quad + \sum_{x,y} \sum_{y'} j\left(\{x,y'\},\{x,y\};t\right) \ln \frac{p_t(x,y)}{p_t(x)p_t(y)} && \text{(2.72c)} \\
&= \sum_{x>x',y} j\left(\{x',y\},\{x,y\};t\right) \left(\ln \frac{p_t(x,y)}{p_t(x)p_t(y)} - \ln \frac{p_t(x',y)}{p_t(x')p_t(y)} \right) \\
&\quad + \sum_{x,y>y'} j\left(\{x,y'\},\{x,y\};t\right) \left(\ln \frac{p_t(x,y)}{p_t(x)p_t(y)} - \ln \frac{p_t(x,y')}{p_t(x)p_t(y')} \right) && \text{(2.72d)} \\
&= l_X + l_Y. && \text{(2.72e)}
\end{aligned}$$

Thus, $l_X + l_Y = 0$ holds in the stationary state.

We can interpret the information-thermodynamic dissipation in the context of Maxwell's demon [21]. For example, if $l_X > 0$ and $l_Y < 0$ hold, X is Maxwell's demon and Y is the controlled system. This is because $l_X > 0$ means that X acquires information of Y, while $l_Y < 0$ means that the correlation is consumed, which suggests that X performs feedback control on Y. As a consequence of the feedback control, the conventional entropy production $\sigma_Y^{\rm sys}+\sigma_Y^{\rm med}$ can be negative because of the second law of information thermodynamics:

$$\sigma_Y^{\rm sys} + \sigma_Y^{\rm med} \geq l_Y. \tag{2.73}$$

In the stationary state, it can be written as

$$\dot{Q}_Y \geq T l_Y. \tag{2.74}$$

Thus, the heat dissipation from the subsystem Y can be negative under the feedback control. Indeed, such phenomena have been realized in several artificial setups [27, 28,

50]. We note that the second law of thermodynamics can be recovered by summing the contribution from X as

$$\dot{Q}_X + \dot{Q}_Y \geq T\left(l_X + l_Y\right) = 0. \tag{2.75}$$

Chapter 3

Thermodynamic uncertainty relation

In this chapter, we review thermodynamic uncertainty relation (TUR). In Sec. 3.1, we explain the main idea, and provide a brief review on this topic. In Sec. 3.2, we explain the outline of the derivation proposed in Refs. [36, 43], which are based on the large deviation theory. In Sec. 3.3, we review previous results on the tightness of the TUR bound.

3.1 Overview

In this section, we introduce the TUR, and provide a brief review on its extensions and applications.

3.1.1 Main idea

Recently, a fundamental relation called TUR has been proposed [35–38]. Roughly speaking, the TUR represents a tradeoff relation between dissipation and fluctuation of currents:

$$\sigma \frac{\tau \mathrm{Var}(j_d)}{\langle j_d \rangle^2} \geq 2, \tag{3.1}$$

where $\langle j_d \rangle$ and $\mathrm{Var}(j_d)$ are the mean and the variance of a fluctuating current j_d called generalized current, and τ is the observation time of the current. Here, the generalized current j_d includes any current observables, and thus Eq. (3.1) imposes strict limitation on the realization of currents. This relation can also be viewed as a refinement of the second law, since it means that the entropy production rate becomes strictly positive under the presence of any currents unless their variance is finite.

This relation has been mainly formulated for stationary dynamics described by Markov jump processes [35–37] or overdamped Langevin dynamics [51]. Here, we explain the definition of the generalized current in these processes. In Markov jump processes, we first define an integrated empirical current on a transition edge from y to z as

$$J_\tau(y,z) := \int_0^\tau \mathrm{d}t (\delta_{x(t^-),y}\delta_{x(t^+),z} - \delta_{x(t^-),z}\delta_{x(t^+),y}), \tag{3.2}$$

where $x(t^\pm)$ represents the state before (after) the jump at time t. $J_\tau(y,z)$ counts the net number of jumps from y to z during the time interval $[0,\tau]$. We define the integrated

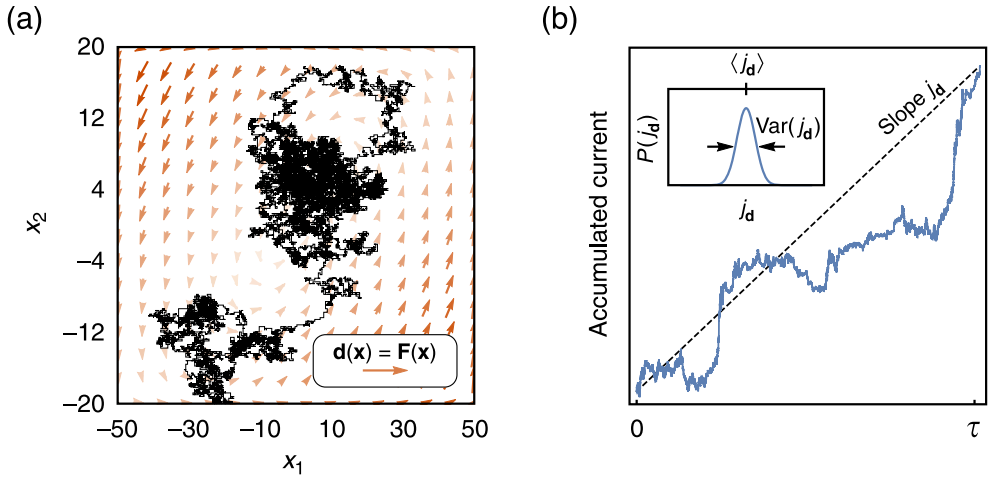

Figure 3.1: Generalized current in Langevin dynamics. (a) A sample trajectory generated by the two beads model (the details of the model can be found in Sec. 5.3) and the thermodynamic force field. (b) The generalized current is defined as the slope of the accumulated current (3.3), which is a stochastic variable as illustrated in the inset figure. Reprinted figure from [44] (DOI: 10.1038/s41467-019-09631-x). Figure is available under the terms of the Creative Commons Attribution 4.0 International license.

generalized current as a linear combination of $J_\tau(y,z)$ with some coefficient satisfying $d(y,z) = -d(z,y)$:

$$J_d := \sum_{y,z} d(y,z) J_\tau(y,z). \tag{3.3}$$

Then, the generalized current is defined by $j_d := J_d/\tau$. We stress that these are stochastic variables, and the mean and the variance of any generalized current satisfy the TUR (3.1). Here, the observation time τ is relevant for the variance $\tau \mathrm{Var}(j_d)$, while $\langle j_d \rangle$ and σ are independent of τ in the stationary state. Thus, we often distinguish the TUR in terms of the time scale as follows: the long-time TUR ($\tau \to \infty$), the finite-time TUR ($\tau > 0$), and the short-time TUR ($\tau \to 0$). Among them, the finite-time TUR is the most general concept, and includes the others.

An important example of the generalized current is the entropy production. In this case, we use $d(y,z) = \ln \frac{\pi(y)r(y,z)}{\pi(z)r(z,y)}$ for the coefficient, where $r(y,z)$ is the transition rate from y to z and π is the stationary distribution. Then, J_d represents the entropy production during the observation time $[0,\tau]$, and the mean of j_d gives the entropy production rate as

$$\langle j_d \rangle = \sum_{y,z} \{\pi(y)r(y,z) - \pi(z)r(z,y)\} \ln \frac{\pi(y)r(y,z)}{\pi(z)r(z,y)}. \tag{3.4}$$

In the same manner, any currents associated with transitions can be expressed as the generalized current.

In Langevin dynamics, the integrated generalized current is defined by

$$J_{\boldsymbol{d}} := \int_0^\tau \boldsymbol{d}(\boldsymbol{x}) \circ \mathrm{d}\boldsymbol{x}(t), \tag{3.5}$$

which is the integral of the Stratonovich product between some coefficient field $\boldsymbol{d}(\boldsymbol{x})$ and the displacement of the state $\mathrm{d}\boldsymbol{x}(t) := \boldsymbol{x}(t+\mathrm{d}t) - \boldsymbol{x}(t)$. Once again, an important example is the entropy production, where the coefficient field is given by the thermodynamic force $\boldsymbol{F}(\boldsymbol{x})$. Since $\boldsymbol{x}(t)$ changes stochastically, $J_{\boldsymbol{d}}$ is a stochastic variable, and its time average $j_{\boldsymbol{d}} = J_{\boldsymbol{d}}/\tau$ satisfies the TUR (3.1) for any choice of $\boldsymbol{d}(\boldsymbol{x})$. In Fig. 3.1, we illustrate a sample trajectory and the corresponding generalized current.

In this chapter, the expression of (3.1) that consists of the rate quantities is studied since it fits to the large deviation analysis in the next section, while in the later chapters we often use the following expression:

$$\sigma \frac{\tau \mathrm{Var}(J_d)}{\langle J_d \rangle^2} \geq 2, \tag{3.6}$$

which consists of the integrated quantities by viewing $\sigma\tau$ as the mean entropy production during the time interval τ. This is because $\mathrm{Var}(j_d)$ diverges in the short-time limit $\tau \to 0$.

3.1.2 Extensions and applications of the TUR

Here, we review the recent development of the TUR. The TUR has been first proposed in biomolecular processes [35]. Rigorous proofs are provided for the long-time TUR ($\tau \to \infty$) for the first time [36], and then for the finite-time TUR in Markov jump processes [37, 52] and overdamped Langevin dynamics [43, 51]. Since then, numerous works have studied the range of applicability, for example, in underdamped Langevin dynamics [53–56], processes under measurement and feedback control [57, 58], periodically driven systems [59–61], and discrete-time systems [62], all of which require some modifications to the original expression (3.1). Moreover, various extensions [63–70] or generalizations [71–75] of the original TUR have been considered. Given these theoretical developments, it is interesting to consider its application. In the following, we give three examples.

Efficiency bound

Since the TUR is a refinement of the second law, it is interesting to consider how the TUR imposes fundamental limits on thermodynamic efficiencies [76, 77].

For example, in Ref. [76], a thermodynamic efficiency of a molecular motor is studied, where the molecular motor walks along a periodic track with velocity v against an external force f. The thermodynamic efficiency is defined by the ratio between the extracted work fv and the rate of chemical energy consumption $\dot{w}_{\mathrm{chem}}$ as $\eta := fv/\dot{w}_{\mathrm{chem}}$. As a consequence of the TUR, η is bounded by

$$\eta \leq \frac{1}{1 + vk_BT/Df}, \tag{3.7}$$

which is strictly tighter than the bound $\eta \leq 1$ given by the second law. Here, T is the temperature, and D is the diffusion coefficient. This bound not only deepens our understanding of the limitation but also provides a useful information on the efficiency in experiments, since the bound consists of quantities measurable through the kinetic motion of the motor.

Optimal engine beyond the TUR

The search for an optimal engine whose efficiency surpasses the original TUR bound is an interesting direction. In order to realize such an engine, we need to violate some of the necessary conditions of the TUR.

An interesting example is a periodically driven system [59, 78]. Since it is not a stationary process, the TUR (3.1) does not necessarily hold. It is shown in Ref. [78] that the following inequality holds when a system is periodically driven by changing some parameters with a frequency ω:

$$\sigma \frac{D_J}{J^2} \geq \left[1 - \omega \frac{J'}{J}\right]^2, \tag{3.8}$$

where J is the mean of the generalized current per period, and D_J is its diffusion coefficient, and $'$ is the derivative with respect to ω. This relation suggests that the TUR bound goes to zero when the current is proportional to the frequency, i.e, $J(\omega) \propto \omega$. Indeed, such an example is presented in Ref. [59], and it is shown that an adiabatic pump system [79–81] can achieve arbitrary precision at arbitrarily low cost.

Estimation of the entropy production

The application of the TUR for the estimation of the entropy production is one of the hot topics recently [43–45]. Since this is the main interest of this thesis, we explain it in detail in the next chapter. For this application, the tightness of the TUR bound becomes an important issue. Thus, in the last section of this chapter, we give a review on this point.

3.2 Derivation of the TUR

In this section, we explain the outline of the proof of the TUR proposed in Refs. [36, 43]. In Sec. 3.2.1, we explain the proof of the TUR in Markov jump processes [36]. In Sec. 3.2.2, we show that the TUR straightforwardly holds in overdamped Langevin dynamics since it is a special limit of Markov jump processes [43].

3.2.1 Markov jump process

Here, we explain the derivation of the long-time TUR in Markov jump processes [36]. The idea is to study the rate function $I(j_d)$ of the generalized current, which is defined by

$$I(j_d) := \lim_{\tau \to \infty} -\frac{1}{\tau} \ln P(J_d = \tau j_d). \tag{3.9}$$

This means that the probability of taking J_d (or corresponding j_d) asymptotically behaves as $e^{-\tau I(j_d)}$ in the long time limit $\tau \to \infty$. The rate function should satisfy $I(j_d) \geq 0$ and take the minimum value of 0 at the stationary value j_d^π, i.e., $I(j_d^\pi) = 0$ so that the probability distribution converges properly. Here, π denotes the value in the stationary

state, and j_d^π can be explicitly written as

$$j_d^\pi = \sum_{y<z} d(y,z)\{\pi(y)r(y,z) - \pi(z)r(z,y)\}. \tag{3.10}$$

As a result of the above properties, we get $I(j_d) = I''(j_d^\pi)(j_d - j_d^\pi)^2 + o\left((j_d - j_d^\pi)^2\right)$ by the Taylor expansion around j_d^π. Since it means that $P(j_d) \sim \exp\left[-\tau I''(j_d^\pi)(j_d - j_d^\pi)^2\right]$ in the long time limit, the probability distribution of j_d converges to the Gaussian distribution with mean $\langle j_d \rangle = j_d^\pi$ and variance $\mathrm{Var}(j_d) = 1/\left(\tau I''(j_d)\right)$, which corresponds to the central limit theorem.

Since it is hard to obtain the analytical expression for $I(j_d)$, we consider to evaluate $I(j_d)$ by deriving a bound. The starting point is the rate function $I(p,j)$ for the empirical density $p_\tau(y) = \frac{1}{\tau}\int_0^\tau \mathrm{d}t\delta_{x(t),y}$ and the empirical current $j_\tau = J_\tau/\tau$ (see Eq. (3.2)), whose analytical expression is obtained in Ref. [82]. Note that $I(p,j)$ is a function of set $\{p(y)\}$ and $\{j(y,z)\}$ for all y and z. Then, the rate function for the generalized current is obtained by the contraction principle, i.e., $I(j_d) = \inf_{p,j} I(p,j)$, where the infimum is taken over all $p(y)$ and $j(y,z)$ that satisfies the conservation law of the current and $\sum_{y,z} d(y,z)j(y,z) = j_d$.

Although $\inf_{p,j} I(p,j)$ is not analytically solvable, it is feasible to obtain a bound. Concretely, a bound on $I(j_d)$ is obtained in Ref. [36] as

$$I(j_d) \leq \frac{(j_d - j_d^\pi)^2}{4(j_d^\pi)^2}\sigma, \tag{3.11}$$

which leads to

$$I''(j_d) \leq \frac{\sigma}{2(j_d^\pi)^2}. \tag{3.12}$$

Therefore, we get the TUR (3.1) by substituting $I''(j_d) = 1/\left(\tau \mathrm{Var}(j_d)\right)$ and $j_d^\pi = \langle j_d \rangle$. The derived inequality is the long-time TUR since $\mathrm{Var}(j_d)$ is the variance obtained in the long-time limit. We note that the finite-time TUR can also be proved in the same manner by considering the large deviation on the number of copy processes, i.e., by preparing N independent finite-length trajectories and considering the rate function for $N \to \infty$ [37].

3.2.2 Overdamped Langevin dynamics

Next, we explain that overdamped Langevin dynamics is a special limit of Markov jump processes, and thus the TUR holds straightforwardly [43]. Here, we slightly extend the discussion in Ref. [43], and consider an n-dimensional Langevin equation with multiplicative noise described by Eq. (2.11) for the latter use in Chap. 5.

We explain a jump process approximation of the Langevin dynamics described by Eq. (2.11). Here, we assume without loss of generality that the diffusion matrix is diagonal by transforming the coordinates properly. The Langevin dynamics can be spatially discretized into a Markov jump process with lattice states, whose lattice spacing is h. We describe the unit vector in the i-th axis as $\boldsymbol{e}_i$, and the transition rates from $\boldsymbol{x}$ to $\boldsymbol{x} \pm h\boldsymbol{e}_i$ as $W_{i,\pm}(\boldsymbol{x})$. Here, $W_{i,\pm}(\boldsymbol{x})$ should be determined so that the first two jump moments match

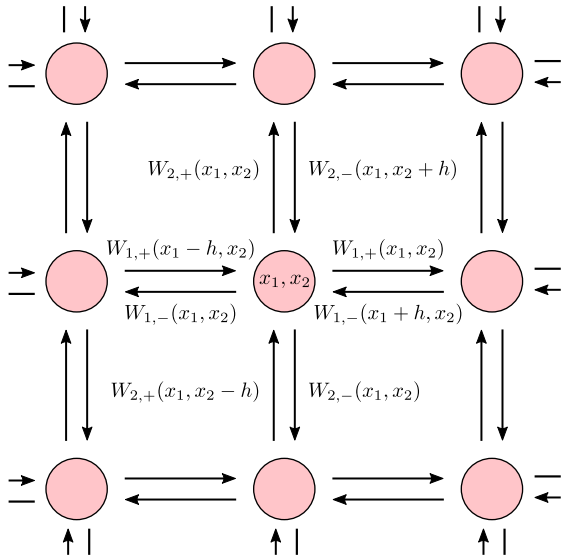

Figure 3.2: A jump process approximation of Langevin dynamics. The continuous space is discretized into lattice states.

the drift term and the diffusion matrix [83]. This can be realized, for example, by requiring

$$h\left(W_{i,+}(\boldsymbol{x}) - W_{i,-}(\boldsymbol{x})\right) = A_i(\boldsymbol{x}), \tag{3.13}$$
$$h^2\left(W_{i,+}(\boldsymbol{x}) + W_{i,-}(\boldsymbol{x})\right) = 2D_{ii}(\boldsymbol{x}). \tag{3.14}$$

Then, we obtain the transition rates of the jump process approximation as

$$W_{i,+}(\boldsymbol{x}) = \frac{A_i(\boldsymbol{x})}{2h} + \frac{D_{ii}(\boldsymbol{x})}{h^2}, \tag{3.15}$$
$$W_{i,-}(\boldsymbol{x}) = -\frac{A_i(\boldsymbol{x})}{2h} + \frac{D_{ii}(\boldsymbol{x})}{h^2}, \tag{3.16}$$

whose dynamics converges to the Langevin dynamics described by Eq. (2.11) as $h \to 0$.

This approximation preserves the structure of thermodynamics. For example, the probability current (2.15) and the thermodynamic force (2.32) are obtained as

$$j^p_{i,+}(\boldsymbol{x}) = p(\boldsymbol{x})W_{i,+}(\boldsymbol{x}) - p(\boldsymbol{x} + h\boldsymbol{e}_i)W_{i,-}(\boldsymbol{x} + h\boldsymbol{e}_i) \tag{3.17a}$$
$$= \left(A_i(\boldsymbol{x})\rho(\boldsymbol{x}) - \nabla_i\left[D_{ii}(\boldsymbol{x})\rho(\boldsymbol{x})\right]\right)h^{n-1} + O(h^n) \tag{3.17b}$$
$$= \mathcal{J}^\rho_i(\boldsymbol{x})h^{n-1} + O(h^2), \tag{3.17c}$$

and

$$F^p_{i,+}(\boldsymbol{x}) = \ln\frac{p(\boldsymbol{x})W_{i,+}(\boldsymbol{x})}{p(\boldsymbol{x} + h\boldsymbol{e}_i)W_{i,-}(\boldsymbol{x} + h\boldsymbol{e}_i)} \tag{3.18a}$$
$$= \frac{1}{D_{ii}(\boldsymbol{x})\rho(\boldsymbol{x})}\left(A_i(\boldsymbol{x})\rho(\boldsymbol{x}) - \nabla_i\left[D_{ii}(\boldsymbol{x})\rho(\boldsymbol{x})\right]\right)h + O(h^2) \tag{3.18b}$$
$$= \mathcal{F}^\rho_i(\boldsymbol{x})h + O(h^2), \tag{3.18c}$$

where $\rho(\boldsymbol{x}) = p(\boldsymbol{x})h^n$. Here, different notations $\rho(\boldsymbol{x})$, $\mathcal{J}_i^\rho(\boldsymbol{x})$ and $\mathcal{F}_i^\rho(\boldsymbol{x})$ are used for the Langevin dynamics to distinguish them from their counterparts, $p(\boldsymbol{x})$, $j_{i,+}^p(\boldsymbol{x})$ and $F_{i,+}^p(\boldsymbol{x})$, in the Markov jump process. The expression of the entropy production rate (2.30) is also obtained as

$$\sum_{\boldsymbol{x},i} j_{i,+}^p(\boldsymbol{x})F_{i,+}^p(\boldsymbol{x}) = \sum_{\boldsymbol{x},i} \mathcal{J}_i^\rho(\boldsymbol{x})\mathcal{F}_i^\rho(\boldsymbol{x})h^n \to \int \mathrm{d}\boldsymbol{x} \sum_i \mathcal{J}_i^\rho(\boldsymbol{x})\mathcal{F}_i^\rho(\boldsymbol{x}). \tag{3.19}$$

Thus, the results obtained in Markov jump processes straightforwardly hold in overdamped Langevin dynamics.

In Ref. [43], the tightness of the long-time TUR in Langevin dynamics is further discussed using this approximation. They concluded that the equality of the long-time TUR is not generally achievable, while the bound on the rate function (3.1) is tighter in Langevin dynamics than in Markov jump processes in the sense that one of inequalities appeared in the derivation of Eq. (3.1) becomes equality.

We note that a similar approximation holds for underdamped Langevin dynamics, while in that case the distinction of transitions between reversible and irreversible contributions is necessary in the approximated jump process [84], and thus results obtained in Markov jump processes cannot be directly applied to underdamped Langevin dynamics.

3.3 Equality condition

Here, we review previous results on the equality condition of the TUR. As explained in the previous section, the equality of the long-time TUR is not generally achievable even in Langevin dynamics. This fact directly means that the equality of the finite-time TUR is not generally achievable both in Langevin dynamics and Markov jump processes. Importantly, however, this fact does not tell anything about particular cases such as the short-time limit, which we study in detail in Chap. 5. Similarly, the equality of the finite-time TUR is known to be always achievable in the equilibrium limit [36, 63, 66, 67] although this is somewhat trivial since σ goes to zero.

Then, it is interesting to question which current makes the bound tightest, even though the equality may not be always achieved. In this thesis, the current that makes the bound tightest is called *hyperaccurate current*, while the current that achieves the equality is called optimal current. The property of the hyperaccurate current is explored in Ref. [85], which can be summarized as follows: (i) If there are any optimal currents, the optimal currents are the entropy production itself or a current proportional to it. (ii) In the long-time limit, if the entropy production is a hyperaccurate current, the entropy production is also an optimal current.

The first statement is proved under the finite-time condition, which means that only the entropy production or a current proportional to it can be optimal currents. Note that there is a degree of freedom in the optimal currents, since the TUR is invariant under the scaling of the coefficient, i.e., $\boldsymbol{d}(\boldsymbol{x})$ and $\tilde{\boldsymbol{d}}(\boldsymbol{x}) := c\boldsymbol{d}(\boldsymbol{x})$ give the same value for $\mathrm{Var}(j_{\boldsymbol{d}})/\langle j_{\boldsymbol{d}}\rangle^2$. In the following, we regard them as an identical current. The second statement is proved under the long-time limit, which means that if the entropy production is not an optimal

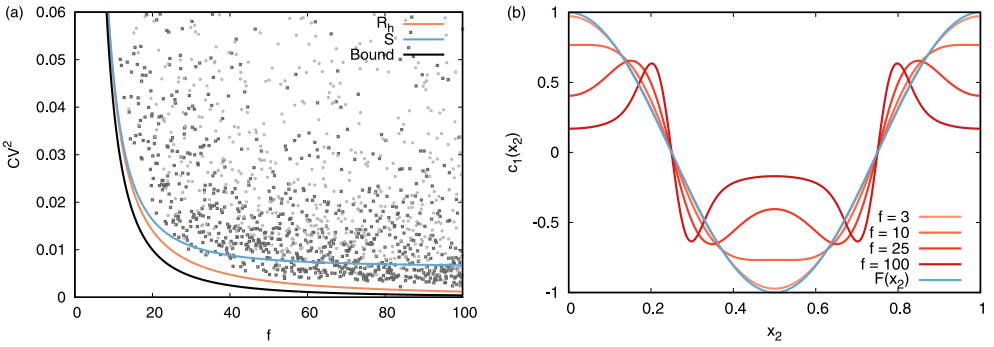

Figure 3.3: The hyperaccurate current and the entropy production in the long-time limit. (a) The bounds set by the hyperaccurate current and the entropy production are studied with a two-dimensional Langevin equation (see Ref. [85] for the details). The horizontal axis is a parameter of the equation, and the vertical axis is the coefficient of variation squared ($\mathrm{CV}^2 := \tau \mathrm{Var}(\mathrm{j_d})/\langle \mathrm{j_d} \rangle^2$). $\mathrm{R_h}$, S and Bound represent the CV^2 of the hyperaccurate current, the entropy production and $2/\sigma$, respectively, and they are calculated using analytical expressions. (b) A coefficient of the hyperaccurate current. As the system becomes away from equilibrium ($f = 0$ is the equilibrium case), the hyperaccurate current deviates from the entropy production. Reprinted figure with permission from [85] (DOI: 10.1103/PhysRevE.100.060102). Copyright 2019 by the American Physical Society.

current, the hyperaccurate current is other than the entropy production.

In Fig. 3.3, the relation between the entropy production and the hyperaccurate current is studied. Since the entropy production is not an optimal current in this example, there is a hyperaccurate current that sets a tighter bound on the entropy production than the entropy production itself, while the hyperaccurate current does not saturate the bound as predicted above. Interestingly, the hyperaccurate current deviates from the entropy production as the system becomes away from equilibrium.

Chapter 4

Estimation of entropy production

In this chapter, we review the methods for estimating the entropy production. In Sec 4.1, we give an overview of this topic. Then, we explain in detail non-invasive methods, which are the main interests of this thesis (from Sec. 4.2 to Sec. 4.4).

4.1 Overview

Recent developments in experimental techniques enable us to study nonequilibrium activity of small systems. Especially, there is great interest in nonequilibrium activity of living systems, since they often operate far from equilibrium by consuming biochemical energy sources such as ATP. For example, a primary cilium, which is a hairlike structure protruding from many eukaryotic cells, shows apparently random behavior (Fig. 4.1B). However, when the dynamics is viewed over some phase space, clockwise probability currents appear (Fig. 4.1C), which suggests that the primary cilium not only fluctuates thermally but also is enhanced by non-equilibrium driving [40].

To quantify nonequilibrium activity beyond the qualitative classification of thermal or active, it is demanded to estimate the entropy production. There are two methods that immediately come to mind on the basis of the following two expressions of the entropy production S:

$$S = S_{\rm sys} + \frac{Q}{T} = \ln \frac{P(\Gamma)}{P^\dagger(\Gamma^\dagger)}. \tag{4.1}$$

One is the direct calorimetric measurement of the heat dissipation Q when the stationary dynamics is considered ($S_{\rm sys} = 0$), but it seems difficult to realize experimentally. The other is based on the detailed fluctuation theorem, which requires estimation of the forward and backward transition probabilities. However, the estimation of these probabilities is not easy in general since it is equivalent to get full cumulant information on probability currents.

As the demand from experiments increases, more sophisticated methods have been considered. One is an invasive method that uses the Harada-Sasa equality [86–88]:

$$\langle \dot{Q} \rangle = \gamma \left\{ \langle v \rangle^2 + \int_{-\infty}^{\infty} {\rm d}f \left[\tilde{C}(f) - 2T\tilde{R}'(f) \right] \right\}, \tag{4.2}$$

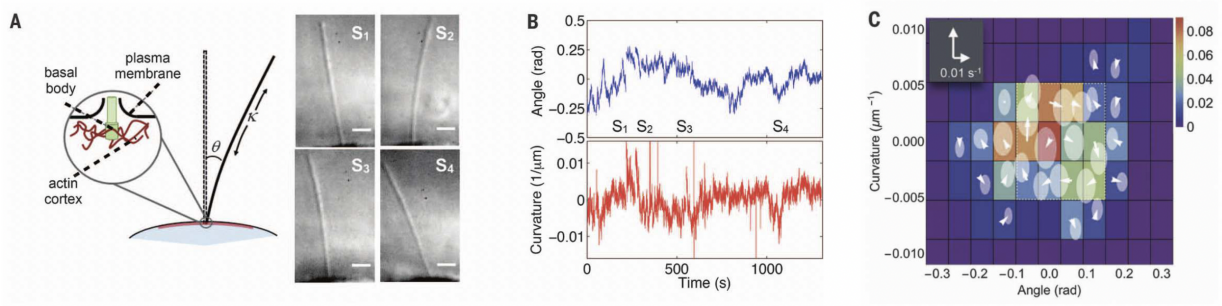

Figure 4.1: Nonequilibrium fluctuation of MDCK-II primary cilia. (A) Schematic of primary cilium and snapshots in the experiment. (B) Time series of the angle θ and the curvature κ. (C) Phase-space probability distribution (color) and flux map (white arrows). From [40] (DOI: 10.1126/science.aac8167). Reprinted with permission from AAAS.

where $\tilde{C}(f)$ is the Fourier transform of the time correlation function of velocity fluctuations, and $\tilde{R}'(f)$ is the real part of the Fourier transform of the response function against perturbation force (see Refs. [86, 87] for the details). The second term represents the violation of the fluctuation-response relation that holds at the equilibrium, i.e., $\tilde{C}(f) = 2T\tilde{R}'(f)$. Since the physical meaning of this equality is clear, it has been applied to several biological systems including F_1-ATPase [50, 89], kinesin [90], and actomyosin [91]. Another characteristic of this approach is that it is applicable to underdamped Langevin equations, which is not the case for most of the other methods introduced in this chapter. However, invasive methods can be challenging in general. For example, it is mentioned in Ref. [90] that they cannot probe all the bandwidth since the kinesin moves out of detectable range in sub-second time scales.

Recently, various non-invasive methods have been developed. They estimate the entropy production solely on the basis of finite-length trajectory data without perturbing systems (note that some of them require additional knowledge of the diffusion matrix). The possibility of a non-invasive method was first proposed in Ref. [92], which is based on the expression (2.30). However, this method involves the estimation of the probability distribution and the mean local velocity over the phase space, which requires a huge amount of data [44]. Currently, there are three methods that seem to be useful in practice: KDE (kernel density estimation) [44], SFI (stochastic force inference) [93], and TUR [43–45]. In the following sections, we explain these methods in detail.

Finally, we give some remarks on other methods for the completeness of this review. In Ref. [94], a method for systems with hidden degrees of freedom is proposed. The method is based on the estimation of the forward and backward multiple jump sequences, in which the timing of jumps is not taken into account. In Ref. [95], as a refinement of Ref. [94], it is shown that the timing of jumps can play a crucial role in detecting broken detailed balance. In Ref. [96], a method that can fully utilize the information contained in multiple transition probabilities is proposed.

4.2 Kernel density estimation

First, we introduce KDE [44]. This method estimates the thermodynamic force by smoothing the data with a kernel function, and estimates the entropy production rate using the obtained thermodynamic force. In Ref. [44], two types of estimators for the entropy production rate were proposed: one is based on the expression (2.30), and the other is based on the TUR. In this section, we review the former estimator, while the TUR-based estimator is described in the last section of this chapter.

The characteristic of KDE is that it is a non-parametric method, which estimates the thermodynamic force using all the data points directly. KDE deals with the problem of underfitting and overfitting by determining an appropriate bandwidth of the kernel function assuming that the data points follow a Gaussian distribution.

In the following, we explain the proposed method, and discuss these points in more detail.

4.2.1 Proposed method

The entropy production rate can be estimated by the following procedure.

KDE (kernel density estimation)

Let us consider the case that we have access to a finite-length trajectory $\{\boldsymbol{x}_0, \boldsymbol{x}_{\Delta t}, ..., \boldsymbol{x}_{\tau_{\rm obs}}(= \boldsymbol{x}_{N\Delta t})\}$ sampled from the stationary dynamics of the following n-dimensional Langevin equation:

$$\dot{\boldsymbol{x}}(t) = \boldsymbol{A}(\boldsymbol{x}) + \sqrt{2\boldsymbol{D}} \cdot \boldsymbol{\eta}(t). \tag{4.3}$$

In KDE, an estimate of the thermodynamic force $\widehat{\boldsymbol{F}}_{\rm sm}(\boldsymbol{x})$ is obtained by smoothing the displacements which occurred around the position $\boldsymbol{x}$:

$$\widehat{F}_{\rm sm}(\boldsymbol{x}) = \frac{\widehat{j}(\boldsymbol{x})\boldsymbol{D}^{-1}}{\widehat{p}(\boldsymbol{x})} \tag{4.4}$$

$$:= \frac{1}{2\Delta t}\frac{\sum_i L(\boldsymbol{x}_{i\Delta t}, \boldsymbol{x})\left[\boldsymbol{x}_{(i+1)\Delta t} - \boldsymbol{x}_{(i-1)\Delta t}\right]\boldsymbol{D}^{-1}}{\sum_i L(\boldsymbol{x}_{i\Delta t}, \boldsymbol{x})}, \tag{4.5}$$

where $L(\boldsymbol{x}', \boldsymbol{x})$ is a kernel function. Concretely, the Epanechnikov kernel is shown to achieve the fastest convergence:

$$L(\boldsymbol{x}_{i\Delta t}, \boldsymbol{x}) \propto \begin{cases} \prod_{j=1}^{n}\left(1 - \frac{(x_{i\Delta t;j} - x_j)^2}{b_j^2}\right), & \forall j \ |x_{i\Delta t,j} - x_j| < b_j, \\ 0, & \text{otherwise}, \end{cases} \tag{4.6}$$

where its bandwidth b_j is determined by

$$\boldsymbol{b} := \left(\frac{4}{N(n+2)}\right)^{\frac{1}{(n+4)}} \frac{\tilde{\boldsymbol{\sigma}}}{0.6745}. \tag{4.7}$$

$\tilde{\boldsymbol{\sigma}}$ is a median absolute deviation:

$$\tilde{\boldsymbol{\sigma}} := \sqrt{\text{median}\left\{|v - \text{median}(v)|\right\} \text{median}\left\{|\boldsymbol{x} - \text{median}(\boldsymbol{x})|\right\}}, \tag{4.8}$$

where v is the magnitude of the velocities, i.e., $v_i = \sqrt{\sum_j (x_{(i+1)\Delta t,j} - x_{i\Delta t,j})^2}/\Delta t$. Note that the diffusion matrix $\boldsymbol{D}$ should be obtained beforehand, and the bandwidth b_j would be optimized under the assumption that the data points follow a Gaussian distribution.

Then, it is proposed to use the following temporal average as an estimator of the entropy production rate:

$$\widehat{\dot{S}}_{\text{ss}}^{\text{temp}} := \frac{1}{\tau_{\text{obs}}} \int_0^{\tau_{\text{obs}}} \widehat{F}_{\text{ss}}(\boldsymbol{x}(t)) \circ \mathrm{d}\boldsymbol{x}(t) \tag{4.9}$$

$$\approx \frac{1}{\tau_{\text{obs}}} \sum_i \widehat{F}_{\text{ss}} \left(\frac{\boldsymbol{x}_{(i+1)\Delta t} + \boldsymbol{x}_{i\Delta t}}{2} \right) \left[\boldsymbol{x}_{(i+1)\Delta t} - \boldsymbol{x}_{i\Delta t} \right]. \tag{4.10}$$

The main idea of KDE is to estimate the thermodynamic force at a position $\boldsymbol{x}$ on the basis of the displacements which occurred around $\boldsymbol{x}$. The bandwidth of the kernel function determines the distance from $\boldsymbol{x}$, within which the displacements of data points are taken into account for calculating $\widehat{\boldsymbol{F}}_{\text{sm}}(\boldsymbol{x})$. Here, there is a bias-variance tradeoff, or a tradeoff between underfitting and overfitting, depending on the bandwidth. Concretely, the estimate becomes vulnerable to the noise when the bandwidth is small, while the estimate becomes biased when the bandwidth is large.

To determine the appropriate bandwidth, KDE would assume that the data points follow a Gaussian distribution, although it was not stated explicitly in Ref. [44]. This is because the expression of (4.7) is usually derived by assuming a Gaussian distribution when the kernel function is used for the probability density estimation [97]. However, the derivation of (4.7) may not be straightforward in this case, since the estimated quantity $\widehat{j}/\widehat{p}$ is not a density. In fact, it was explained as a rule of thumb in Ref. [44]. We show in the later chapter that the convergence of $\widehat{\dot{S}}_{\text{ss}}^{\text{temp}}$ becomes indeed very slow for nonlinear Langevin equations, in which the stationary distributions are distinct from Gaussian distributions.

4.3 Stochastic force inference

Next, we introduce SFI [93], which is based on function fitting. We give a brief review on SFI from the perspective of the estimation of the entropy production rate, while the main focus of Ref. [93] was the estimation of the force, i.e., the drift term $\boldsymbol{A}(\boldsymbol{x})$ when the noise is additive.

The characteristic of SFI compared to KDE is that it does not have any prior assumptions on the equation, and can be used even for nonlinear Langevin equations with multiplicative noise. SFI estimates the thermodynamic force $\boldsymbol{F}(\boldsymbol{x}) = \boldsymbol{\nu}(\boldsymbol{x})\boldsymbol{D}(\boldsymbol{x})^{-1}$ by estimating the diffusion matrix $\boldsymbol{D}(\boldsymbol{x})$ and the mean local velocity $\boldsymbol{\nu}(\boldsymbol{x})$, respectively, each of

which is expressed as a linear combination of basis functions. Then, the entropy production rate is estimated using the obtained thermodynamic force, similarly to KDE. Another interesting characteristic of SFI is that it deals with the problem of underfitting and overfitting by deriving a practical criterion to determine the complexity of the model function. The criterion is based on the Shannon's noisy-channel coding theorem [98].

In the following, we explain the proposed method in the case of a Langevin equation with additive noise. We also explain how to choose an appropriate model function that can avoid underfitting and overfitting.

4.3.1 Proposed method

The entropy production rate can be estimated by the following procedure.

SFI (stochastic force inference)

Let us consider the case that we have access to a finite-length trajectory $\{\boldsymbol{x}_0, \boldsymbol{x}_{\Delta t}, ..., \boldsymbol{x}_{\tau_{\rm obs}}\}$ sampled from the stationary dynamics of the following n-dimensional Langevin equation:

$$\dot{\boldsymbol{x}}(t) = \boldsymbol{A}(\boldsymbol{x}) + \sqrt{2\boldsymbol{D}} \cdot \boldsymbol{\eta}(t). \tag{4.11}$$

In SFI, the force $\boldsymbol{A}(\boldsymbol{x})$ and the mean local velocity $\boldsymbol{\nu}(\boldsymbol{x})$ are estimated as a linear combination of fixed basis functions $\{\widehat{c}_\alpha(\boldsymbol{x})\}$:

$$\widehat{A}_k(\boldsymbol{x}) = \sum_\alpha \widehat{A}_{k\alpha}\widehat{c}_\alpha(\boldsymbol{x}), \tag{4.12}$$

$$\widehat{A}_{k\alpha} = \frac{1}{\tau_{\rm obs}} \sum_i \left\{x_{(i+1)\Delta t,k} - x_{i\Delta t,k}\right\} \widehat{c}_\alpha(\boldsymbol{x}_{i\Delta t}), \tag{4.13}$$

$$\widehat{\nu}_k(\boldsymbol{x}) = \sum_\alpha \widehat{\nu}_{k\alpha}\widehat{c}_\alpha(\boldsymbol{x}), \tag{4.14}$$

$$\widehat{\nu}_{k\alpha} = \frac{1}{\tau_{\rm obs}} \sum_i \left\{x_{(i+1)\Delta t,k} - x_{i\Delta t,k}\right\} \widehat{c}_\alpha\left(\frac{\boldsymbol{x}_{(i+1)\Delta t} + \boldsymbol{x}_{i\Delta t}}{2}\right), \tag{4.15}$$

$$\tag{4.16}$$

where the basis functions $\{\widehat{c}_\alpha(\boldsymbol{x})\}$ are prepared from a set of functions $\{b_\alpha(\boldsymbol{x})\}$ as

$$\widehat{c}_\alpha = \sum_\beta \widehat{B}^{-1/2}_{\alpha\beta} b_\beta, \tag{4.17}$$

$$\widehat{B}_{\alpha\beta} = \frac{\Delta t}{\tau_{\rm obs}} \sum_i b_\alpha(\boldsymbol{x}_{i\Delta t}) b_\beta(\boldsymbol{x}_{i\Delta t}). \tag{4.18}$$

Then, the entropy production rate σ can be estimated by

$$\widehat{\sigma} = \sum_{k,l,\alpha} D^{-1}_{kl} \widehat{\nu}_{k\alpha}\widehat{\nu}_{l\alpha}. \tag{4.19}$$

We note that a Langevin equation with additive noise is considered here, but SFI is also applicable to a system with multiplicative noise. In that case, the diffusion matrix $\boldsymbol{D}(\boldsymbol{x})$ is estimated as a linear combination of basis functions, i.e., $\widehat{D}_{kl}(\boldsymbol{x}) = \sum_\alpha \widehat{D}_{kl\alpha}\widehat{c}_\alpha(\boldsymbol{x})$.

4.3.2 Derivation

We explain how to derive these expressions. First, the basis functions $\{\widehat{c}_\alpha(\boldsymbol{x})\}$ are normalized as

$$\int \mathrm{d}\boldsymbol{x}\ \widehat{c}_\alpha(\boldsymbol{x})\widehat{c}_\beta(\boldsymbol{x})p(\boldsymbol{x}) \approx \frac{\Delta t}{\tau_{\mathrm{obs}}}\sum_i \widehat{c}_\alpha(\boldsymbol{x}_{i\Delta t})\widehat{c}_\beta(\boldsymbol{x}_{i\Delta t}) \tag{4.20a}$$

$$= \delta_{\alpha\beta}, \tag{4.20b}$$

which directly follows from its construction in Eq. (4.17). Then, the expansion coefficients of the force are derived as

$$\widehat{A}_{k\alpha} = \int A_k(\boldsymbol{x})\widehat{c}_\alpha(\boldsymbol{x})p(\boldsymbol{x})\mathrm{d}\boldsymbol{x} \tag{4.21a}$$

$$\approx \frac{\Delta t}{\tau_{\mathrm{obs}}}\sum_i A_k(\boldsymbol{x}_{i\Delta t})\ \widehat{c}_\alpha(\boldsymbol{x}_{i\Delta t}) \tag{4.21b}$$

$$\approx \frac{1}{\tau_{\mathrm{obs}}}\sum_i \left\{x_{(i+1)\Delta t,k} - x_{i\Delta t,k}\right\}\ \widehat{c}_\alpha(\boldsymbol{x}_{i\Delta t}), \tag{4.21c}$$

where we used the fact that $\left\langle x_{(i+1)\Delta t,k} - x_{i\Delta t,k}\right\rangle = A_k(\boldsymbol{x}_{i\Delta t})\Delta t$. Thus, $\widehat{\boldsymbol{A}}(\boldsymbol{x})$ defined in Eq. (4.12) serves as an estimator of the force.

The expansion coefficients of the mean local velocity can also be derived in a similar manner:

$$\widehat{\nu}_{k\alpha} = \int \nu_k(\boldsymbol{x})\widehat{c}_\alpha(\boldsymbol{x})p(\boldsymbol{x})\mathrm{d}\boldsymbol{x} \tag{4.22a}$$

$$= \int \left(A_k(\boldsymbol{x}) - \frac{1}{p(\boldsymbol{x})}D_{kj}\nabla_j p(\boldsymbol{x})\right)\widehat{c}_\alpha(\boldsymbol{x})p(\boldsymbol{x})\mathrm{d}\boldsymbol{x} \tag{4.22b}$$

$$= \int A_k(\boldsymbol{x})(\widehat{c}_\alpha(\boldsymbol{x}) + D_{kj}\nabla_j\widehat{c}_\alpha(\boldsymbol{x}))p(\boldsymbol{x})\mathrm{d}\boldsymbol{x} \tag{4.22c}$$

$$\approx \frac{1}{\tau_{\mathrm{obs}}}\sum_i \left\{x_{(i+1)\Delta t,k} - x_{i\Delta t,k}\right\}\ \left(\widehat{c}_\alpha(\boldsymbol{x}_{i\Delta t}) + \frac{\left\{x_{(i+1)\Delta t,j} - x_{i\Delta t,j}\right\}}{2}\nabla_j\widehat{c}_\alpha(\boldsymbol{x}_{i\Delta t})\right) \tag{4.22d}$$

$$\approx \frac{1}{\tau_{\mathrm{obs}}}\sum_i \left\{x_{(i+1)\Delta t,k} - x_{i\Delta t,k}\right\}\ \widehat{c}_\alpha\left(\frac{\boldsymbol{x}_{(i+1)\Delta t} + \boldsymbol{x}_{i\Delta t}}{2}\right), \tag{4.22e}$$

where we used the fact that $\left\{x_{(i+1)\Delta t,k} - x_{i\Delta t,k}\right\}\left\{x_{(i+1)\Delta t,j} - x_{i\Delta t,j}\right\} = 2D_{kj}\Delta t$. The derivation of $\widehat{\sigma}$ is also straightforward by substituting $\widehat{\boldsymbol{\nu}}(\boldsymbol{x})$ into the expression of the entropy

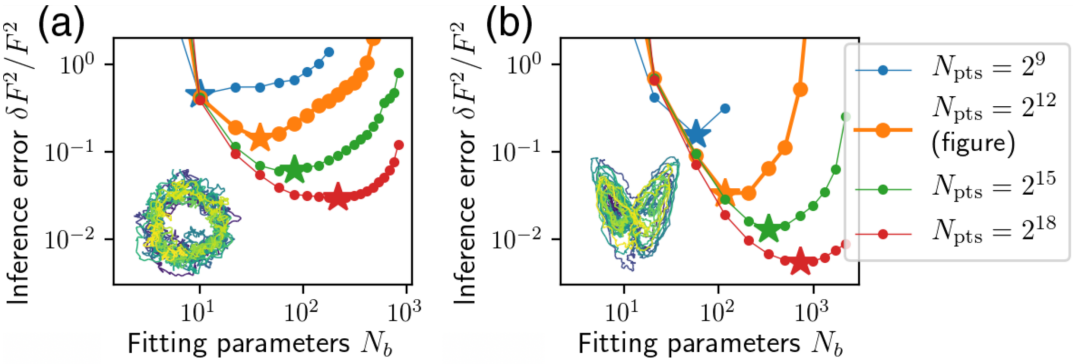

Figure 4.2: Tradeoff between underfitting and overfitting. The horizontal axis is the number of basis functions N_b, and the vertical axis is the mean squared relative error of the estimated force along a trajectory $\delta A^2/A^2 := \left\langle \sum_{k,l} (\widehat{A_k} - A_k) D^{-1}_{kl} (\widehat{A}_l - A_l) \right\rangle / \left\langle \sum_{k,l} \widehat{A}_k D^{-1}_{kl} \widehat{A}_l \right\rangle$(note that a different notation $\delta F^2/F^2$ is used in this figure). Here, a Fourier basis is adopted, and the results with different number of data points $N_{\rm pts} := \tau_{\rm obs}/\Delta t$ are shown. Sample trajectories with $N_{\rm pts} = 2^{12}$ are drawn in each subfigure (see Ref. [93] for the details of the equations). The star symbols are the optimal number N_b^* determined by maximizing $\widehat{I}_b - \delta\widehat{I}_b$. The increase of errors at $N_b < N_b^*$ suggests underfitting, and that at $N_b > N_b^*$ suggests overfitting. Reprinted figure from Ref. [93] (DOI: 10.1103/PhysRevX.10.021009). Figure is available under the terms of the Creative Commons Attribution 4.0 International license.

production rate as

$$\widehat{\sigma} = \int \mathrm{d}\boldsymbol{x} \sum_{kl} D^{-1}_{kl} \widehat{\nu}_k(\boldsymbol{x}) \widehat{\nu}_l(\boldsymbol{x}) p(\boldsymbol{x}) \tag{4.23a}$$

$$\approx \int \mathrm{d}\boldsymbol{x} \sum_{k,l,\alpha,\beta} D^{-1}_{kl} \widehat{\nu}_{k\alpha} \widehat{\nu}_{l\beta} \widehat{c}_\alpha(\boldsymbol{x}) \widehat{c}_\beta(\boldsymbol{x}) p(\boldsymbol{x}) \tag{4.23b}$$

$$\approx \sum_{k,l,\alpha,\beta} D^{-1}_{kl} \widehat{\nu}_{k\alpha} \widehat{\nu}_{l\beta} \sum_i \widehat{c}_\alpha(\boldsymbol{x}_{i\Delta t}) \widehat{c}_\beta(\boldsymbol{x}_{i\Delta t}) \frac{\Delta t}{\tau_{\rm obs}} \tag{4.23c}$$

$$= \sum_{k,l,\alpha} D^{-1}_{kl} \widehat{\nu}_{k\alpha} \widehat{\nu}_{l\alpha}. \tag{4.23d}$$

4.3.3 How to choose an appropriate model function

It is important for an estimator to have a criterion to determine the hyperparameters solely on the basis of data. Here, parameters which need to be determined before the fitting are called hyperparameters. The hyperparameter of SFI is the number of basis functions N_b. In Ref. [93], a practical criterion is proposed to determine the appropriate number. In this subsection, we explain the criterion focusing on the case of the force inference as in Ref. [93].

First of all, we explain how the number of basis functions N_b affects the precision of the force inference. In Fig. 4.2, the N_b dependence of the inference error is plotted. We can see a clear tradeoff between underfitting and overfitting as is the case for many machine learning problems. Here, underfitting occurs at smaller N_b because of the poor representation ability of the model function, while overfitting occurs at larger N_b because the overparametrized model function is easily adapted to the noise of the data. Therefore, our task is to find an appropriate size N_b between the underfitting and overfitting regimes.

We explain the proposed criterion to determine N_b. First, information contained in the trajectory data is estimated by

$$\widehat{I}_b := \frac{\tau_{\mathrm{obs}}}{4} \sum_{k,l,\alpha} D^{-1}_{kl} \widehat{A}_{k\alpha} \widehat{A}_{l\alpha}. \tag{4.24}$$

It is shown in Ref. [93] that $\widehat{I}_b/\tau_{\mathrm{obs}}$ actually estimates the channel capacity of the Gaussian communication channel, where $A_k[\boldsymbol{x}(t)]$ and $\dot{\boldsymbol{x}}(t)$ are viewed as the code word and the output of the channel, respectively. It is further proposed to use $\widehat{I}_b$ as an objective function to maximize by regarding it as information captured by the model function. However, $\widehat{I}_b$ steadily increases as N_b increases, which means that $\widehat{I}_b$ alone cannot detect the overfitting of the model function.

In order to deal with the problem of overfitting, the estimation error of $\widehat{I}_b$ is approximated as

$$\delta\widehat{I}_b \sim \sqrt{2\widehat{I}_b + \frac{N_b^2}{4}}, \tag{4.25}$$

which increases as the model function becomes overfitted to the trajectory data. Therefore, the model function that maximizes $\widehat{I}_b - \delta\widehat{I}_b$ would be balanced between the underfitting and overfitting. Indeed, it is numerically checked that the estimation error becomes minimum at the optimal number N_b^* which maximizes $\widehat{I}_b - \delta\widehat{I}_b$ as shown in Fig. 4.2.

4.4 Thermodynamic uncertainty relation

Finally, we introduce TUR-based estimators [43–45]. The idea of this method is to use the lower bound of the TUR as an estimator of the entropy production rate after performing its maximization:

$$\sigma \geq \max_{\boldsymbol{d}} \frac{2\left\langle J_{\boldsymbol{d}} \right\rangle^2}{\tau \mathrm{Var}(J_{\boldsymbol{d}})}. \tag{4.26}$$

Since it requires only the mean and the variance of a single projected fluctuating current $J_{\boldsymbol{d}}$, we can expect that the estimation converges with small amount of data at the cost that it returns only a lower bound. Indeed, it is suggested in Ref. [44] that a TUR-based estimator shows a good convergence rate at high-dimensional data. Also, its robustness against coarse-graining of dynamics is suggested in Ref. [43].

Recently, this approach has turned out to be promising since it is numerically suggested that the exact estimation is possible by taking the short-time limit of the generalized current

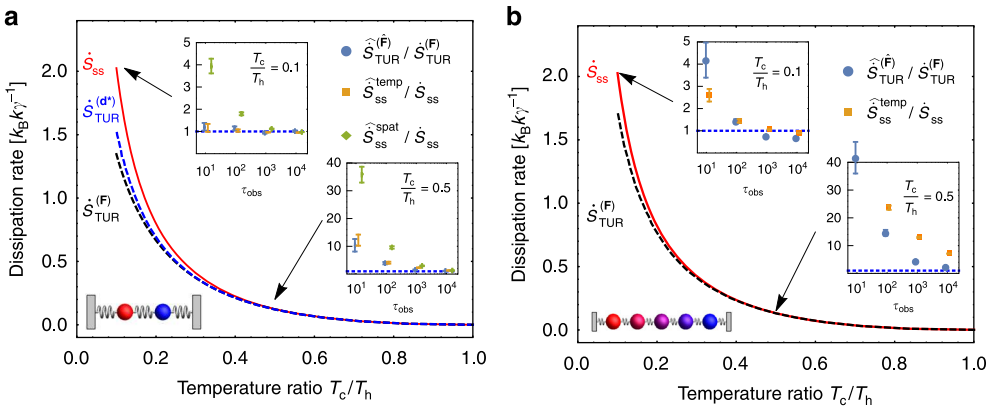

Figure 4.3: Performance of the estimators. Trajectory data generated by two-beads and five-beads models are used for numerical experiments in (a) and (b), respectively (the details of the models can be found in Sec. 5.3). Since the finite-time TUR is used in this study, $\dot{S}^{(\boldsymbol{F})}_{\mathrm{TUR}} < \dot{S}^{(\boldsymbol{d}^*)}_{\mathrm{TUR}} < \dot{S}_{\mathrm{ss}}$ holds (note that $\dot{S}_{\mathrm{ss}} = \sigma$ in our notation). The convergence rate of these estimators are shown as inset plots with error bars reporting standard deviation of 10 independent trials. The result suggests that the TUR-based estimator may be useful for high-dimensional data. Reprinted figure from Ref. [44] (DOI: 10.1038/s41467-019-09631-x). Figure is available under the terms of the Creative Commons Attribution 4.0 International license.

$\tau \to 0$ [45]. This fact is also suggested in a concrete Langevin model with analytical calculation [99]. However, its range of applicability is not well understood since there is no analytical proof under general conditions. In addition, a practical estimation method that leverages the benefit of maximization has not yet been considered.

In the following, we explain these points in detail.

4.4.1 Proposed method

The entropy production rate can be estimated by the following procedure.

TUR-based estimation

Let us consider the case that we have access to a finite-length trajectory $\{\boldsymbol{x}_0, \boldsymbol{x}_{\Delta t}, ..., \boldsymbol{x}_{\tau_{\mathrm{obs}}}\}$ sampled from the stationary dynamics of the following n-dimensional Langevin equation:

$$\dot{\boldsymbol{x}}(t) = \boldsymbol{A}(\boldsymbol{x}) + \sqrt{2\boldsymbol{D}} \cdot \boldsymbol{\eta}(t). \tag{4.27}$$

In this method, a lower bound of the TUR is used as an estimator of the entropy production rate:

$$\widehat{\dot{S}}^{(\boldsymbol{d})}_{\mathrm{TUR}} := \frac{1}{\tau} \frac{2\widehat{\langle J_{\boldsymbol{d}} \rangle}^2}{\widehat{\mathrm{Var}(J_{\boldsymbol{d}})}}, \tag{4.28}$$

where $\widehat{\langle J_{\boldsymbol{d}} \rangle}$ and $\widehat{\mathrm{Var}(J_{\boldsymbol{d}})}$ are the estimated mean and variance of the generalized current. Here, we first divide the whole trajectory into τ_{obs}/τ subtrajectories, and a realization of the generalized current is calculated for each subtrajectory as

$$J_{\boldsymbol{d}} = \sum_i \boldsymbol{d}\left(\frac{\boldsymbol{x}_{(i+1)\Delta t} + \boldsymbol{x}_{i\Delta t}}{2}\right)\left[\boldsymbol{x}_{(i+1)\Delta t} - \boldsymbol{x}_{i\Delta t}\right]. \tag{4.29}$$

Then, the mean and the variance are estimated using the τ_{obs}/τ realizations.

In Ref. [44], two types of functions are adopted for $\boldsymbol{d}(\boldsymbol{x})$. One uses the thermodynamic force $\widehat{\boldsymbol{F}}_{\mathrm{sm}}(\boldsymbol{x})$ estimated by KDE, and this estimator is denoted as $\widehat{\dot{S}}_{\mathrm{TUR}}^{(\widehat{\boldsymbol{F}})}$. The other uses $\boldsymbol{d}^*(\boldsymbol{x})$ which maximizes $\dot{S}_{\mathrm{TUR}}^{(\boldsymbol{d})}$, and this estimator is denoted as $\dot{S}_{\mathrm{TUR}}^{(\boldsymbol{d}^*)}$ (the hat symbol is not attached here since this estimator was studied only with population distribution).

In Fig. 4.3, the performances of the TUR-based estimators are studied. First, the TUR bounds are shown as main plots. Since the finite-time TUR is used in this study, the following inequalities hold:

$$\dot{S}_{\mathrm{TUR}}^{(\boldsymbol{F})} < \dot{S}_{\mathrm{TUR}}^{(\boldsymbol{d}^*)} < \sigma, \tag{4.30}$$

which become tight at the equilibrium limit in accordance with the discussion in Sec. 3.3. We note that these quantities are calculated with the analytical probability distribution, and thus they are not estimated quantities here.

Next, the performance of $\widehat{\dot{S}}_{\mathrm{TUR}}^{(\widehat{\boldsymbol{F}})}$ is compared with that of $\widehat{\dot{S}}_{\mathrm{ss}}^{\mathrm{temp}}$ defined in Sec. 4.2 using finite-length trajectory data in the inset plots of Fig. 4.3. $\widehat{\dot{S}}_{\mathrm{TUR}}^{(\widehat{\boldsymbol{F}})}$ shows the similar convergence rate to $\widehat{\dot{S}}_{\mathrm{ss}}^{\mathrm{temp}}$ overall, but $\widehat{\dot{S}}_{\mathrm{TUR}}^{(\widehat{\boldsymbol{F}})}$ converges much faster at $T_c/T_h = 0.5$ of the five-beads model, which is described by a five-dimensional Langevin equation (the details of the model can be found in Sec. 5.3). On the basis of the result, it is argued that TUR-based estimators may have some advantages for weakly driven high-dimensional Langevin equations. We note that although $\dot{S}_{\mathrm{TUR}}^{(\boldsymbol{d}^*)}$ should be better for estimating the entropy production rate, a practical estimator that includes the maximization process is not proposed in Ref. [44].

There is a clear drawback for the TUR-based estimators that they only return lower bounds on the entropy production rate. However, it is recently suggested that the exact estimation is possible even if the state is far from equilibrium by taking the short-time limit of the generalized current [45]:

$$\sigma = \max_{\boldsymbol{d}} \lim_{\tau \to 0} \frac{2\langle J_{\boldsymbol{d}} \rangle^2}{\tau \mathrm{Var}(J_{\boldsymbol{d}})}. \tag{4.31}$$

In Fig. 4.4, the time interval τ dependence of the TUR bounds are shown with several choices of the generalized current. When the time interval is finite, the TUR bounds take similar values. On the other hand, when the short-time limit is considered, the range of values expands and some of the generalized current can achieve the equality. Concretely, the generalized current which is proportional to the entropy production itself achieves the

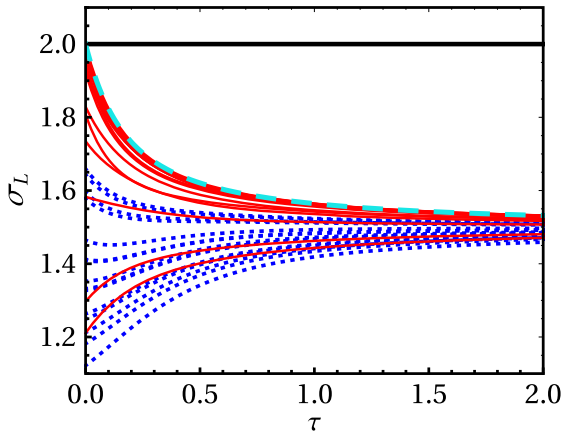

Figure 4.4: The time interval dependence of the TUR bound. The generalized current is chosen as a linear combination of thermodynamic quantities like $J = c_1(\eta_C/T_2)Q_1 + c_2(1/T_2)W + c_3\Delta S_{\mathrm{int}}$, and c_1, c_2 and c_3 are chosen uniformly randomly from $[-1, 1]$ (see Ref. [45] for the details of the model and the notation). $c_1 = c_2 = c_3 = 1$ corresponds to the entropy production (green dashed line). Reprinted figure from Ref. [45] (DOI: 10.1103/PhysRevLett.124.120603). Figure is available under the terms of the Creative Commons Attribution 4.0 International License.

equality (green dashed line in Fig. 4.4).

However, this study relies on the knowledge of the underlying Langevin equation, and a practical estimator that is solely based on trajectory data is not considered.

4.4.2 Remaining issues

As seen above, the TUR-based approach has some promising characteristics. However, the following questions still remain.

- The equality condition of the short-time TUR has not been analytically studied.
- There is no practical estimation method that leverages the benefit of maximization.
- It is still not clear whether the TUR-based approach is good at high-dimensional setups.

In the next chapter, we resolve these remaining issues. For example, we show that the short-time TUR is saturable only in overdamped Langevin dynamics, while this is not the case in general Markov jump processes.

Chapter 5

Estimating entropy production by machine learning

In this chapter, we investigate a theoretical framework for estimation of the entropy production using the short-time TUR with machine learning techniques. Concretely, we resolve the three remaining issues presented in Sec. 4.4.2. In Sec. 5.1, we reveal the equality condition of the short-time TUR analytically. As a result, we show that the short-time TUR gives the exact estimate of the entropy production in overdamped Langevin dynamics, while this is not the case in general Markov jump processes. In Sec. 5.2, we propose a practical estimation method that combines the short-time TUR with machine learning techniques such as the gradient ascent. In Sec. 5.3, we numerically demonstrate that our method performs well even in high-dimensional and non-linear Langevin dynamics. We also find that our method is robust against the choice of the sampling interval in Markov jump processes, while the exact estimation is shown to be impossible. A schematic of our estimation method is shown in Fig. 5.1. The results presented in this chapter are based on our paper [100].

5.1 Short-time TUR

In this section, we formulate the short-time TUR in both Markov jump processes (Sec. 5.1.1) and overdamped Langevin dynamics (Sec. 5.1.2), and reveal its equality condition. We show that the equality is always achievable in overdamped Langevin dynamics, while this is not the case in general Markov jump processes. Our formulation is based on the partial entropy production, which reveals the hierarchy of the bound when the generalized current is constrained. We note that the following discussion holds for non-stationary dynamics, while the estimation in stationary dynamics is addressed in later sections.

5.1.1 Markov jump process

Here we formulate the short-time TUR in Markov jump processes. As in Sec. 3.1, we consider a system with a finite number of states, whose transition rate from y to z is written as $r(y, z)$. Note that we omit the time-dependence for simplicity, and we use

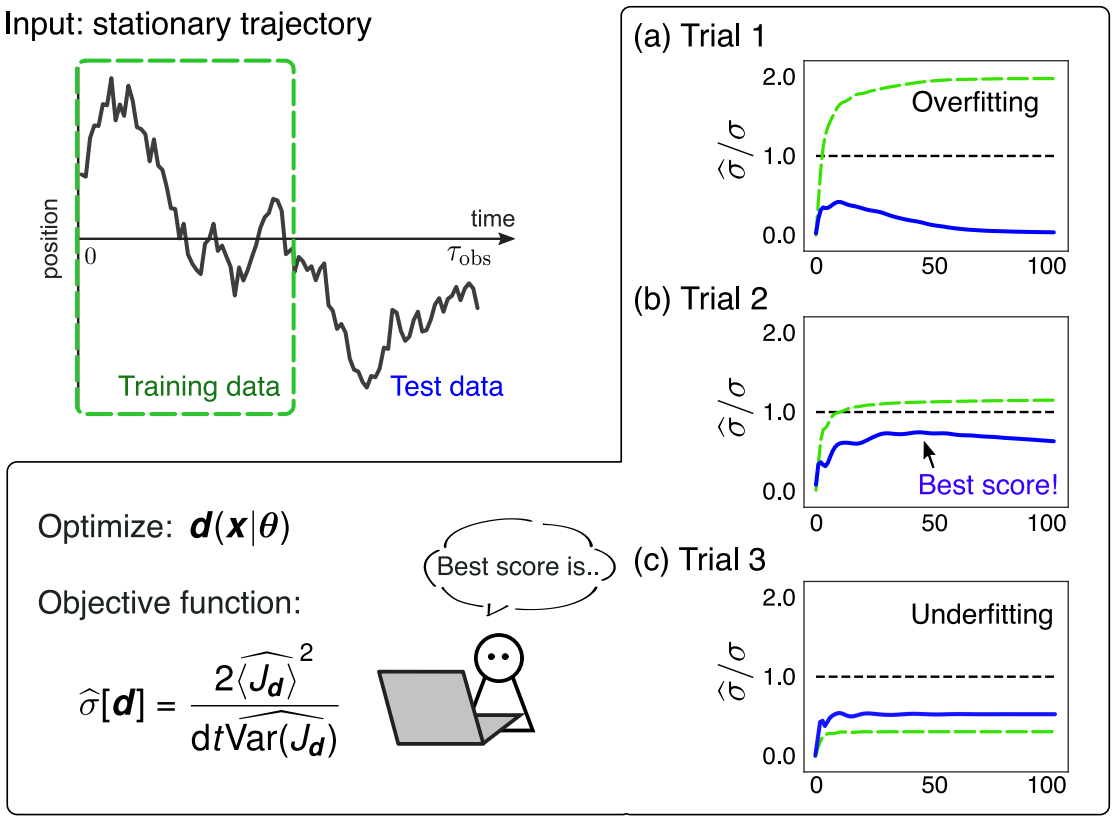

Figure 5.1: Schematic of the estimation method. Our method is solely based on finite-length trajectory data. We use a half of the data to train parameters $\boldsymbol{\theta}$ of a model function $\boldsymbol{d}(\boldsymbol{x}|\boldsymbol{\theta})$ by regarding the short-time TUR bound as the objective function to maximize. We use the other half for testing the generalization performance of the model function. This data splitting scheme is useful for choosing the model function and its parameter values as illustrated in inset plots (a)-(c). The horizontal axis is the iteration step of the gradient ascent, and the vertical axis is the value of the objective function $\widehat{\sigma}$ calculated with training data (green dashed line) and test data (blue line), normalized by the true entropy production rate σ. These plots are based on the binned learning estimator and the two-beads model (see later sections for their explanations). Figure (a) is the case of a model function with many parameters, which leads to overfitting. Figure (c) is the case with a few parameters, which leads to underfitting. Figure (b) is the case with an appropriate number of parameters, where the value $\widehat{\sigma}$ calculated with the test data becomes the largest. We adopt the maximum of the learning curves evaluated with the test data among these trials (described as the best score) as an estimate of the entropy production rate. The system parameters and hyperparameters are as follows: $\tau_{\rm obs} = 10^2, \Delta t = 10^{-3}, T_c/T_h = 0.1, \alpha = 1, \lambda = 0$, and $N_{\rm bin} = (a)10, (b)6, (c)2$. The other parameters are the same as in Fig. 5.4.

quantities defined in Sec. 3.1 without mentioning.

We consider currents in the short-time limit $\tau = \mathrm{d}t$. First, the mean and the variance of the integrated empirical current are explicitly obtained as

$$\begin{aligned} \langle J_{\mathrm{d}t}(y,z)\rangle &= \{p(y)r(y,z) - p(z)r(z,y)\}\,\mathrm{d}t + O(\mathrm{d}t^2), && (5.1)\\ \mathrm{Var}(J_{\mathrm{d}t}(y,z)) &= \{p(y)r(y,z) + p(z)r(z,y)\}\,\mathrm{d}t \\ &- \{p(y)r(y,z) - p(z)r(z,y)\}^2\,\mathrm{d}t^2 + O(\mathrm{d}t^2), && (5.2)\end{aligned}$$

where $p(y)$ is the probability distribution. These expressions are obtained by considering the fact that $J_{\mathrm{d}t}(y,z)$ counts 1 (resp. -1) when a jump occurs from y to z (resp. z to y), and its probability is $p(y)r(y,z)\mathrm{d}t$ (resp. $p(z)r(z,y)\mathrm{d}t$). Meanwhile, we calculated the partial entropy production rate on a transition edge between y and z in Eq. (2.61) as

$$\sigma_{(y,z)} = \{p(y)r(y,z) - p(z)r(z,y)\}\log\frac{p(y)r(y,z)}{p(z)r(z,y)}. \tag{5.3}$$

Then, we claim the following inequality as the short-time TUR on a transition edge between y and z:

$$\sigma_{(y,z)}\frac{\mathrm{d}t\mathrm{Var}(J_{\mathrm{d}t}(y,z))}{\langle J_{\mathrm{d}t}(y,z)\rangle^2} \geq 2. \tag{5.4}$$

The derivation is as follows:

$$\begin{aligned} \sigma_{(y,z)}\frac{\mathrm{d}t\mathrm{Var}(J_{\mathrm{d}t}(y,z))}{\langle J_{\mathrm{d}t}(y,z)\rangle^2} &= \{p(y)r(y,z) - p(z)r(z,y)\}\log\frac{p(y)r(y,z)}{p(z)r(z,y)}\frac{p(y)r(y,z)+p(z)r(z,y)}{\{p(y)r(y,z)-p(z)r(z,y)\}^2} && (5.5a)\\ &\geq 2\frac{\{p(y)r(y,z) - p(z)r(z,y)\}^2}{p(y)r(y,z)+p(z)r(z,y)}\frac{p(y)r(y,z)+p(z)r(z,y)}{\{p(y)r(y,z)-p(z)r(z,y)\}^2} && (5.5b)\\ &= 2, && (5.5c)\end{aligned}$$

where we used the inequality $(a-b)\ln a/b \geq 2(a-b)^2/(a+b)$.

We next formulate the short-time TUR for a subsystem X by summing Eq. (5.4) using the Cauchy-Schwarz inequality. First, the mean and the variance of the (integrated) generalized current are obtained as

$$\begin{aligned} \langle J_d\rangle &= \sum_{y<z} d(y,z)\,\{p(y)r(y,z) - p(z)r(z,y)\}\,\mathrm{d}t, && (5.6)\\ \mathrm{Var}(J_d) &= \sum_{y<z} d(y,z)^2\,\{p(y)r(y,z) + p(z)r(z,y)\}\,\mathrm{d}t. && (5.7)\end{aligned}$$

The partial entropy production rate for a set of transitions $\mathcal{X}$ is obtained as

$$\sigma_X = \sum_{y<z,\ (y,z)\in\mathcal{X}} \{p(y)r(y,z) - p(z)r(z,y)\}\log\frac{p(y)r(y,z)}{p(z)r(z,y)}, \tag{5.8}$$

which is derived by summing $\sigma_{(y,z)}$. Note that σ_X includes information-thermodynamic dissipation and the total entropy production rate, for example. We define $\mathcal{N}$ as a set of transition edges (y,z) such that $d(y,z) \neq 0$. Then, we claim the following inequality as the short-time TUR for the subsystem X.

Result: Short-time TUR for a subsystem

If $\mathcal{N} \subset \mathcal{X}$ is satisfied, the short-time TUR for the subsystem X holds as

$$\sigma_X \frac{\mathrm{d}t\mathrm{Var}(J_d)}{\langle J_d \rangle^2} \geq 2. \tag{5.9}$$

This relation holds for non-stationary dynamics as well as stationary dynamics. The optimal coefficient d^* that makes the bound tightest is given by

$$d^*(y,z) = c\frac{p(y)r(y,z) - p(z)r(z,y)}{p(y)r(y,z) + p(z)r(z,y)}, \tag{5.10}$$

where c is a constant.

The condition $\mathcal{N} \subset \mathcal{X}$ is reasonable since it means that the generalized current should be defined within the subsystem X. The derivation is as follows:

$$\begin{aligned}
&\sigma_X \frac{\mathrm{d}t\mathrm{Var}(J_d)}{\langle J_d \rangle^2} \\
=& \sum_{y<z,\ (y,z)\in\mathcal{X}} \{p(y)r(y,z) - p(z)r(z,y)\} \log \frac{p(y)r(y,z)}{p(z)r(z,y)} \frac{\sum_{y<z} d(y,z)^2 \{p(y)r(y,z) + p(z)r(z,y)\}}{\left[\sum_{y<z} d(y,z)\{p(y)r(y,z) - p(z)r(z,y)\}\right]^2} && \text{(5.11a)} \\
\geq& \sum_{y<z,\ (y,z)\in\mathcal{N}} \frac{2d(y,z)^2\{p(y)r(y,z) - p(z)r(z,y)\}^2}{d(y,z)^2\{p(y)r(y,z) + p(z)r(z,y)\}} \frac{\sum_{y<z,(y,z)\in\mathcal{N}} d(y,z)^2 \{p(y)r(y,z) + p(z)r(z,y)\}}{\left[\sum_{y<z,(y,z)\in\mathcal{N}} d(y,z)\{p(y)r(y,z) - p(z)r(z,y)\}\right]^2} && \text{(5.11b)} \\
\geq& 2, && \text{(5.11c)}
\end{aligned}$$

where we used the Cauchy-Schwarz inequality $\sum a_i^2 \sum b_i^2 \geq (\sum a_i b_i)^2$ in Eq. (5.11c). The bound becomes the tightest when d satisfies the equality condition of the Cauchy-Schwarz inequality, which is explicitly given by Eq. (5.10).

The short-time TUR (5.9) is an extension of the TUR under measurement and feedback control [57,58] to subsystems under autonomous interaction. When we take X as the total system, the short-time TUR becomes the special case ($\tau \to 0$) of the finite-time TUR (3.1). In the following, we mainly consider the total entropy production, and omit the suffix X.

Next, we discuss the achievability of the bound. The equality of the short-time TUR is not achievable in general because of the inequality of Eq. (5.11b). However, we can consider two limits that asymptotically saturate the bound: one is the equilibrium limit, and the other is the Langevin limit. The equilibrium limit is a well known condition for the equality of the finite-time TUR [36,63,66,67], which states that $p(y)r(y,z) - p(z)r(z,y)$ goes to zero for all the pairs of y and z. In this study, we newly find that the Langevin limit also achieves the equality, which states that $\Delta := 2\{p(y)r(y,z) - p(z)r(z,y)\} / \{p(y)r(y,z) + p(z)r(z,y)\}$ goes to zero for all the pairs of y and z. We call it the Langevin limit since it is satisfied in the jump process approximation (3.15). We can check that the inequality (5.11b) becomes

the equality in this limit by the following scaling analysis:

$$\ln \frac{p(y)r(y,z)}{p(z)r(z,y)} = \ln\left(1+\frac{\Delta}{1-\Delta/2}\right) \tag{5.12a}$$
$$= \Delta + O(\Delta^3). \tag{5.12b}$$

This suggests a striking fact that the equality of the short-time TUR is always achievable even if the state is far from equilibrium in Langevin dynamics. Indeed, we reproduce this fact on the basis of the general Langevin equation with multiplicative noise (2.11) in the next subsection.

5.1.2 Overdamped Langevin dynamics

Here, we formulate the short-time TUR in overdamped Langevin dynamics described by Eq. (2.11), and show that the equality is always achievable.

First, the generalized current can be expressed in the short-time limit $\tau = \mathrm{d}t$ as

$$J_{\boldsymbol{d}} = \sum_i d_i(\boldsymbol{x}(t),t)\circ \mathrm{d}x_i(t) \tag{5.13a}$$
$$= \sum_i \frac{d_i(\boldsymbol{x}(t+\mathrm{d}t),t+\mathrm{d}t)-d_i(\boldsymbol{x}(t),t)}{2}\mathrm{d}x_i(t) + d_i(\boldsymbol{x}(t),t)\mathrm{d}x_i(t) \tag{5.13b}$$
$$= \frac{1}{2}\sum_{i,j}\left[\nabla_j d_i(\boldsymbol{x}(t),t)\right]\mathrm{d}x_j(t)\mathrm{d}x_i(t) + \sum_i d_i(\boldsymbol{x}(t),t)\mathrm{d}x_i(t) + O(\mathrm{d}t^{\frac{3}{2}}) \tag{5.13c}$$
$$= \frac{1}{2}\sum_{i,j,l}\left[\nabla_j d_i(\boldsymbol{x}(t),t)\right]B_{il}B_{jl}\mathrm{d}t + \sum_i d_i(\boldsymbol{x}(t),t)(A_i\mathrm{d}t + \sum_l \sqrt{2}B_{il}\mathrm{d}w_l) + O(\mathrm{d}t^{\frac{3}{2}}), \tag{5.13d}$$

where $\mathrm{d}\boldsymbol{w}(t) := \boldsymbol{\eta}(t)\mathrm{d}t$. Then, the ensemble average of the generalized current is obtained as

$$\langle J_{\boldsymbol{d}}\rangle = \int \mathrm{d}\boldsymbol{x}p(\boldsymbol{x},t)\delta(\boldsymbol{x}(t)-\boldsymbol{x})J_{\boldsymbol{d}} \tag{5.14a}$$
$$= \mathrm{d}t\int \mathrm{d}\boldsymbol{x}\sum_{i,j} -d_i(\boldsymbol{x},t)\nabla_j\left[D_{ij}p(\boldsymbol{x},t)\right] + \sum_i d_i(\boldsymbol{x},t)A_i p(\boldsymbol{x},t) \tag{5.14b}$$
$$= \mathrm{d}t\int \mathrm{d}\boldsymbol{x}\boldsymbol{d}(\boldsymbol{x},t)^{\mathsf{T}}\boldsymbol{j}(\boldsymbol{x},t), \tag{5.14c}$$

where $\boldsymbol{j}(\boldsymbol{x},t)$ is the probability current defined in Eq. (2.15). Similarly, the variance of the generalized current is obtained as

$$\mathrm{Var}(J_{\boldsymbol{d}}) = \left\langle J_{\boldsymbol{d}}^2\right\rangle - \langle J_{\boldsymbol{d}}\rangle^2 \tag{5.15a}$$
$$= \int \mathrm{d}\boldsymbol{x}p(\boldsymbol{x},t)\left[\sum_{i,j,l}\nabla_j\left(d_i\right)B_{il}B_{jl}\mathrm{d}t + \sum_i d_i(A_i\mathrm{d}t + \sum_l\sqrt{2}B_{il}\mathrm{d}w_l)\right]^2 - \langle J_{\boldsymbol{d}}\rangle^2 \tag{5.15b}$$
$$= 2\mathrm{d}t\int \mathrm{d}\boldsymbol{x}P\boldsymbol{d}^{\mathsf{T}}\boldsymbol{D}\boldsymbol{d}. \tag{5.15c}$$

Since we assume the overdamped Langevin dynamics, the entropy production rate is given by Eq. (2.31). Then, the short-time TUR can be derived as follows:

$$\sigma \frac{\mathrm{d}t\mathrm{Var}(J_{\boldsymbol{d}})}{\langle J_{\boldsymbol{d}} \rangle^2} = \frac{2\left[\int \mathrm{d}\boldsymbol{x} \frac{\boldsymbol{j}^\mathsf{T}\boldsymbol{D}^{-1}\boldsymbol{D}\boldsymbol{D}^{-1}\boldsymbol{j}}{p}\right]\left[\int \mathrm{d}\boldsymbol{x} p \boldsymbol{d}^\mathsf{T}\boldsymbol{D}\boldsymbol{d}\right]}{\left(\int \mathrm{d}\boldsymbol{x}\boldsymbol{d}^\mathsf{T}\boldsymbol{j}\right)^2} \tag{5.16a}$$

$$\geq \frac{2\left(\int \mathrm{d}\boldsymbol{x}\boldsymbol{j}^\mathsf{T}\boldsymbol{D}^{-1}\boldsymbol{D}\boldsymbol{d}\right)^2}{\left(\int \mathrm{d}\boldsymbol{x}\boldsymbol{d}^\mathsf{T}\boldsymbol{j}\right)^2} \tag{5.16b}$$

$$= 2, \tag{5.16c}$$

where we used the Cauchy-Schwarz inequality in Eq. (5.16b) in terms of the inner product:

$$\langle \boldsymbol{f}, \boldsymbol{g} \rangle := \int \mathrm{d}\boldsymbol{x} \boldsymbol{f}^\mathsf{T}\boldsymbol{D}\boldsymbol{g}. \tag{5.17}$$

The optimal coefficient $\boldsymbol{d}^*(\boldsymbol{x}, t)$ is given by the equality condition of the Cauchy-Schwarz inequality. It is clear from the derivation that the optimal coefficient makes the bound the equality as suggested in the previous subsection.

We summarize the above results as follows.

Result: Short-time TUR in overdamped Langevin dynamics

The short-time TUR holds as

$$\sigma \frac{\mathrm{d}t\mathrm{Var}(J_{\boldsymbol{d}})}{\langle J_{\boldsymbol{d}} \rangle^2} \geq 2. \tag{5.18}$$

This relation holds for non-stationary dynamics as well as stationary dynamics. The optimal coefficient $\boldsymbol{d}^*(\boldsymbol{x}, t)$ that makes the bound the equality is given by

$$\boldsymbol{d}^*(\boldsymbol{x}, t) = c\, \frac{\boldsymbol{j}(\boldsymbol{x}, t)^\mathsf{T}\boldsymbol{D}(\boldsymbol{x}, t)^{-1}}{p(\boldsymbol{x}, t)} \tag{5.19a}$$

$$= c\, \boldsymbol{F}(\boldsymbol{x}, t), \tag{5.19b}$$

where c is a constant and $\boldsymbol{F}(\boldsymbol{x}, t)$ is the thermodynamic force defined in Eq. (2.32).

Related to the short-time TUR, we often use the following formulas. The optimal current with the coefficient $\boldsymbol{d}(\boldsymbol{x}, t) = c\boldsymbol{F}(\boldsymbol{x}, t)$ satisfies

$$J_{\boldsymbol{d}} = c\mathrm{d}S, \tag{5.20}$$

$$\langle J_{\boldsymbol{d}} \rangle = c\sigma \mathrm{d}t, \tag{5.21}$$

$$\mathrm{Var}(J_{\boldsymbol{d}}) = 2c^2\sigma \mathrm{d}t, \tag{5.22}$$

$$\mathrm{Var}(J_{\boldsymbol{d}}^2) \propto \mathrm{d}t^2, \tag{5.23}$$

and thus the constant factor c can be obtained by calculating

$$c = \frac{\mathrm{Var}(J_{\boldsymbol{d}})}{2\langle J_{\boldsymbol{d}} \rangle}. \tag{5.24}$$

We can derive Eqs. (5.20) to (5.22) just by substituting the coefficient into their expressions, and Eq. (5.23) by evaluating $\langle J_{\boldsymbol{d}}^4 \rangle$ and $\langle J_{\boldsymbol{d}}^2 \rangle^2$. Eq. (5.23) actually holds for arbitrary choice of $\boldsymbol{d}(\boldsymbol{x})$, and it will be used in the next chapter.

The short-time TUR also holds for a subsystem. In Langevin dynamics, each coordinate corresponds to a subsystem [49], and the partial entropy production rate σ_i associated with the i-th coordinate is given by

$$\sigma_i = \int \mathrm{d}\boldsymbol{x} F_i(\boldsymbol{x}, t) j_i(\boldsymbol{x}, t). \tag{5.25}$$

Then, the short-time TUR holds for the generalized current satisfying $d_j(\boldsymbol{x}, t) = 0$ for $j \neq i$ as

$$\sigma_i \frac{\mathrm{d}t \mathrm{Var}(J_{d_i})}{\langle J_{d_i} \rangle^2} = \frac{2 \int \mathrm{d}\boldsymbol{x} \frac{j_i D_{ii}^{-1} j_i}{p} \times \int \mathrm{d}\boldsymbol{x} d_i D_{ii} d_i p}{\left(\int \mathrm{d}\boldsymbol{x} d_i j_i \right)^2} \tag{5.26a}$$

$$\geq 2. \tag{5.26b}$$

The short-time TUR for subsystems reveal the hierarchy of the bound when the generalized current is constrained. Here, we view the short-time TUR as an inequality that gives a lower bound on the entropy production rate. For example, when the generalized current is constrained to satisfy $d_j(\boldsymbol{x}, t) = 0$ for $j \neq i$, the maximization of the lower bound only yields σ_i rather than σ:

$$\sigma \geq \sigma_i \geq \frac{2 \langle J_{d_i} \rangle^2}{\mathrm{d}t \mathrm{Var}(J_{d_i})}. \tag{5.27}$$

In another case where the degrees of freedom other than the i-th variable are completely hidden, there is a further constraint on the generalized current that it only depends on x_i, i.e., the coefficient is written as $d_i(x_i, t)$. In this case, the maximization of the lower bound only gives a lower value than σ_i.

5.2 Estimation method

In this section, we present our framework for the estimation of the entropy production in stationary dynamics using the short-time TUR along with machine learning techniques. The aim of our method is to estimate the entropy production solely on the basis of a limited amount of trajectory data. First, we explain the main idea of applying machine learning for the estimation problem in Sec. 5.2.1. After that, we construct practical estimators for Langevin dynamics in Sec. 5.2.2 and for Markov jump processes in Sec. 5.2.3.

5.2.1 General idea

Here, we explain the idea of applying machine learning for the estimation problem. As explained in Sec. 4.4, we can estimate the entropy production rate by finding the optimal

coefficient d^* that maximizes the lower bound of the TUR:

$$d^* := \arg\max \tilde{\sigma}[d], \tag{5.28}$$

$$\tilde{\sigma}[d] := \frac{2\langle J_d\rangle^2}{\mathrm{d}t\mathrm{Var}(J_d)}. \tag{5.29}$$

Then, $\tilde{\sigma}[d^*]$ serves as an estimate of the entropy production rate. As shown in the previous section, if the short-time TUR is used, $\tilde{\sigma}[d^*]$ gives an exact estimate of the entropy production rate in Langevin dynamics.

However, we are interested in the case that only a finite-length trajectory data is available. In this case, we need to estimate the mean and the variance of the generalized current, which generally differ from $\langle J_d\rangle$ and $\mathrm{Var}(J_d)$ calculated with the population distribution. If we write these estimates as $\widehat{\langle J_d\rangle}$ and $\widehat{\mathrm{Var}(J_d)}$, the objective function to maximize is given by

$$\widehat{\sigma}[d] := \frac{2\widehat{\langle J_d\rangle}^2}{\mathrm{d}t\widehat{\mathrm{Var}(J_d)}}, \tag{5.30}$$

where we use the hat symbol for quantities that are estimated by data.

In Langevin dynamics, the coefficient $\boldsymbol{d}(\boldsymbol{x})$ is a vector field over the space, which is equivalent to have an infinite number of parameters. Thus we first consider to approximate the coefficient by some model function $\boldsymbol{d}(\boldsymbol{x}|\boldsymbol{\theta})$ with a finite number of parameters $\boldsymbol{\theta}$. On the other hand, such approximation is not necessary in Markov jump processes in general, since the number of coefficients $d(y,z)$ is already finite. We update the parameters $\boldsymbol{\theta}$ using the gradient ascent by regarding the objective function as a function of $\boldsymbol{\theta}$ defined by $f(\boldsymbol{\theta}) := \widehat{\sigma}[\boldsymbol{d}(\boldsymbol{x}|\boldsymbol{\theta})]$. The basic update rule of the gradient ascent is as follows:

$$\boldsymbol{\theta} \to \boldsymbol{\theta} + \alpha \boldsymbol{\nabla}_{\boldsymbol{\theta}} f(\boldsymbol{\theta}), \tag{5.31}$$

where α is the step size. By repeating the above update, the parameters $\boldsymbol{\theta}$ are expected to converge into the optimal values $\boldsymbol{\theta}^*$ that maximize the objective function, since the gradient ascent updates $\boldsymbol{\theta}$ in the direction where the objective function increases the most. Specifically, we implement an algorithm called Adam [101] for the gradient ascent to improve the convergence.

Here, as is the case for the other estimators reviewed in Chap. 4, the underfitting and the overfitting of the model function to the trajectory data become the major issues. To overcome these problems, we employ ideas from machine learning, namely the data splitting scheme. A schematic of this idea is presented in Fig. 5.1. First, we divide the whole trajectory into two parts: training and test data. We use only the training data for calculating the objective function $\widehat{\sigma}[d]|_{\mathrm{train}}$, and optimize the model function with respect to this objective function. This process is called learning, and the progress of learning is monitored by the objective function calculated with the test data $\widehat{\sigma}[d]|_{\mathrm{test}}$. When the correlation between the training and the test data is negligible, the test value $\widehat{\sigma}[d]|_{\mathrm{test}}$ can evaluate the generalization performance of the trained model function. For example, the learning curve of the test value $\widehat{\sigma}[d]|_{\mathrm{test}}$ often has a peak structure (see the inset plots (a) and (b) in

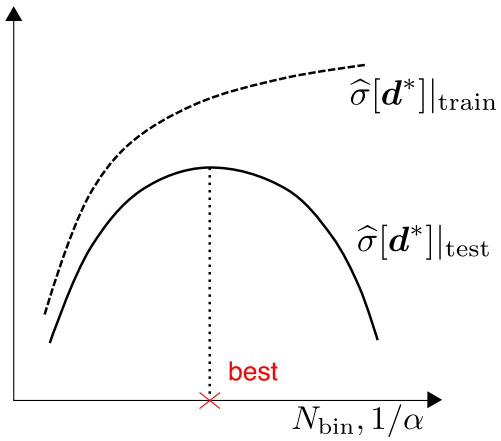

Figure 5.2: Hyperparameter dependence of the test and the training values. Typical behaviors of $\widehat{\sigma}[d^*]|_{\mathrm{train}}$ and $\widehat{\sigma}[d^*]|_{\mathrm{test}}$ are illustrated. For example, as we increase N_{bin} (defined in the next subsection), the model complexity increases. In another case, as we decrease the step size α, the granularity of the gradient ascent improves. In the both cases, the model function becomes easily overfitted to the training data, leading to the decrease of $\widehat{\sigma}[d^*]|_{\mathrm{test}}$. On the other hand, if we decrease N_{bin} or increase α too much, the model function cannot be adapted to the training data, which is called underfitting. We can expect that when $\widehat{\sigma}[d^*]|_{\mathrm{test}}$ is maximized, its value is closest to the true entropy production rate from below.

Fig. 5.1), which suggests that the model function becomes overfitted to the training data after the peak. Thus, we adopt the parameters that maximize the learning curve as the optimal values $\boldsymbol{\theta}^*$, and use $\widehat{\sigma}[d(\boldsymbol{x}|\boldsymbol{\theta}^*)]|_{\mathrm{test}}$ as an estimate of the entropy production rate, which is described as the best score in Fig. 5.1.

How to choose an appropriate model function

The data splitting scheme is also useful for determining an appropriate model function and checking the convergence of the estimate. In the next subsection, we construct practical estimators by assuming some model functions for the coefficient. The parameters of a model function that should be predetermined before the learning are called hyperparameters. Hyperparameters often determine the complexity of a model function, for example, the number of parameters to optimize. It is important for an estimator to have a criterion to determine hyperparameters solely on the basis of trajectory data so that we can avoid the problem of underfitting and overfitting.

For this purpose, the data splitting scheme is useful. As a practical criterion to determine hyperparameters, we propose to use the values that maximize the peak of the test value $\widehat{\sigma}[d^*]|_{\mathrm{test}}$ ($\boldsymbol{d}^* := \boldsymbol{d}(\boldsymbol{x}|\boldsymbol{\theta}^*)$) for the hyperparameters. To explain this idea, we illustrate a typical hyperparameter dependence of the test and the training values in Fig. 5.2. When the complexity of the model function is too low, both of $\widehat{\sigma}[d^*]|_{\mathrm{train}}$ and $\widehat{\sigma}[d^*]|_{\mathrm{test}}$ become small. This is because the model function cannot express the optimal coefficient $c\boldsymbol{F}(\boldsymbol{x})$ well due to the underfitting. As we increase the complexity, both of $\widehat{\sigma}[d^*]|_{\mathrm{train}}$ and $\widehat{\sigma}[d^*]|_{\mathrm{test}}$

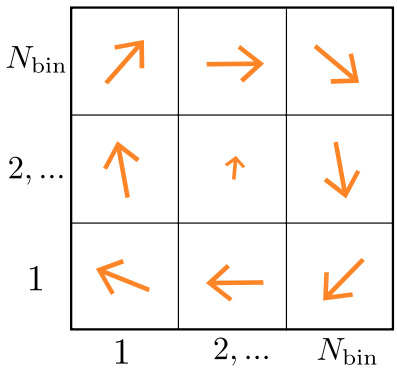

Figure 5.3: Sketch of the model function $\boldsymbol{d}_{\mathrm{bin}}(\boldsymbol{x})$. A two dimensional case is illustrated as an example. It discretize the space into bins aligned on a square lattice. A single vector value is attached to each bin.

increase. However, at some point, the value of $\widehat{\sigma}[d^*]|_{\mathrm{test}}$ starts to decrease. This is because the model function becomes overfitted to the training data, often being away from the optimal coefficient $c\boldsymbol{F}(\boldsymbol{x})$. Thus, the complexity of the model function is expected to be the most appropriate when $\widehat{\sigma}[d^*]|_{\mathrm{test}}$ takes the maximum value. An example of the actual hyperparameter dependence is presented in Fig. 5.10.

The test value $\widehat{\sigma}[d^*]|_{\mathrm{test}}$ usually approaches to the true entropy production rate from below as the length of available trajectory increases. This is because the model function cannot adapt to the fluctuation of the test data, since it is optimized using only the training data. On the other hand, the training value $\widehat{\sigma}[d^*]|_{\mathrm{train}}$ usually approaches to the true entropy production rate from above. Thus, when the values of $\widehat{\sigma}[d^*]|_{\mathrm{test}}$ and $\widehat{\sigma}[d^*]|_{\mathrm{train}}$ are close to each other, they are expected to give a good estimate of the entropy production rate. We note that, however, the test value sometimes becomes higher than the true entropy production rate in practice. We discuss the reason in Sec. 5.5.2.

In short, the estimation procedure can be summarized as in Fig. 5.1. We try several model functions with different hyperparameter values. Then, we adopt the trial that gives the largest test value $\widehat{\sigma}[d^*]|_{\mathrm{test}}$ for the estimation. We use $\widehat{\sigma}[d^*]|_{\mathrm{test}}$ as an estimate of the entropy production rate, and $\boldsymbol{d}^*$ as that of the thermodynamic force $c\boldsymbol{F}(\boldsymbol{x})$.

5.2.2 Estimators in Langevin dynamics

In this subsection, we explain the setup of the estimation, and propose two learning estimators. Here, we focus on the main idea of the learning estimators, and their details are provided in Sec. 5.5.1. We also explain the characteristics of the learning estimators compared to previous methods, KDE (Kernel density estimation) [44] and SFI (Stochastic force inference) [93], which are reviewed in Chap. 4.

We first explain the setup. We consider the case that we have access to a finite-length trajectory $\{\boldsymbol{x}_0, \boldsymbol{x}_{\Delta t}, ..., \boldsymbol{x}_{\tau_{\mathrm{obs}}} (= \boldsymbol{x}_{N\Delta t})\}$ sampled from a stationary Langevin dynamics with interval Δt. The mean and the variance of the generalized current can be computed by

viewing

$$J_{\boldsymbol{d}} = \boldsymbol{d}\left(\frac{\boldsymbol{x}_{i\Delta t} + \boldsymbol{x}_{(i-1)\Delta t}}{2}\right)\left[\boldsymbol{x}_{i\Delta t} - \boldsymbol{x}_{(i-1)\Delta t}\right] \quad (i = 1, 2, ..., N) \tag{5.32}$$

as a realization of the generalized current. We use only the first half ($i = 1, 2, ..., N/2$) for training the model function, and the other half ($i = N/2 + 1, ..., N$) for the evaluation.

As explained in the previous subsection, we construct estimators by assuming model functions for the coefficient. In this study, we consider two types of model functions: one is a histogram-like function $\boldsymbol{d}_{\mathrm{bin}}(\boldsymbol{x})$ and the other is a linear combination of Gaussian functions $\boldsymbol{d}_{\mathrm{Gauss}}(\boldsymbol{x})$. We call the estimators with these model functions the binned learning estimator $\widehat{\sigma}[\boldsymbol{d}_{\mathrm{bin}}]$ and the Gaussian learning estimator $\widehat{\sigma}[\boldsymbol{d}_{\mathrm{Gauss}}]$ respectively.

In the binned learning estimator, the model function $\boldsymbol{d}_{\mathrm{bin}}(\boldsymbol{x})$ discretizes the space into bins aligned on a hypercube lattice, and returns a single vector value for each bin as illustrated in Fig. 5.3. Here, N_{bin} is a hyperparameter that determines the number of divisions in each coordinate. The binned learning estimator is not so data efficient, since the vectors are trained independently of transition data which occurred outside of the same bins. To improve the generalization performance, a regularization term is further added to the objective function so that the vectors change smoothly between neighboring bins. We describe the binned learning estimator with the regularization term as $\widehat{\sigma}^{\lambda}[\boldsymbol{d}_{\mathrm{bin}}]$, denoting the strength of the regularization by λ. We predetermine the hyperparameters α (the step size of the gradient ascent), N_{bin}, and λ, and optimize the vectors of the bins.

In the Gaussian learning estimator, the model function is a linear combination of Gaussian functions whose centers are placed at the centers of the bins. Here, the widths of the Gaussian functions and the coefficients of the linear combination are the parameters to optimize, and α and N_{bin} are the hyperparameters. In contrast to the binned learning estimator, the Gaussian learning estimator shows high generalization performance since the Gaussian functions are trained on the basis of all the transition data. However, the Gaussian learning estimator is computationally costly when the data is high dimensional since the number of Gaussian functions increases exponentially. Thus, we also use a modification of the Gaussian learning estimator in which the centers of Gaussian functions are also parameters to optimize. In this case, the hyperparameters are the number of Gaussian functions N_{Gauss} and α. We describe this estimator as $\widehat{\sigma}[\boldsymbol{d}_{\mathrm{Gauss,m}}]$.

In this study, we mainly use $\widehat{\sigma}[\boldsymbol{d}_{\mathrm{Gauss}}]$, while $\widehat{\sigma}^{\lambda}[\boldsymbol{d}_{\mathrm{bin}}]$ and $\widehat{\sigma}[\boldsymbol{d}_{\mathrm{Gauss,m}}]$ are used for high dimensional setups. Their hyperparameters are determined beforehand using another trajectory data, and the performance of the estimators are evaluated using 10 independent trajectories. In practice, however, we can conduct both of the hyperparameter tuning and the estimation using a single trajectory.

Our approach can be viewed as a method to estimate the thermodynamic force since the optimal coefficient is $c\boldsymbol{F}(\boldsymbol{x})$. In this sense, the learning estimators are related to the previous methods, KDE and SFI. In KDE, the thermodynamic force is estimated by kernel smoothing of the data. The bandwidth of the kernel function is determined by assuming a Gaussian distribution for the data. On the other hand, the learning estimators do not assume any distribution, since $\boldsymbol{d}_{\mathrm{bin}}(\boldsymbol{x})$ and $\boldsymbol{d}_{\mathrm{Gauss}}(\boldsymbol{x})$ can approximate any function when N_{bin} is large enough. Indeed, we show in the next section that the learning estimators outperform the KDE estimators in non-linear Langevin dynamics, where the stationary

distribution becomes non-Gaussian.

In SFI, the thermodynamic force $\boldsymbol{F}(\boldsymbol{x}) = \boldsymbol{\nu}(\boldsymbol{x})\boldsymbol{D}(\boldsymbol{x})^{-1}$ is estimated by fitting of the mean local velocity $\boldsymbol{\nu}(\boldsymbol{x})$ and the diffusion matrix $\boldsymbol{D}(\boldsymbol{x})$, respectively. Since a quantitative comparison between our method and SFI, both of which depend on the choice of the model function, is difficult, we clarify their qualitative difference here. In SFI, the available model function is restricted to a linear combination of fixed basis functions. On the other hand, our method can use an arbitrary function as the model function. There is also a difference in the way to avoid underfitting and overfitting. In SFI, a practical criterion is derived, but its range of applicability may not be clear (see Sec. 4.3.3). On the other hand, our method is simply based on the data splitting scheme, which is enabled by the fact that we have the objective function to maximize.

5.2.3 Estimators in Markov jump processes

In this subsection, we explain the setup of the estimation in Markov jump processes, and propose a learning estimator. We also introduce a simple estimator, which is based on the fluctuation theorem.

We first explain the setup. Similarly to the Langevin case, we suppose that we have access to a finite-length trajectory $\{x_0, x_{\Delta t}, ..., x_{\tau_{\rm obs}}(= x_{N\Delta t})\}$ sampled from a stationary Markov jump process with interval Δt. In Markov jump processes, however, we need to reconstruct the underlying jump sequence from the observed trajectory to compute the generalized current. If we write the reconstructed jump sequence which occurred between $\{x_{i\Delta t}, x_{(i+1)\Delta t}\}$ by $\{x_0^i\,(= x_{i\Delta t})\,, x_1^i, ..., x_{m_i}^i\,\big(= x_{(i+1)\Delta t}\big)\}$, we can compute a generalized current by

$$J_d = \sum_{j=0}^{m_i-1} d(x_j^i, x_{j+1}^i), \tag{5.33}$$

where $d(y,z)$ is a coefficient that satisfies $d(y,z) = -d(z,y)$. Although this is a non-trivial task in general, such a reconstruction is always possible if the system is one-dimensional. For example, we can estmate the sequence by connecting $x_{i\Delta t}$ and $x_{(i+1)\Delta t}$ with the shortest path. We note that such a reconstruction is not necessary if the sampling interval is small enough so that only a single jump occurs at most between the samplings.

Since the coefficient $d(y,z)$ already consists of a finite number of parameters, we use $\widehat{\sigma}[d]$ as an estimator of the entropy production rate without approximating the coefficient. We describe the estimator by $\widehat{\sigma}^{\rm M}[d]$, and compare it with a simple estimator $\widehat{\sigma}^{\rm M}_{\rm simple}$ which is based on the fluctuation theorem. If we write all the reconstructed jump sequences as $\{x_0, x_1, ..., x_m\}$, the simple estimator is defined as follows:

$$\widehat{\sigma}^{\rm M}_{\rm simple} := \sum_{y<z} \Big\{\widehat{j}(y,z) - \widehat{j}(z,y)\Big\} \ln \frac{\widehat{j}(y,z)}{\widehat{j}(z,y)}, \tag{5.34}$$

$$\widehat{j}(y,z) := \frac{1}{\tau_{\rm obs}} \sum_{i=0}^{m-1} \chi_{y,z}(x_i, x_{i+1}), \tag{5.35}$$

where $\chi_{y,z}(x_i, x_{i+1}) := \delta_{y,x_i}\delta_{z,x_{i+1}}$.

5.3 Numerical experiments

In this section, we numerically demonstrate the performance of the learning estimators, and compare them with the KDE estimators $\widehat{\dot{S}}_{\rm ss}^{\rm temp}$ and $\widehat{\sigma}[\widehat{\boldsymbol{F}}_{\rm sm}]$ (see Sec. 4.2 and Sec. 4.4 for their definitions). Here, we use the short-time TUR instead of the finite-time TUR for $\widehat{\dot{S}}_{\rm TUR}^{(\widehat{\boldsymbol{F}})}$, and thus a different notation $\widehat{\sigma}[\widehat{\boldsymbol{F}}_{\rm sm}]$ from $\widehat{\dot{S}}_{\rm TUR}^{(\widehat{\boldsymbol{F}})}$ is used in this section. We use the following three models for the demonstration: (i) N-beads model ($N = 2, 5, 10, 15$), (ii) Mexican-hat potential model, and (iii) one-dimensional hopping model. For the N-beads model, which is an N-dimensional linear Langevin equation, we show that both the estimators show similar convergence for $N = 2$, while the learning estimators outperform the KDE estimators for the higher-dimensional cases. For the Mexican-hat potential model, which is a two-dimensional nonlinear Langevin equation, we show that the learning estimator $\widehat{\sigma}[\boldsymbol{d}_{\rm Gauss}]$ outperforms the KDE estimators. This is because the learning estimator does not assume any distribution on data, while this is not the case for the KDE estimators. For the one-dimensional hopping model, we confirm that the learning estimator gives only a lower bound on the entropy production rate, and the estimate becomes exact in the equilibrium and the Langevin limits. We also find that the learning estimator is robust against the choice of the sampling interval.

5.3.1 N-beads model

In this subsection, we compare the learning estimators with the KDE estimators using the N-beads model described by an N-dimensional linear Langevin equation. We show that the learning estimators and the KDE estimators show similar convergence for $N = 2$, while the learning estimators outperform the KDE estimators for the higher dimensional setups $N = 5, 10, 15$.

The N-beads model describes the motion of beads which are connected to each other and to the boundary walls by springs with stiffness k (see Fig. 5.4(a) for a schematic). The beads are independently immersed in viscous fluids with temperature T_i, which satisfies $T_i = T_h + (T_c - T_h)(i-1)/(N-1)$ $(i = 1, 2, ..., N)$ with T_c the coldest, T_h the hottest temperatures. The ratio $r := T_c/T_h$ determines the degree of non-equilibrium, and the system is in equilibrium at $r = 1$. When $T_c < T_h$, the heat is dissipated into or absorbed from the fluids though the friction γ.

The displacements of the beads from their equilibrium positions are described by an N-dimensional linear Langevin equation. For example, the two-beads model is described by

$$\dot{\boldsymbol{x}}(t) = A\boldsymbol{x}(t) + F\boldsymbol{\eta}(t), \tag{5.36}$$

$$A = \begin{pmatrix} -2k/\gamma & k/\gamma \\ k/\gamma & -2k/\gamma \end{pmatrix}, \tag{5.37}$$

$$F = \begin{pmatrix} \sqrt{2T_h/\gamma} & 0 \\ 0 & \sqrt{2T_c/\gamma}, \end{pmatrix}. \tag{5.38}$$

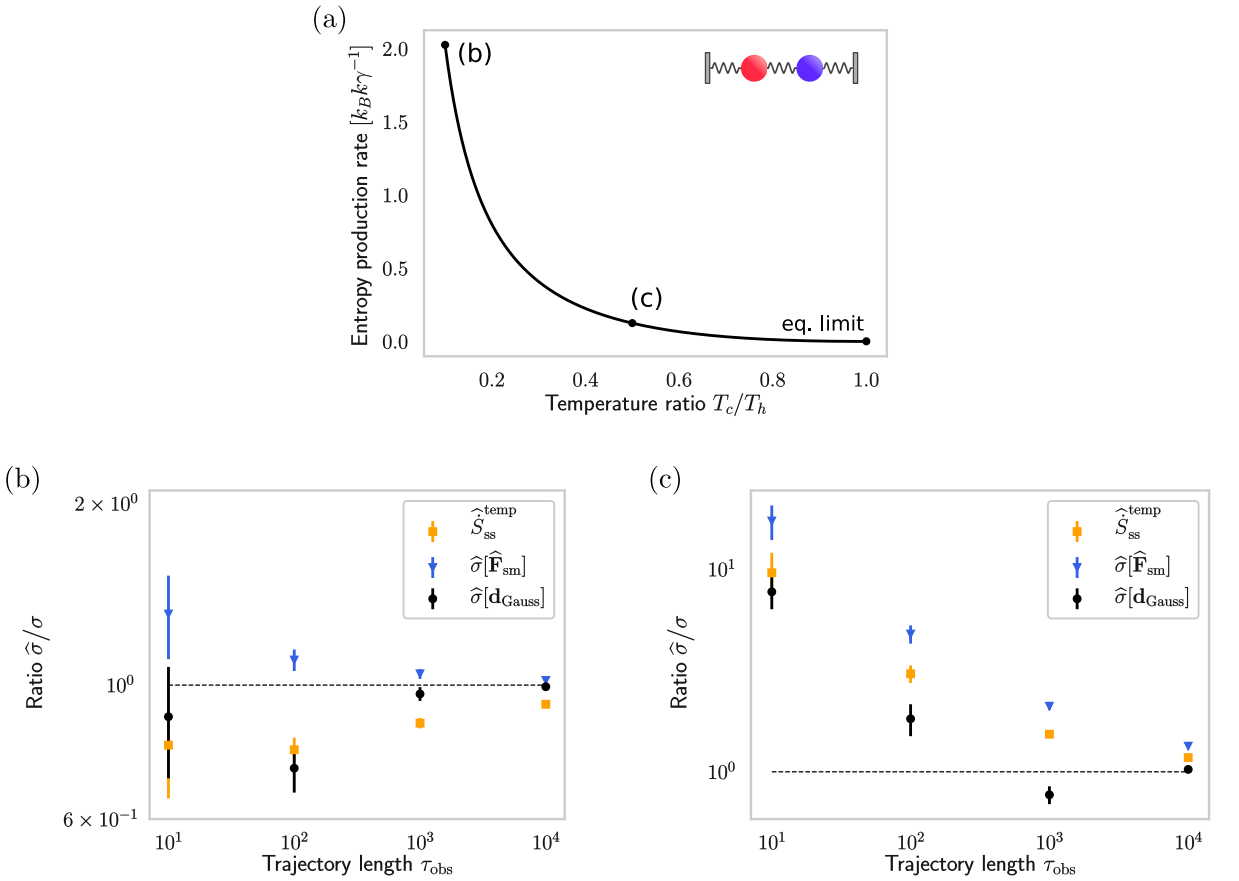

Figure 5.4: Numerical experiment with the two-beads model. (a) Temperature ratio versus the entropy production rate. (b)(c) Performance of the estimators at (b) $T_c/T_h = 0.1$ and (c) $T_c/T_h = 0.5$ with $\widehat{\dot{S}}^{\rm temp}_{\rm ss}$ (yellow squares), $\widehat{\sigma}[\widehat{\boldsymbol{F}}_{\rm sm}]$ (blue triangles), and $\widehat{\sigma}[\boldsymbol{d}_{\rm Gauss}]$ (black circles). The system parameters are set to $k = \gamma = 1$, $T_h = 250$, and $\Delta t = 10^{-3}$. The mean and its standard deviation of 10 independent trials are plotted. Reprinted figure with permission from Ref. [100] (DOI: 10.1103/PhysRevE.101.062106). Copyright 2020 by the American Physical Society.

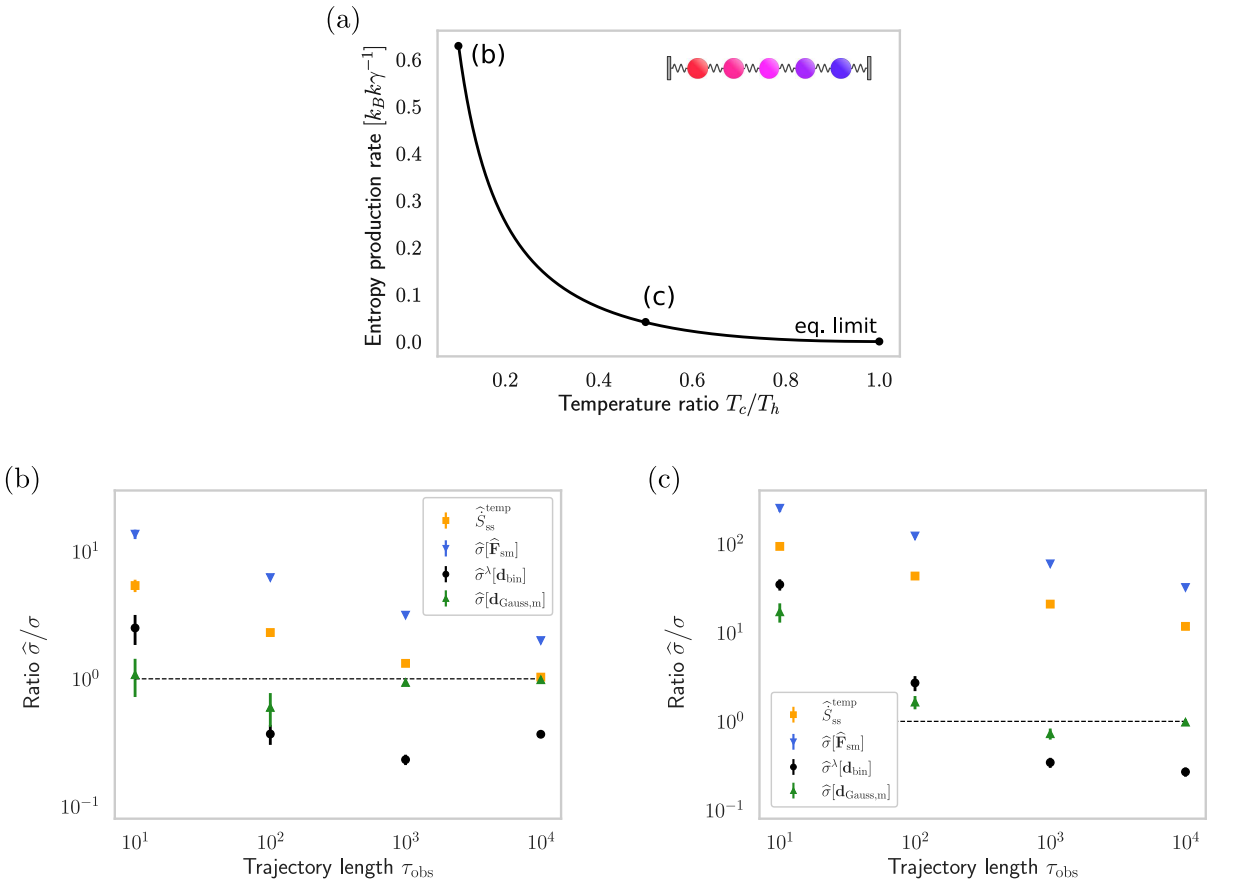

Figure 5.5: Numerical experiment with the five-beads model. (a) Temperature ratio versus the entropy production rate. (b)(c) Performance of the estimators at (b) $T_c/T_h = 0.1$ and (c) $T_c/T_h = 0.5$ with $\widehat{\dot{S}}_{\rm ss}^{\rm temp}$ (yellow squares), $\widehat{\sigma}[\widehat{\boldsymbol{F}}_{\rm sm}]$ (blue triangles), $\widehat{\sigma}^{\lambda}[\boldsymbol{d}_{\rm bin}]$ (black circles), and $\widehat{\sigma}[\boldsymbol{d}_{\rm Gauss,m}]$ (green triangles). The system parameters are set to $k = \gamma = 1$, $T_h = 250$, and $\Delta t = 10^{-3}$. The mean and its standard deviation of 10 independent trials are plotted. Reprinted figure with permission from Ref. [100] (DOI: 10.1103/PhysRevE.101.062106). Copyright 2020 by the American Physical Society.

In higher dimensional setups, A and F can be written as $A_{ij} = \delta_{i,j}(-2k/\gamma) + (\delta_{i,j+1} + \delta_{i+1,j})k/\gamma$ and $F_{i,j} = \delta_{i,j}\sqrt{2T_i/\gamma}$. Since this is a linear Langevin equation, the stationary distribution becomes a Gaussian distribution, and the entropy production rate can be obtained analytically. For example, it is obtained as

$$\sigma = \frac{k\,(T_h - T_c)^2}{4\gamma T_h T_c} \tag{5.39}$$

for the two-beads model, and

$$\sigma = \frac{k(T_h - T_c)^2(111T_h^2 + 430T_hT_c + 111T_c^2)}{495T_hT_c(3T_h + T_c)(T_h + 3T_c)\gamma} \tag{5.40}$$

for the five-beads model [44]. In this study, we use these analytical expressions for $N = 2$ and 5, while we numerically calculate the entropy production rate using the stationary distribution obtained by solving the Riccati equation [47] for $N = 10$ and 15. In the following, we compare the entropy production rate obtained as above with its estimates obtained solely on the basis of a finite-length trajectory.

In Fig. 5.4, we show the results of the numerical experiment with the two-beads model. In Fig. 5.4(a), we show the dependence of the entropy production rate on the temperature ratio r. In Fig. 5.4(b) and (c), we compare the performance of the Gaussian learning estimator $\widehat{\sigma}[\boldsymbol{d}_{\mathrm{Gauss}}]$ with the KDE estimators $\hat{\dot{S}}_{\mathrm{ss}}^{\mathrm{temp}}$ and $\widehat{\sigma}[\widehat{\boldsymbol{F}}_{\mathrm{sm}}]$ at $r = 0.1$ and 0.5. The system parameters are set to $k = \gamma = 1$, $T_h = 250, \Delta t = 10^{-3}$, and thus the number of transitions contained in each trajectory is $10^3\tau_{\mathrm{obs}}$. We find that all the estimators show similar convergence in this setup. The convergence at $r = 0.5$ is worse than that at $r = 0.1$ for all the estimators, since the mean local velocity is small when the system is close to equilibrium, and its detection within the thermal noise becomes difficult.

In Fig. 5.5, we show the results of the numerical experiment with the five-beads model in the same manner as Fig. 5.4. The system parameters are set to $k = \gamma = 1, T_h = 250$, and $\Delta t = 10^{-3}$. Since $\widehat{\sigma}[\boldsymbol{d}_{\mathrm{Gauss}}]$ is computationally costly in the high dimensional setups, $\widehat{\sigma}[\boldsymbol{d}_{\mathrm{Gauss,m}}]$ and $\widehat{\sigma}^{\lambda}[\boldsymbol{d}_{\mathrm{bin}}]$ are used instead. We find that the learning estimators outperform the KDE estimators in this setup. Their difference is significant especially at $r = 0.5$, where the learning estimators with $\tau_{\mathrm{obs}} = 10$ show similar performance as the KDE estimators with $\tau_{\mathrm{obs}} = 10^4$. Thus, we conclude that the learning estimators perform well even at high dimensional setups. In addition, we find that $\widehat{\sigma}[\boldsymbol{d}_{\mathrm{Gauss,m}}]$ shows better performance than $\widehat{\sigma}^{\lambda}[\boldsymbol{d}_{\mathrm{bin}}]$ for all the trajectory lengths. Since we have the criterion to choose the highest test value as an estimate, we can choose $\widehat{\sigma}[\boldsymbol{d}_{\mathrm{Gauss,m}}]$ in practice at large τ_{obs}. Note that this criterion gives a little worse value, i.e., the value of $\widehat{\sigma}^{\lambda}[\boldsymbol{d}_{\mathrm{bin}}]$, at small τ_{obs} in this case, because the test values somehow come above the true entropy production rate. This problem may be avoidable by checking the fluctuation of the learning curve, for example, on the basis of the discussion in Sec. 5.5.2, while we do not pursue this point further in this thesis.

Next, we study the scalability of our approach to higher dimensional data. Here, at the same time, we study how the representation ability of the model function affects the estimation performance, since this is a qualitatively different point of our method from SFI as explained in Sec. 5.2.2. For this purpose, we compare two estimators: one is the

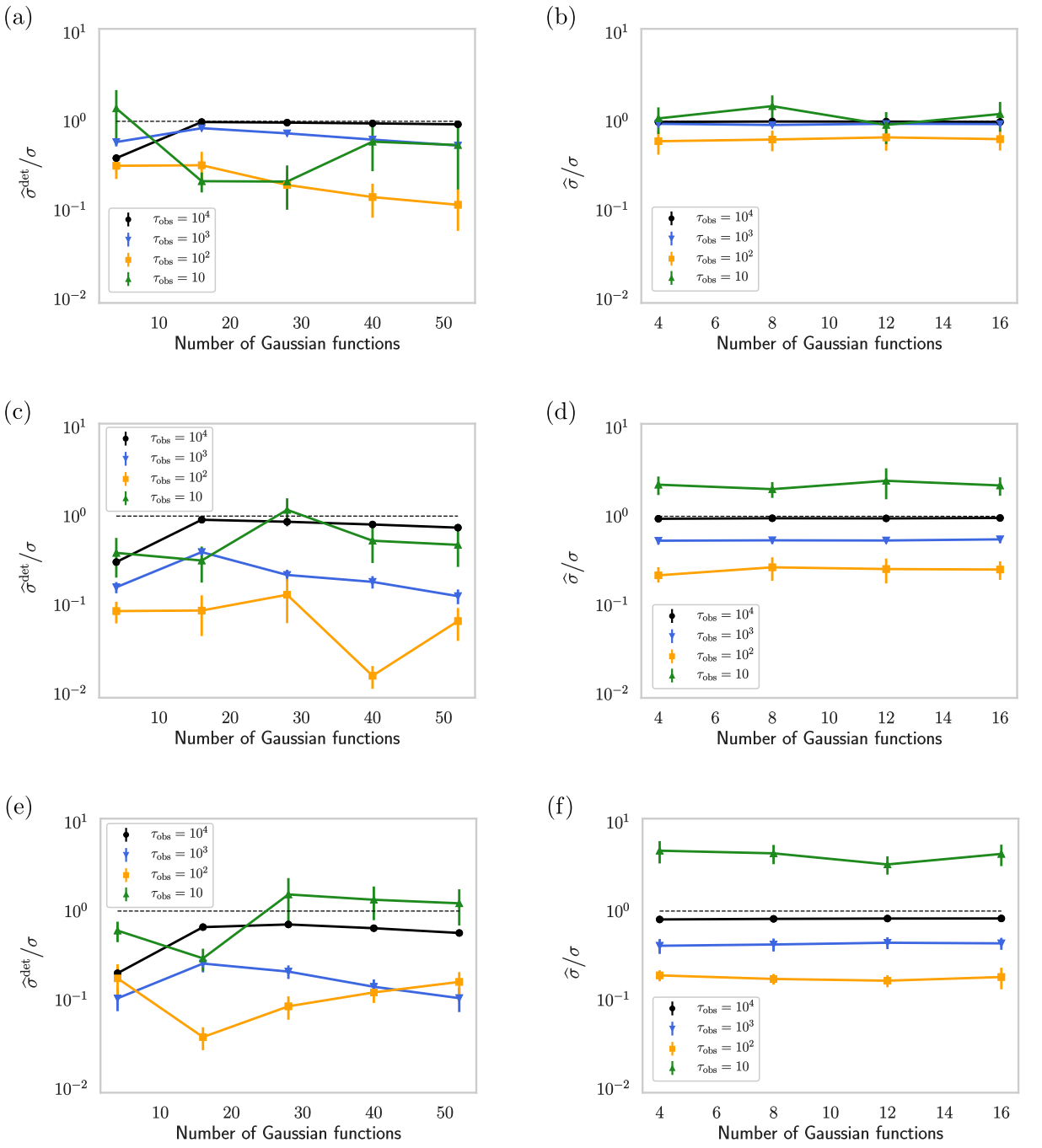

Figure 5.6: Numerical experiment with the N-beads model. (a)(c)(e) The number of the Gaussian functions N_{Gauss} versus the performance of the Gaussian deterministic estimator $\widehat{\sigma}^{\mathrm{det}}[\boldsymbol{d}_{\mathrm{Gauss,m}}]$. (b)(d)(f) The number of the Gaussian functions N_{Gauss} versus the performance of the Gaussian learning estimator $\widehat{\sigma}[\boldsymbol{d}_{\mathrm{Gauss,m}}]$. The dimension N is set to (a)(b) 5, (c)(d) 10, and (e)(f) 15. We use larger values for N_{Gauss} of the Gaussian deterministic estimator, since each Gaussian function has fewer number of parameters. The system parameters are set to $k = \gamma = 1, T_c = 25, T_h = 250$, and $\Delta t = 10^{-3}$. The mean and its standard deviation of 10 independent trials are plotted. Reprinted figure with permission from Ref. [100] (DOI: 10.1103/PhysRevE.101.062106). Copyright 2020 by the American Physical Society.

Gaussian learning estimator $\widehat{\sigma}[\boldsymbol{d}_{\mathrm{Gauss,m}}]$, and the other is the Gaussian deterministic estimator $\widehat{\sigma}^{\mathrm{det}}[\boldsymbol{d}_{\mathrm{Gauss,m}}]$ which optimizes only the coefficient of the linear combination in a deterministic manner [102] (see Sec. 5.5.1 for more details).

In Fig. 5.6, we show the results of the numerical experiment with the N-beads model ($N = 5, 10, 15$). We plot the performance of the estimators changing the number of Gaussian functions. The system parameters are set to $k = \gamma = 1, T_c = 25, T_h = 250$, and $\Delta t = 10^{-3}$. We find that both of the estimators show good convergence even for the 15 dimensional data. The Gaussian learning estimator shows the better convergence, and performs equally well for various choice of N_{Gauss}. Surprisingly, even $N_{\mathrm{Gauss}} = 4$ is enough for all the setups, reflecting the high representation ability of the model function. Thus, we conclude that the learning estimators are scalable to higher dimensional data, and the high representation ability of the model function can improve the estimation.

5.3.2 Mexican-hat potential model

In this subsection, we compare the Gaussian learning estimator with the KDE estimators using a two-dimensional nonlinear Langevin equation named Mexican-hat potential model. We show that the Gaussian learning estimator performs very well, while the KDE estimators do not work well especially when the nonlinearity is large. In addition, we show the results on the estimation of the thermodynamic force.

Here, we consider a two variable (x, y) dynamics described by the following Langevin equation:

$$\dot{\boldsymbol{x}}(t) = -\frac{1}{\gamma}\nabla U(\boldsymbol{x}(t)) + F\boldsymbol{\eta}(t), \tag{5.41}$$

$$U(\boldsymbol{x}) = Ak(r^4 - r^2) + k(x^2 + y^2 - xy), \tag{5.42}$$

$$F = \begin{pmatrix} \sqrt{2T_h/\gamma} & 0 \\ 0 & \sqrt{2T_c/\gamma} \end{pmatrix}, \tag{5.43}$$

where ∇U is the gradient of the potential U, $r = \sqrt{x^2 + y^2}$, and A is a parameter that determines the nonlinearity of this equation. When $A = 0$, this model reduces to the two-beads model. As we increase A, a small hill appears in the center of the potential, and the stationary distribution deviates from the Gaussian distribution (see Fig. 5.7(a) for an illustration of the potential). In this model, we calculate the true entropy production rate using the stationary distribution obtained by the exact diagonalization of the transition matrix of the corresponding Fokker-Planck equation.

In Fig. 5.7, we show the results of the numerical experiment with this model. Figure 5.7 shows the nonlinearity A dependence of the entropy production rate. In Figs. 5.7(b)-(d), we compare the Gaussian learning estimator with the KDE estimators for $A = 10^{-4}, 1$, and 10^2. We find that the Gaussian learning estimator converges the best in all the setups, while the KDE estimators do not work well at highly nonlinear setups, since the KDE estimators assume a Gaussian distribution on the data. On the other hand, the learning estimators works well even if the equation is nonlinear, since they do not assume anything on the distribution.

The learning estimators can also be used for the estimation of the thermodynamic force,

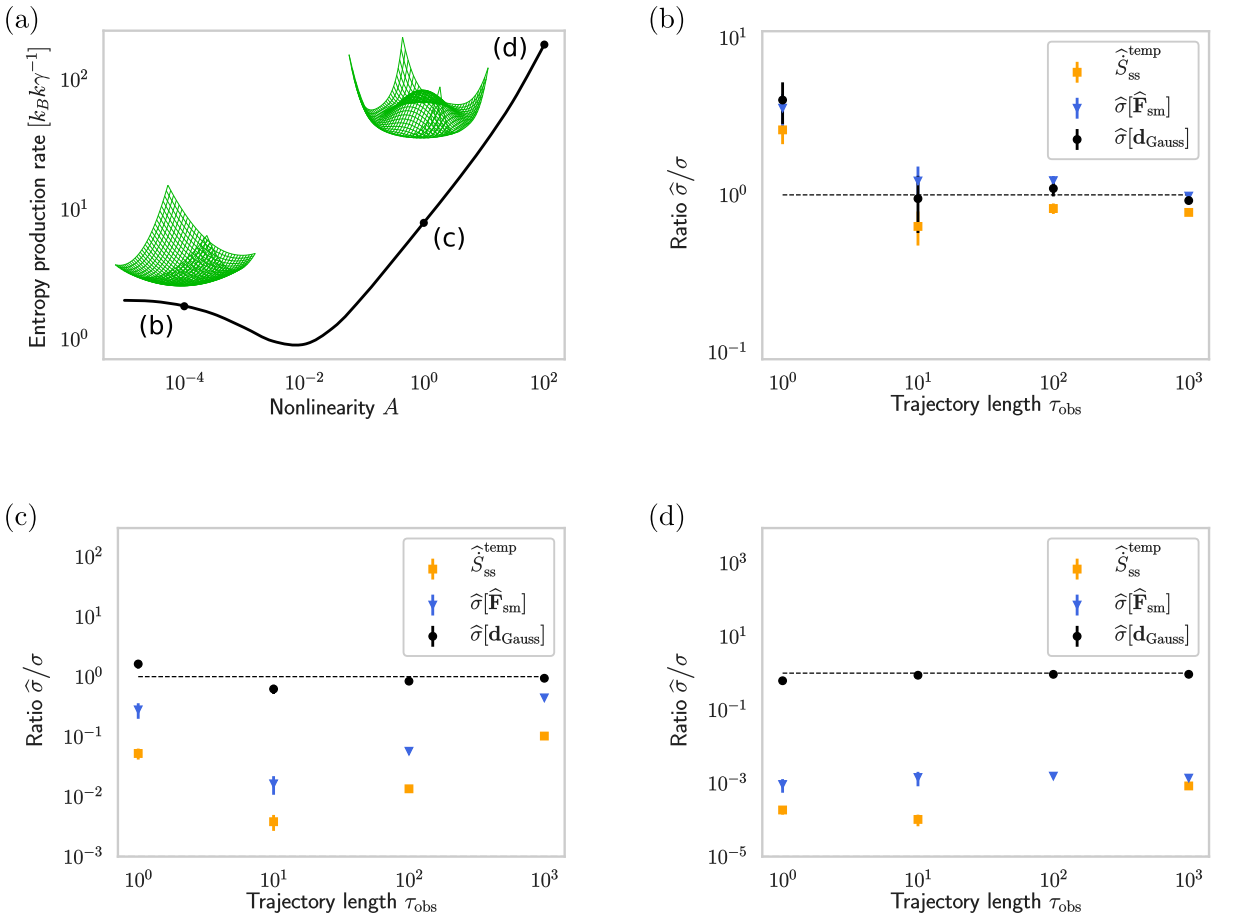

Figure 5.7: Numerical experiment with the Mexican-hat potential model. (a) The nonlinearity A versus the entropy production rate. The model becomes equivalent to the two-beads model at $A = 0$. The potential shapes at $A = 10^{-4}$ and $A = 10^2$ are drawn. (b)(c)(d) Performance of the estimators at (b) $A = 10^{-4}$, (c) $A = 1$, and (d) $A = 10^2$ with $\widehat{\dot{S}}_{\rm ss}^{\rm temp}$ (yellow squares), $\widehat{\sigma}[\widehat{\boldsymbol{F}}_{\rm sm}]$ (blue triangles), and $\widehat{\sigma}[\boldsymbol{d}_{\rm Gauss}]$ (black circles). In (d), a point of $\widehat{\dot{S}}_{\rm ss}^{\rm temp}$ is lacking since it is a negative value. The system parameters are set to $k = \gamma = 1, T_c = 25, T_h = 250$, and $\Delta t = 10^{-4}$. The mean and its standard deviation of 10 independent trials are plotted. Reprinted figure with permission from Ref. [100] (DOI: 10.1103/PhysRevE.101.062106). Copyright 2020 by the American Physical Society.

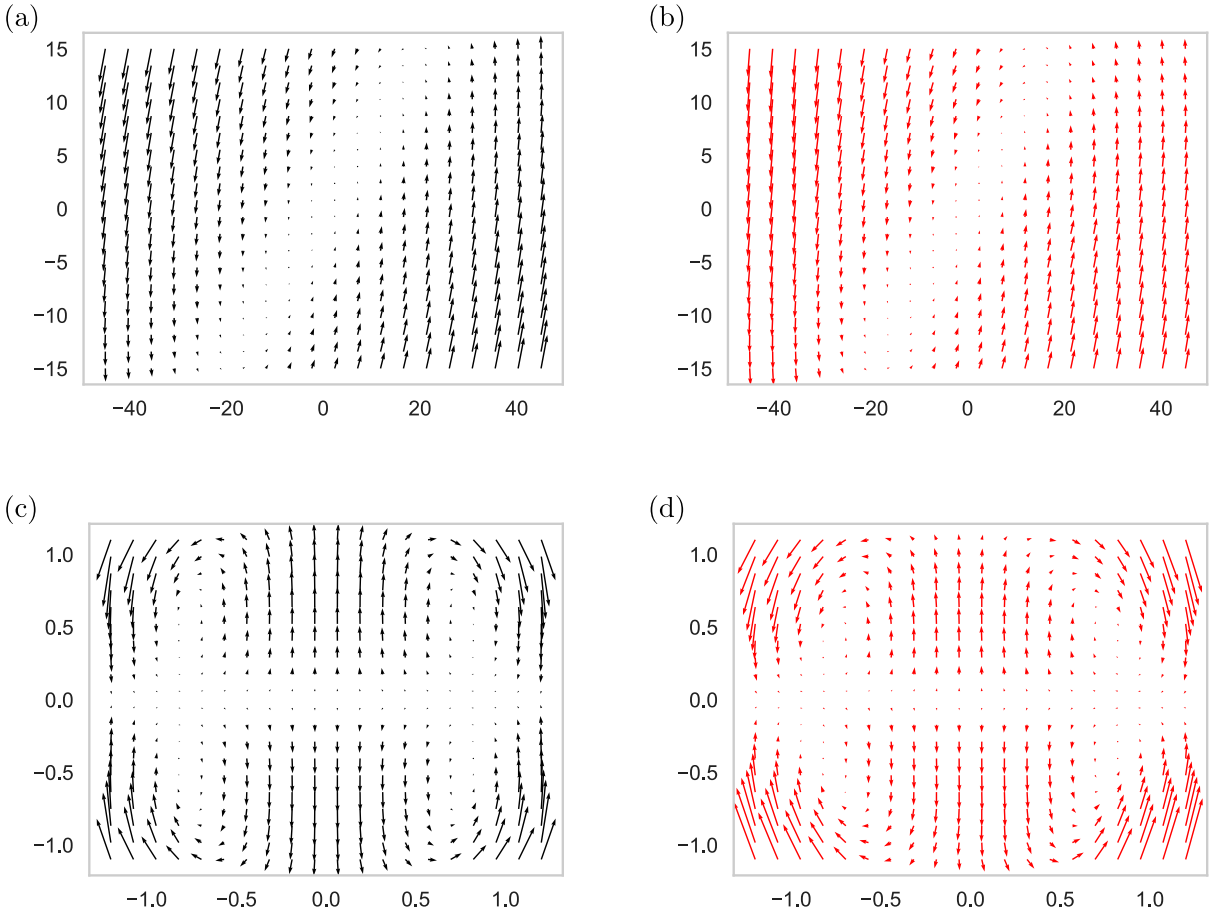

Figure 5.8: Comparison between the true and the estimated thermodynamic force field: (a)(c) Analytically obtained thermodynamic force for the two-beads model in (a) and for the Mexican-hat potential model in (c). (b)(d) Estimated thermodynamic force for the two-beads model in (b) and for the Mexican-hat potential model in (d). The thermodynamic force is estimated by the Gaussian learning estimator. For the two-beads model, we use $r = 0.1, \tau_{\text{obs}} = 10^3$ with the other system parameters the same as in Fig. 5.4. For the Mexican-hat potential model, we use $A = 10^2, \tau_{\text{obs}} = 10^2$ with the other system parameters the same as in Fig. 5.7. Reprinted figure with permission from Ref. [100] (DOI: 10.1103/PhysRevE.101.062106). Copyright 2020 by the American Physical Society.

since the optimal coefficient is proportional to the thermodynamic force $\boldsymbol{d}^*(\boldsymbol{x}) = c\boldsymbol{F}(\boldsymbol{x})$. Here, the constant factor c can be removed by estimating Eq. (5.24). In Fig. 5.8, we compare the true and the estimated thermodynamic force. We can see that the estimated thermodynamic force agrees well with the analytically obtained thermodynamic force.

5.3.3 One-dimensional hopping model

In this subsection, we compare the learning estimator $\widehat{\sigma}^{\mathrm{M}}[d]$ with the simple estimator $\widehat{\sigma}^{\mathrm{M}}_{\mathrm{simple}}$ using a one-dimensional hopping model. First, we check that the optimal estimate of the learning estimator only gives a lower bound on the entropy production rate, which becomes exact in the equilibrium and the Langevin limits. Then, we numerically demonstrate the estimators. We find that the learning estimator is robust against the choice of the sampling interval.

We consider the hopping dynamics over N_{state} states on a one-dimensional ring with radius 1. The transition rate between the neighboring states is given by

$$r(i, i+1) = \frac{D}{h^2} + \frac{A}{h}\left(-\cos\left[hi\right] + f\right), \tag{5.44}$$

$$r(i+1, i) = \frac{D}{h^2}, \tag{5.45}$$

where A determines the degree of non-equilibrium, and $h = 2\pi/N_{\mathrm{state}}$ is the distance between the states. We adopt this model since the dynamics converges to the following Langevin equation in the limit $N_{\mathrm{state}} \to \infty$:

$$\dot{x}(t) = A(-\cos\left[x(t)\right] + f) + \sqrt{2D}\eta(t). \tag{5.46}$$

As explained in Sec. 5.1.1, the short-time TUR does not give the exact estimate in Markov jump processes. In this setup, the optimal estimate $\tilde{\sigma}^M[d^*]$ and the entropy production rate are given by

$$\tilde{\sigma}^M[d^*] = \sum_i \frac{2\left\{p(i)r(i, i+1) - p(i+1)r(i+1, i)\right\}^2}{p(i)r(i, i+1) + p(i+1)r(i+1, i)}, \tag{5.47}$$

$$\sigma = \sum_i \left\{p(i)r(i, i+1) - p(i+1)r(i+1, i)\right\} \ln \frac{p(i)r(i, i+1)}{p(i+1)r(i+1, i)}. \tag{5.48}$$

In Fig. 5.9(a) and (b), we study the behavior of the optimal estimate. We confirm that the optimal estimate is only a lower bound on the entropy production rate in general, while it becomes exact in the equilibrium $A \to 0$ and the Langevin $N_{\mathrm{state}} \to \infty$ limits, which is in accordance with the discussion in Sec. 5.1.1.

Next, we compare the learning estimator with the simple estimator. In Fig. 5.9(c), the convergence of the estimators is studied. We find that the learning estimator shows the better convergence than the simple estimator. In Fig. 5.9(d), the sampling interval Δt dependence of the estimates is studied. Interestingly, as we increase the sampling interval, the simple estimator deviates from the true entropy production rate, while the learning estimator is not affected much. This is because as we increase the sampling interval, we

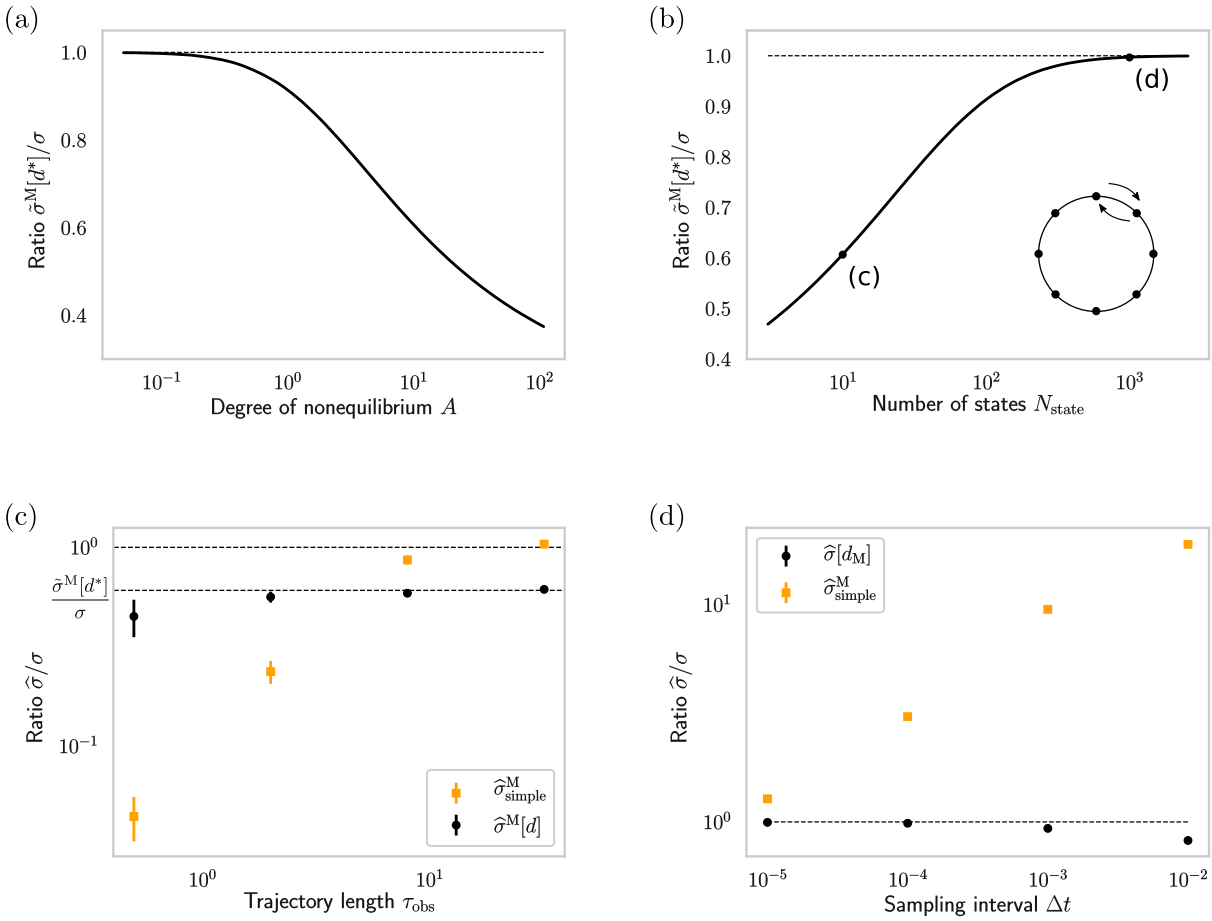

Figure 5.9: Numerical experiment with the one-dimensional hopping model. (a) The degree of non-equilibrium A versus the optimal estimate $\tilde{\sigma}^{\mathrm{M}}[d^*]$ with $N_{\mathrm{state}} = 10$. (b) The number of states N_{state} versus the optimal estimate $\tilde{\sigma}^{\mathrm{M}}[d^*]$ with $A = 10$. The optimal estimate becomes exact in the equilibrium ($A \to 0$) and the Langevin ($N_{\mathrm{state}} \to \infty$) limits. (c) The trajectory length τ_{obs} versus the performance of the estimators with $N_{\mathrm{state}} = 10, A = 10, \Delta t = 10^{-3}$. (d) The sampling interval Δt versus the performance of the estimators with $N_{\mathrm{state}} = 1000, A = 10, \tau_{\mathrm{obs}} = 100$. The other system parameters are set as $D = 1, f = 3$. The mean and its standard deviation of ten independent trials are plotted in (c) and (d). Reprinted figure with permission from Ref. [100] (DOI: 10.1103/PhysRevE.101.062106). Copyright 2020 by the American Physical Society.

fail to reconstruct the underlying dynamics in terms of the back and forth dynamics (for example $1 \to 2 \to 1$), which makes it hard to estimate the transition probability $\widehat{j}(y,z)$ accurately (see Eq. (5.35)). On the other hand, the learning estimator is not affected much since the back and forth dynamics just cancels when we calculate the generalized current (see Eq. (5.33)).

5.4 Conclusions

In this chapter, we have developed a platform for applying machine learning to the estimation of the entropy production using the short-time TUR. We have formulated the estimation method both for Langevin dynamics and Markov jump processes in the stationary state, which can be applied to a wide range of stochastic dynamics including biological systems [50, 103].

First, we have formulated the short-time TUR, and revealed the equality condition by deriving the optimal coefficient as in Eqs. (5.10) and (5.19b). The equality is always achievable in Langevin dynamics, while this is not the case in Markov jump processes. The achievability of the bound in Langevin dynamics is revealed by the scaling analysis in Eq. (5.12b) as well as by the direct evaluation of the general Langevin dynamics described by Eq. (2.11). These results are consistent with the previous results in Sec. 3.3, since the short-time TUR is a special case of the finite-time TUR.

Next, we have constructed the learning estimators [the binned learning estimator $\widehat{\sigma}^{\lambda}[\boldsymbol{d}_{\rm bin}]$ as in Eq. (5.49), the Gaussian learning estimators $\widehat{\sigma}[\boldsymbol{d}_{\rm Gauss}]$, $\widehat{\sigma}[\boldsymbol{d}_{\rm Gauss}]$ as in Eqs. (5.55) and (5.56)] for Langevin dynamics and compared them with the KDE estimators. As a result, we have found that the learning estimators outperform the KDE estimators especially in the high dimensional and nonlinear setups as shown in Figs. 5.5 and 5.7.

We have also formulated the estimation in Markov jump processes, and constructed the learning estimator $\widehat{\sigma}^{\rm M}[d]$ in Sec. 5.2.3. The learning estimator gives an exact estimate only in the equilibrium and the Langevin limits as shown in Fig. 5.9(a) and (b). However, as an advantage of the learning estimator, we have found that it is robust against the choice of the sampling interval, which is of practical importance since the time resolution of a detector is usually limited.

In summary, we have resolved the three remaining issues presented in Sec. 4.4.2. It is an interesting future issue to give a theoretical foundation, for example, on the relation between the convergence and the choice of the model function. The application of the learning estimator for more complex Markov jump processes is also a remaining issue, where the reconstruction of the underlying dynamics becomes a non-trivial task.

5.5 Supplementary to Chapter 5

In this section, we give supplementary information on the learning estimators. In Sec. 5.5.1, we explain the details of the learning estimators from their definition to hyperparameter tuning. In Sec. 5.5.2, we discuss the reason why the test value sometimes becomes larger than the entropy production rate. In Sec. 5.5.3, we study the effect of the measurement

noise on the estimation.

5.5.1 Details of the learning estimators

Here, we explain the binned learning estimator $\widehat{\sigma}^{\lambda}[\boldsymbol{d}_{\rm bin}]$ and the Gaussian learning estimators $\widehat{\sigma}[\boldsymbol{d}_{\rm Gauss}], \widehat{\sigma}[\boldsymbol{d}_{\rm Gauss,m}]$ in detail. We define them by assuming two-dimensional data for simplicity, but their extensions to higher dimensional data are straightforward.

Binned learning estimator

In the binned learning estimator, we assume a histogram-like function $\boldsymbol{d}_{\rm bin}(\boldsymbol{x})$ for the coefficient. Concretely, the model function is defined by

$$\begin{aligned} &\boldsymbol{d}_{\rm bin}(\boldsymbol{x}) := \boldsymbol{d}(i(x), j(y)), \\ &\quad \text{with } i(x) := \left\lceil \frac{x - x_{\rm min}}{b_x} \right\rceil, \ j(y) := \left\lceil \frac{y - y_{\rm min}}{b_y} \right\rceil, \end{aligned} \tag{5.49}$$

where $i(x)$ and $i(y)$ specify the bin, $x_{\rm min}$ and $y_{\rm min}$ are the minimum of the data in each coordinate, b_x and b_y are the widths of the bins, and the brackets denote the ceiling function. Here, the widths are defined as

$$b_x = \frac{x_{\rm max} - x_{\rm min}}{N_{\rm bin}}, \tag{5.50}$$

$$b_y = \frac{y_{\rm max} - y_{\rm min}}{N_{\rm bin}}, \tag{5.51}$$

where $N_{\rm bin}$ is a hyperparameter that determines the number of divisions in each coordinate.

When the gradient ascent is performed, the updates of the vector $\boldsymbol{d}(i, j)$ depend only on the transitions that occurred in the same bin (i, j). To take into account transitions outside of the bins, we introduce a regularization term to the objective function as

$$f(\boldsymbol{d}_{\rm bin}) = \widehat{\sigma}[\boldsymbol{d}_{\rm bin}] - \frac{\lambda}{4}\mathcal{R}(\boldsymbol{d}_{\rm bin}), \tag{5.52}$$

$$\mathcal{R}(\boldsymbol{d}_{\rm bin}) := \sum_{i,j} \sum_{i',j' \in {\rm nn}(i,j)} ||\boldsymbol{d}(i, j) - \boldsymbol{d}(i', j')||^2, \tag{5.53}$$

where ${\rm nn}(i, j) := \{(i + 1, j), (i - 1, j), (i, j + 1), (i, j - 1)\}$ is a set of the nearest neighbors, $||\cdot||$ is the L^2-norm defined by $||\boldsymbol{a}|| = \sqrt{\sum_i a_i^2}$, and λ is a hyperparameter that determines the strength of the regularization. The regularization term can improve the generalization performance of the estimator, since it requires the vectors to change smoothly between neighboring bins which can prevent the model function from being overfitted to training data.

In the numerical experiments, the parameters are initialized by $\{\boldsymbol{d}(i, j)\}_k = {\rm uni}(-1, 1)$ before the gradient ascent, where ${\rm uni}(a, b)$ returns a value x uniformly randomly from $a < x \leq b$. The hyperparameters $\alpha, N_{\rm bin}$ and λ are determined as explained in the end of this subsection, and their values are listed in Table 5.1.

Gaussian learning estimator

In the Gaussian learning estimator, we assume a linear combination of Gaussian functions $\boldsymbol{d}_{\mathrm{Gauss}}(\boldsymbol{x})$ for the coefficient. Concretely, the model function is defined by

$$\{\boldsymbol{d}_{\mathrm{Gauss}}(\boldsymbol{x})\}_k := \sum_{i=1}^{N_{\mathrm{bin}}}\sum_{j=1}^{N_{\mathrm{bin}}} \omega_k(i,j) K_k(\boldsymbol{x};i,j), \tag{5.54}$$

$$K_k(\boldsymbol{x};i,j) := e^{-(\boldsymbol{x}-\bar{\boldsymbol{x}}(i,j))^{\mathsf{T}}\boldsymbol{M}^{(k)}(i,j)^{-1}(\boldsymbol{x}-\bar{\boldsymbol{x}}(i,j))}, \tag{5.55}$$

where $\bar{\boldsymbol{x}}(i,j) = \left(x_{\min} + b_x\left(i-\frac{1}{2}\right), y_{\min} + b_y\left(j-\frac{1}{2}\right)\right)$ are the centers of the Gaussian functions, and $x_{\min}$, $y_{\min}$, b_x and b_y are the same as in the binned learning estimator. $\boldsymbol{M}^{(k)}(i,j)$ is a diagonal matrix whose lth element is $\boldsymbol{M}^{(k)}(i,j)_{ll} = (m_l^{(k)}(i,j))^2$.

Here, $\omega_k(i,j)$ and $m_l^{(k)}(i,j)$ are the parameters to optimize, while α and N_{bin} are the hyperparameters. The parameters are initialized by $\omega_k(i,j) = \mathrm{uni}(-1,1)$ and $m_l^{(k)}(i,j) = \mathrm{uni}(0,1)$ before the gradient ascent, and the hyperparameters are determined as listed in Table 5.1.

In contrast to the binned learning estimator, the Gaussian learning estimator shows high generalization performance as it is. This is because the updates of the Gaussian functions are dependent on all the transition data, and thus the vector field becomes automatically smooth over the space. However, the computational complexity of the Gaussian learning estimator scales $O(N_{\mathrm{bin}}^n)$ for n-dimensional data, reflecting the exponential increase of the Gaussian functions. To deal with this problem, we also consider a modification of the Gaussian learning estimator whose model function $\boldsymbol{d}_{\mathrm{Gauss,m}}(\boldsymbol{x})$ is defined by

$$\{\boldsymbol{d}_{\mathrm{Gauss,m}}(\boldsymbol{x})\}_k := \sum_{i=1}^{N_{\mathrm{Gauss}}} \omega_k(i) K_k(\boldsymbol{x};i), \tag{5.56}$$

$$K_k(\boldsymbol{x};i) := e^{-\left(\boldsymbol{x}-\bar{\boldsymbol{x}}^{(k)}(i)\right)^{\mathsf{T}}\boldsymbol{M}^{(k)}(i)^{-1}\left(\boldsymbol{x}-\bar{\boldsymbol{x}}^{(k)}(i)\right)}, \tag{5.57}$$

where N_{Gauss} is the number of Gaussian functions, and the centers of the Gaussian functions $\bar{\boldsymbol{x}}^{(k)}(i)$ are additionally regarded as the parameters to optimize. This estimator $\widehat{\sigma}[\boldsymbol{d}_{\mathrm{Gauss,m}}(\boldsymbol{x})]$ is used for high dimensional setups in this study. In fact, we find that even $N_{\mathrm{Gauss}} = 4$ is enough for the N-beads model as shown in Fig. 5.6, and thus the estimation can be done with a small computational cost.

In the numerical experiments, the parameters are initialized as follows:

$$w_k(i) = \mathrm{uni}(-1,1), \tag{5.58}$$

$$\bar{x}_l^{(k)}(i) = \mathrm{uni}(x_{\min,l}, x_{\max,l}), \tag{5.59}$$

$$m_l^{(k)}(i) = x_{\max,l} - x_{\min,l}, \tag{5.60}$$

where $x_{\min,l}$ and $x_{\max,l}$ are the minimum and the maximum of the data in the l-th coordinate.

In Fig. 5.6 and Fig. 5.11, we use the Gaussian deterministic estimator [102] which optimizes only the coefficient $\omega_k(i)$ in a deterministic manner. In Fig. 5.6, the Gaussian

deterministic estimator with the model function $\boldsymbol{d}_{\mathrm{Gauss,m}}(\boldsymbol{x})$ is used, where we set $\bar{x}_l^{(k)}(i)$ and $m_l^{(k)}(i)$ as Eqs. (5.59) and (5.60). In Fig. 5.11, the Gaussian deterministic estimator with the model function $\boldsymbol{d}_{\mathrm{Gauss}}(\boldsymbol{x})$ is used, where we set $m_l^{(k)}(i,j) = \sqrt{2}(x_{\max,l} - x_{\min,l})/N_{\mathrm{bin}}$ following the definition in Ref. [102].

Hyperparameter tuning

Here, we explain the hyperparameter tuning of the learning estimators. In Fig. 5.10, we show the hyperparameter dependence of the Gaussian learning estimator. We find that the hyperparameter dependence is monotonic, and thus we can determine their values by changing them in the direction which increases the test value $\widehat{\sigma}[\boldsymbol{d}^*_{\mathrm{Gauss}}]$. The behaviors of the test and the training values are in accordance with the sketch of Fig. 5.2. On the basis of Fig. 5.10(c), we adopt $\alpha = 10$ in this study. It is an interesting future issue to give a theoretical foundation for these behaviors: for example, why α dependence is more significant.

In the same manner, we determine the hyperparameters of all the learning estimators as listed in Table 5.1. For simplicity, the hyperparameters are determined before numerical experiments using other trajectories in this study, but there is no problem for doing both of the hyperparameter tuning and the estimation for a single trajectory data in practice.

5.5.2 Bias of the learning estimators

In this subsection, we discuss the reason why the test value sometimes becomes larger than the entropy production rate. We consider that there are three reasons for this behavior: (i) bias of the short-time TUR, (ii) fluctuation of the gradient ascent, and (iii) correlation between training and test data. To explain these points, we study the behavior of $\widehat{\sigma}[\boldsymbol{F}]$, $\widehat{\sigma}[\boldsymbol{d}_{\mathrm{Gauss}}]|_{\mathrm{test}}$, $\widehat{\sigma}^{\mathrm{det}}[\boldsymbol{d}_{\mathrm{Gauss}}]|_{\mathrm{test}}$, and $\widehat{\sigma}^{\mathrm{det}}[\boldsymbol{d}_{\mathrm{Gauss}}]|_{\mathrm{train}}$ in Fig. 5.11.

First, the short-time TUR is biased in the sense that even if the thermodynamic force $\boldsymbol{F}(\boldsymbol{x})$ is used for the coefficient, $\widehat{\sigma}[\boldsymbol{F}]$ can be systematically shifted from the true entropy production rate. This is because the mean and the variance of the generalized current are estimated with a finite-length trajectory. Indeed, $\widehat{\sigma}[\boldsymbol{F}]$ gives a larger value than the entropy production rate in Fig. 5.11 especially when the trajectory length is small. As a criterion to judge the bias in practice, we propose to compare the mean $\mathrm{Mean}\left[\widehat{\langle J_{\boldsymbol{F}}\rangle}\right]$ and the standard deviation $\mathrm{Std}\left[\widehat{\langle J_{\boldsymbol{F}}\rangle}\right]$ of the estimated entropy production $\widehat{\langle J_{\boldsymbol{F}}\rangle}$:

$$\mathrm{Mean}\left[\widehat{\langle J_{\boldsymbol{F}}\rangle}\right] \approx \widehat{\sigma}\tau, \tag{5.61}$$

$$\mathrm{Std}\left[\widehat{\langle J_{\boldsymbol{F}}\rangle}\right] \approx \sqrt{\frac{2\widehat{\sigma}\tau}{N}}, \tag{5.62}$$

where τ is the time interval of the generalized current ($\tau = \Delta t$ if it is defined by Eq. (5.32)) and N is the number of transitions used for the computation. Here, the standard deviation is derived using $\mathrm{Var}(J_{\boldsymbol{F}}) = 2\sigma\tau$ and the central limit theorem for $\widehat{\langle J_{\boldsymbol{F}}\rangle} = \sum J_{\boldsymbol{F}}/N$. When the standard deviation is larger than the mean, we should be careful of the bias. For

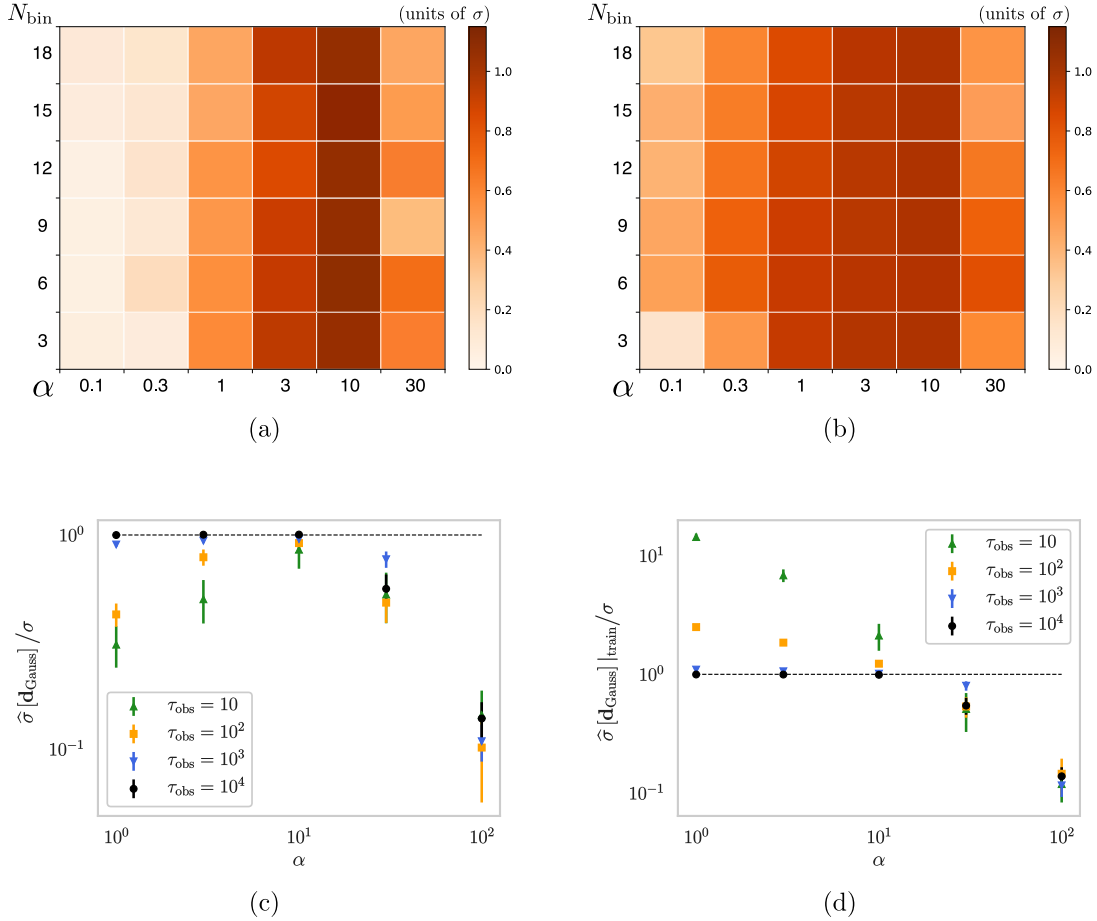

Figure 5.10: Hyperparameter dependence of the Gaussian learning estimator for the two-beads model ($r = 0.1$ with the same system parameters as in Fig. 5.4). (a)(b) $N_{\rm bin}$ and α dependence for (a) $\tau_{\rm obs} = 100$ and (b) $\tau_{\rm obs} = 1000$. (c) α dependence of the normalized test value $\widehat{\sigma}[\boldsymbol{d}^*_{\rm Gauss}]/\sigma$ for $\tau_{\rm obs} = 10$ to 10^4 with $N_{\rm bin} = 6$. (d) α dependence of the normalized training value $\widehat{\sigma}[\boldsymbol{d}_{\rm Gauss}]|_{\rm train}/\sigma$ for $\tau_{\rm obs} = 10$ to 10^4 with $N_{\rm bin} = 6$. The hyperparameter dependence is in accordance with Fig. 5.2. Note that the peak of the training curve is used for (d), but the similar results can be obtained even if $\boldsymbol{d}^*$, which is the optimal model function that maximizes the test curve, is used. In (c) and (d), the mean and its standard deviation of 10 independent trials are plotted. Reprinted figure with permission from Ref. [100] (DOI: 10.1103/PhysRevE.101.062106). Copyright 2020 by the American Physical Society.

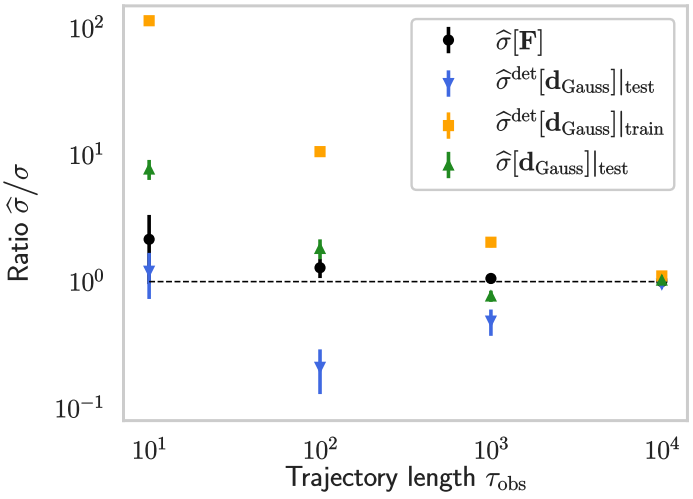

Figure 5.11: Bias of the short-time TUR for the two-beads model ($r = 0.5$ with the same system parameters as in Fig. 5.4). We plot the convergence rate of the short-time TUR with the optimal coefficient $\widehat{\sigma}[\boldsymbol{F}]$ (black circles), the Gaussian learning estimator $\widehat{\sigma}[\boldsymbol{d}_{\mathrm{Gauss}}]|_{\mathrm{test}}$ (green triangles), and the test and the training values of the Gaussian deterministic estimator $\widehat{\sigma}^{\mathrm{det}}[\boldsymbol{d}_{\mathrm{Gauss}}]|_{\mathrm{test}}$ (blue triangles), $\widehat{\sigma}^{\mathrm{det}}[\boldsymbol{d}_{\mathrm{Gauss}}]|_{\mathrm{train}}$ (orange squares). The mean and its standard deviation of 10 independent trials are plotted.

example, if the system is close to equilibrium, i.e., σ is small, we should use a larger time interval τ for the generalized current.

Second, the test value can actually adapt to the fluctuation of the test data because of the fluctuation of the gradient ascent. When the trajectory length is small, the learning curve becomes very noisy. Since we pick up the peak of the test curve, the model function can adapt to the test data by coincidence. Indeed, for the Gaussian deterministic estimator, all of the test values are placed below the optimal value $\widehat{\sigma}[\boldsymbol{F}]$ in Fig. 5.11, since there is no chance for the model function to adapt to the fluctuation of the test data in this estimator. On the other hand, for the Gaussian learning estimator, some of the test values come above the entropy production rate when the trajectory length is small.

Third, the correlation between the training and the test data becomes non-negligible when the trajectory length is small. For example, in Fig. 5.11, $\widehat{\sigma}^{\mathrm{det}}[\boldsymbol{d}_{\mathrm{Gauss}}]|_{\mathrm{test}}$ takes an unnaturally large value for $\tau_{\mathrm{obs}} = 10$, which cannot be explained by (i) and (ii). We consider that this is caused by the correlation between the training and the test data in term of their positions. The effect of the correlation can be confirmed, for example, by using $\{(\boldsymbol{x}_0, \boldsymbol{x}_{\Delta t}), (\boldsymbol{x}_{2\Delta t}, \boldsymbol{x}_{3\Delta t}), ...\}$ for the training data and $\{(\boldsymbol{x}_{\Delta t}, \boldsymbol{x}_{2\Delta t}), (\boldsymbol{x}_{3\Delta t}, \boldsymbol{x}_{4\Delta t}), ...\}$ for the test data, where available transitions are described by the parentheses. With this data splitting, we can check that the test value always comes above the entropy production rate due to the correlation.

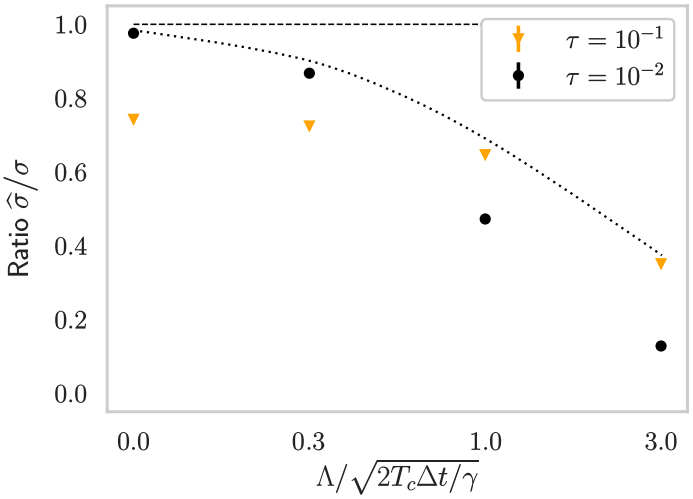

Figure 5.12: Effect of the measurement noise for the two-beads model ($r = 0.1, \tau_{\rm obs} = 10^4$, and $\Delta t = 10^{-2}$ with the other system parameters the same as in Fig. 5.4). The horizontal axis is the strength of the measurement noise Λ compared to the thermal noise of the cold bead $\sqrt{2T_c\Delta t/\gamma}$. The estimates of the Gaussian learning estimator with the time interval $\tau = 10^{-1}$ (yellow triangles), and $\tau = 10^{-2}$ (black circles) are plotted. Here, the generalized current with length $\tau = 10^{-1}$ is calculated using a pair $\{\boldsymbol{x}_{i\Delta t}, \boldsymbol{x}_{(i+10)\Delta t}\}$. Since we have the criterion that the higher is the better as an estimate, the dotted line would be the estimates we can get by tuning the time interval τ. The mean and its standard deviation of 10 independent trials are plotted.

5.5.3 Effect of measurement noise

Here, we study the effect of a measurement noise on the estimation. We simulate a measurement noise by adding a white noise to the data as

$$\boldsymbol{y}_{i\Delta t} = \boldsymbol{x}_{i\Delta t} + \sqrt{\Lambda}\boldsymbol{\eta}^i, \tag{5.63}$$

where Λ is the strength of the measurement noise, and $\boldsymbol{\eta}^i$ satisfies $\left\langle \eta_a^i \eta_b^j \right\rangle = \delta_{a,b}\delta_{i,j}$. We estimate the entropy production rate solely on the basis of the observed trajectory $\{\boldsymbol{y}_0, \boldsymbol{y}_{\Delta t}, ..., \boldsymbol{y}_{N\Delta t}\}$.

In Fig. 5.12, we study its effect using the two-beads model. Here, the strength Λ is determined compared to the thermal noise for the cold bead $\sqrt{2T_c\Delta t/\gamma}$. We find that the estimates take smaller values than the actual entropy production rate due to the measurement noise, while its effect can be mitigated by using a larger time interval for the generalized current. In Fig. 5.12, the estimates of the Gaussian learning estimator with the time interval $\tau = \Delta t$ and $\tau = 10\Delta t$ are plotted. When the measurement noise is small, the estimate is better with $\tau = \Delta t$, since the TUR cannot be regarded as the short-time TUR with the time interval $\tau = 10\Delta t$ in this setup. On the other hand, when the measurement noise is large, the estimate is better with $\tau = 10\Delta t$, which suggests that the finite-time

Model	τ_{obs}	Algorithm	N_{bin}	α	λ	N_{step}
Two-beads ($r = 0.1$)	$10 - 10^4$	$\widehat{\sigma}[\boldsymbol{d}_{\mathrm{Gauss}}]$	6	10		100
	10^4	$\widehat{\sigma}^{\lambda}[\boldsymbol{d}_{\mathrm{bin}}]$	20	1	10^{-4}	300
	10^3	$\widehat{\sigma}^{\lambda}[\boldsymbol{d}_{\mathrm{bin}}]$	12	1	10^{-2}	300
	10^2	$\widehat{\sigma}^{\lambda}[\boldsymbol{d}_{\mathrm{bin}}]$	8	1	10^{-1}	300
	10	$\widehat{\sigma}^{\lambda}[\boldsymbol{d}_{\mathrm{bin}}]$	8	1	10^{2}	300
Two-beads ($r = 0.5$)	$10 - 10^4$	$\widehat{\sigma}[\boldsymbol{d}_{\mathrm{Gauss}}]$	6	10		100
Five-beads ($r = 0.1$)	$10 - 10^4$	$\widehat{\sigma}[\boldsymbol{d}_{\mathrm{Gauss,m}}]$		1		100
	10^4	$\widehat{\sigma}^{\lambda}[\boldsymbol{d}_{\mathrm{bin}}]$	2	1	10^{-5}	300
	10^3	$\widehat{\sigma}^{\lambda}[\boldsymbol{d}_{\mathrm{bin}}]$	2	1	10^{-2}	300
	10^2	$\widehat{\sigma}^{\lambda}[\boldsymbol{d}_{\mathrm{bin}}]$	2	1	10^{-1}	300
	10	$\widehat{\sigma}^{\lambda}[\boldsymbol{d}_{\mathrm{bin}}]$	2	1	1	300
Five-beads ($r = 0.5$)	10^4	$\widehat{\sigma}^{\lambda}[\boldsymbol{d}_{\mathrm{bin}}]$	2	1	10^{-3}	300
	10^3	$\widehat{\sigma}^{\lambda}[\boldsymbol{d}_{\mathrm{bin}}]$	2	1	10^{-2}	300
	10^2	$\widehat{\sigma}^{\lambda}[\boldsymbol{d}_{\mathrm{bin}}]$	2	1	10^{-1}	300
	10	$\widehat{\sigma}^{\lambda}[\boldsymbol{d}_{\mathrm{bin}}]$	2	1	10	300
10, 15-beads ($r = 0.1$)	$10 - 10^4$	$\widehat{\sigma}[\boldsymbol{d}_{\mathrm{Gauss,m}}]$		1		100
Mexican-hat ($A = 10^{-4}$)	$10 - 10^4$	$\widehat{\sigma}[\boldsymbol{d}_{\mathrm{Gauss}}]$	6	10		100
Mexican-hat ($A = 1$)	$10 - 10^4$	$\widehat{\sigma}[\boldsymbol{d}_{\mathrm{Gauss}}]$	6	1		100
Mexican-hat ($A = 10^2$)	$10 - 10^4$	$\widehat{\sigma}[\boldsymbol{d}_{\mathrm{Gauss}}]$	6	0.3		100
One-dimensional hopping		$\widehat{\sigma}^{\mathrm{M}}[d]$		0.01		300

Table 5.1: Hyperparameters used for the learning estimators in this study. N_{step} is the iteration number of the gradient ascent.

TUR is robust against the measurement noise. Since we have the criterion that the higher is the better as an estimate, we can get the best estimate which is illustrated as a dotted line in Fig. 5.12 by tuning the time interval in practice.

Chapter 6

Estimating entropy production along non-stationary trajectories

In this chapter, we extend the learning algorithm developed in Chap. 5 to non-stationary dynamics. In Sec. 6.1, we give a short introduction to this study. In Sec. 6.2, we establish the theoretical relationship between two variational representations of the entropy production, one is the short-time TUR and the other is the NEEP, in terms of the range of applicability, the optimal coefficient field, and the tightness of the bound in non-stationary dynamics. On the basis of this result, we propose an efficient estimation method that estimates the thermodynamic force continuously in time in Sec. 6.3. Specifically, we adopt feedforward neural networks for the model function in this chapter. In Sec. 6.4, we numerically demonstrate the working of our method using time-dependent Langevin models. We show that the continuous-time estimation is data efficient since the estimate converges not only by increasing the number of trajectories but also by increasing the number of time instances contained in each trajectory. In this chapter, we mainly consider non-stationary Langevin dynamics, while our method is straightforwardly extendable to Markov jump processes. The results presented in this chapter are based on our paper [104].

6.1 Introduction

In biological systems, non-stationary dynamics ubiquitously appear as, for example, adaptive responses to environmental change [105, 106] or spontaneous oscillations [107–109]. However, in contrast to the stationary case, the estimation of the entropy production in non-stationary dynamics is largely unexplored. This is because the non-stationary estimation requires repeating of the same experiments many times, which can be a significant hurdle in practice. On the other hand, it has been recently proposed to use a modified TUR for the non-stationary estimation [110]. The proposed method, however, gives only a lower estimate of the entropy production and requires perturbations to dynamics. Thus, it is desirable to establish an estimation method that can give an exact estimate solely on the basis of a small number of trajectories.

In the previous chapter, we have developed a variational estimation method for the stationary entropy production. This method can actually be applied to non-stationary

Rep.	Markov jump	Langevin	Optimal field	Tightness
σ_{NEEP}	Yes	Yes	$\boldsymbol{d}^*(\boldsymbol{x}) = \boldsymbol{F}(\boldsymbol{x}, t)$	Loose
σ_{Simple}	No	Yes	$\boldsymbol{d}^*(\boldsymbol{x}) = \boldsymbol{F}(\boldsymbol{x}, t)$	Loose
σ_{TUR}	No	Yes	$\boldsymbol{d}^*(\boldsymbol{x}) \propto \boldsymbol{F}(\boldsymbol{x}, t)$	Tight

Table 6.1: Summary of the comparison among the variational representations σ_{NEEP}, σ_{Simple} and σ_{TUR}.

dynamics straightforwardly. This is because if we look at only an ensemble of jumps that occur at a particular time t to estimate the instantaneous thermodynamic force $\boldsymbol{F}(\boldsymbol{x})$, the same estimation method as the stationary case can be applied. Let us call this approach instantaneous-time estimation. However, this approach discards a lot of information that the whole trajectories have, since it ignores the jumps that occur at times near to t, while the thermodynamic force should be close to each other when their times are close. Thus, there is room for improvement of the non-stationary estimation method beyond the instantaneous-time estimation.

On another front, a variational representation of the entropy production other than the short-time TUR has been recently proposed, which is called Neural Estimator for Entropy Production (NEEP) [111]. In contrast to the short-time TUR, the NEEP gives an exact estimate in both Markov jump processes and overdamped Langevin dynamics. However, the relationship between the short-time TUR and the NEEP has not been revealed yet.

In this chapter, we resolve these issues. First, we establish the theoretical relationship between the short-time TUR and the NEEP. Then, we propose a continuous-time estimation method that learns the whole trajectories at once and estimates the thermodynamic force continuously in time, i.e., $\boldsymbol{F}(\boldsymbol{x}, t)$. Our method can estimate the entropy production along single trajectories and the entropy production rate using the obtained thermodynamic force (see Fig. 6.1). We find that the continuous-time estimation indeed converges better than the instantaneous-time estimation, which shows the effectiveness of our variational approach for non-stationary dynamics as well as nonlinear and high-dimensional dynamics.

6.2 Short-time variational representations of the entropy production

Here, we establish the theoretical relationship between the short-time TUR and the NEEP by deriving an intermediate variational representation of them called the simple dual representation. In addition, we show that the NEEP is related to a dual representation of the Kullback-Leibler divergence [112–114] and it is applicable to non-stationary dynamics, complementing the original result for stationary dynamics [111]. The summary of the comparison is presented in Table 6.1.

First, we introduce the short-time TUR representation, which has been formulated in

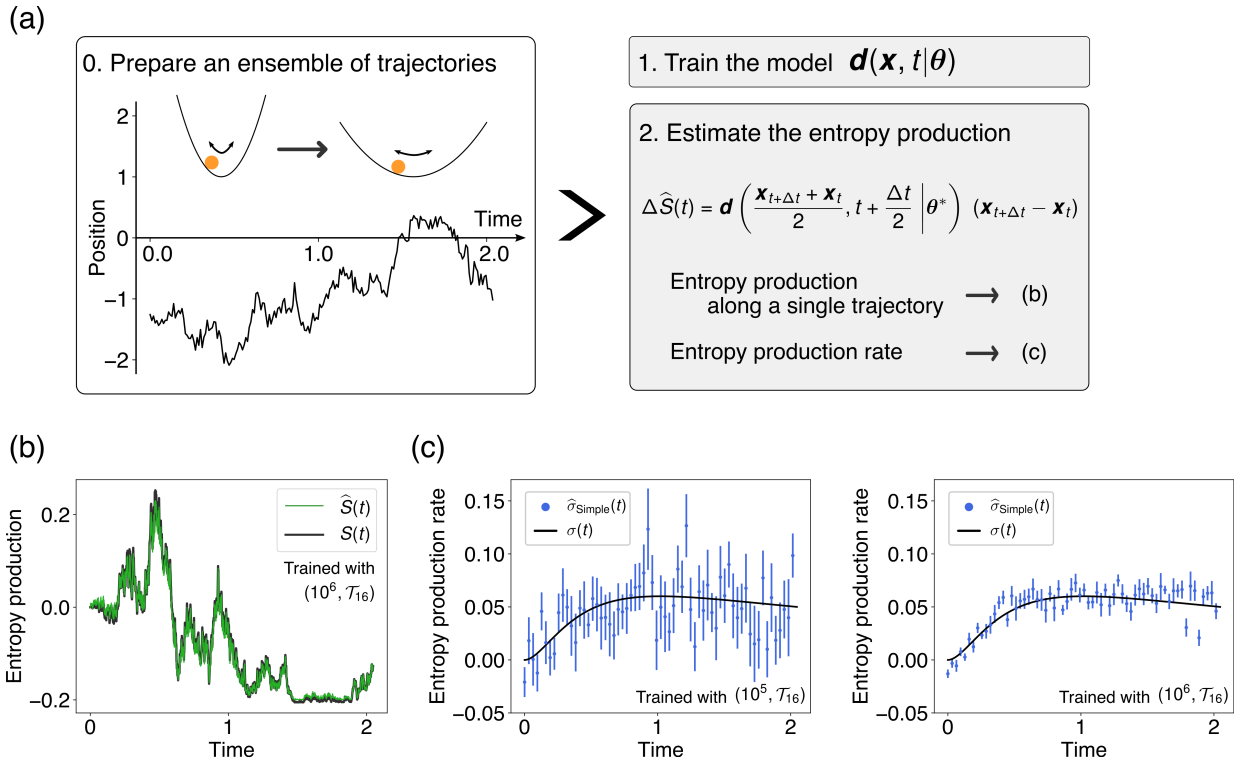

Figure 6.1: Estimating the entropy production along single trajectories. (a) Schematic of our estimation scheme. Our method is solely based on an ensemble of trajectories which are sampled from repeated experiments. We optimize the model function in terms of the parameters $\boldsymbol{\theta}$ to get an estimate of the thermodynamic force $\boldsymbol{d}(\boldsymbol{x}, t|\boldsymbol{\theta}^*)$, and use it to estimate the entropy production along a single trajectory or the entropy production rate. We show an example of a trajectory sampled from the breathing parabola model in the left box. (b) Estimated entropy production along a single trajectory. The thin green line is the estimated entropy production, and the thick black line is the true entropy production. The estimation is conducted for the trajectory drawn in (a) after training the model function using an ensemble of single transitions at $\mathcal{T}_{16}$ of 10^6 trajectories (see Sec. 6.3.1 for the definition of $\mathcal{T}_k$). (c) Estimated entropy production rate. The blue circles are the estimated values using 10^5 (left) and 10^6 (right) trajectories with $\mathcal{T}_{16}$, and the black line is the true entropy production rate. The mean and its standard deviation of 10 independent trials are plotted for the estimated values. For (a)-(c), trajectories are sampled from the breathing parabola model with system parameters $\gamma = T = 1, \Delta t = 10^{-3}$ and $\tau_{\mathrm{obs}} = 2.048$, and the simple dual representation (Eq. (6.3)) is used for both the training and the evaluation.

the previous chapter. In this chapter, we describe this representation as σ_{TUR} defined by

$$\sigma_{\mathrm{TUR}}(t) := \frac{1}{\mathrm{d}t} \max_{\boldsymbol{d}} \frac{2\left\langle J_{\boldsymbol{d}} \right\rangle^2}{\mathrm{Var}(J_{\boldsymbol{d}})}, \tag{6.1}$$

where $J_{\boldsymbol{d}} = \boldsymbol{d}(\boldsymbol{x}) \circ \mathrm{d}\boldsymbol{x}(t)$ is the (single-step) generalized current with some coefficient field $\boldsymbol{d}(\boldsymbol{x})$. The short-time TUR gives an exact estimate of the entropy production rate in overdamped Langevin dynamics, while it gives only a lower estimate in Markov jump processes. The optimal coefficient is proportional to the thermodynamic force $\boldsymbol{d}(\boldsymbol{x}) = c\boldsymbol{F}(\boldsymbol{x}, t)$, and its constant factor c can be calculated by $c = \mathrm{Var}(J_{\boldsymbol{d}})/2\left\langle J_{\boldsymbol{d}} \right\rangle$ as shown in Eq. (5.24).

Next, we introduce the NEEP representation [111]. We formulate the NEEP in the form of a variational representation of the entropy production rate:

$$\sigma_{\mathrm{NEEP}}(t) := \frac{1}{\mathrm{d}t} \max_{\boldsymbol{d}} \left\langle J_{\boldsymbol{d}} - e^{-J_{\boldsymbol{d}}} + 1 \right\rangle, \tag{6.2}$$

which is a slight modification from the original expression in Ref. [111]. In contrast to the short-time TUR, the NEEP gives an exact estimate for both Markov jump processes and overdamped Langevin dynamics, and the optimal coefficient directly gives the thermodynamic force $\boldsymbol{d}^*(\boldsymbol{x}) = \boldsymbol{F}(\boldsymbol{x})$. In the end of this section, we show that the NEEP is also applicable to non-stationary dynamics, although it was derived for stationary dynamics in Ref. [111].

Then, we reveal the pros and cons of the short-time TUR and the NEEP. For the comparison, we derive another variational representation named the simple dual representation σ_{Simple} from σ_{NEEP} by assuming Langevin dynamics and by expanding $\left\langle e^{-J_{\boldsymbol{d}}} \right\rangle$ as

$$\sigma_{\mathrm{Simple}}(t) := \frac{1}{\mathrm{d}t} \max_{\boldsymbol{d}} \left[2\left\langle J_{\boldsymbol{d}} \right\rangle - \frac{\mathrm{Var}(J_{\boldsymbol{d}})}{2} \right], \tag{6.3}$$

where we used $\left\langle e^{-J_{\boldsymbol{d}}} \right\rangle = 1 - \left\langle J_{\boldsymbol{d}} \right\rangle + \mathrm{Var}(J_{\boldsymbol{d}})/2 + o(\mathrm{d}t)$. Since Langevin dynamics is assumed for the expansion of $\left\langle e^{-J_{\boldsymbol{d}}} \right\rangle$, the simple dual representation gives an exact estimate only in Langevin dynamics. Note that we do not assume anything on the probability distribution for the expansion, and it always holds for general Langevin dynamics. Interestingly, the simple dual representation consists of only the mean and the variance of the generalized current similarly to the short-time TUR.

The simple dual representation reveals the relation between the short-time TUR and the NEEP in terms of the tightness of the bounds in Langevin dynamics. Concretely, the following inequality holds for any fixed choice of $J_{\boldsymbol{d}}$:

$$\sigma \mathrm{d}t \geq \frac{2\left\langle J_{\boldsymbol{d}} \right\rangle^2}{\mathrm{Var}(J_{\boldsymbol{d}})} \geq 2\left\langle J_{\boldsymbol{d}} \right\rangle - \frac{\mathrm{Var}(J_{\boldsymbol{d}})}{2}, \tag{6.4}$$

where we used the inequality $\frac{2a^2}{b} \geq 2a - \frac{b}{2}$ for any a and $b > 0$. Since a tighter bound is advantageous for the estimation [114,115], the short-time TUR would be more effective for the estimation of the entropy production rate. Note that the NEEP and the simple dual representation have slightly different statistical properties when they are estimated with

data, and thus the relation (6.4) does not hold in a strict sense between the NEEP and the short-time TUR in practice. However, we numerically find that the short-time TUR indeed converges the fastest, while the NEEP and the simple dual representation show similar convergence (see Sec. 6.6.1).

On the other hand, the NEEP and the simple dual representation would be more effective for the estimation of the thermodynamic force. This is because the optimal coefficient directly gives the thermodynamic force in the NEEP and the simple dual representation, while the short-time TUR necessitates the correction of the constant factor. In the next section, we introduce the continuous-time estimation that improves the estimate of the thermodynamic force using the whole trajectories. The correction of the constant factor can negate the benefit of the continuous-time estimation by adding relatively large statistical error, since it is calculated by using an ensemble of jumps at a single time t as $c(t) = \mathrm{Var}(J_{\boldsymbol{d}})/2\langle J_{\boldsymbol{d}}\rangle$. Here, the time dependence is explicitly written for $c(t)$ to emphasize that it can be different from time to time (see Sec. 6.6.1 for a numerical experiment). In Table 6.1, we summarize the above discussion.

Finally, we show that the NEEP is mathematically related to a dual representation of the Kullback-Leibler (KL) divergence [112–114], and it is applicable to non-stationary dynamics. We consider probability distributions $P(x)$ and $Q(x)$ over a discrete state space Ω. The KL divergence between P and Q is defined by

$$D_{\mathrm{KL}}(P||Q) := \sum_{x\in\Omega} P(x)\ln\frac{P(x)}{Q(x)}. \tag{6.5}$$

The KL divergence can be expressed in a variational form:

$$D_{\mathrm{KL}}(P||Q) = \max_{h\in\mathcal{F}} \mathbb{E}_P[h+1] - \mathbb{E}_Q[e^h], \tag{6.6}$$

where $\mathcal{F}$ is a set of functions $h : \Omega \to \mathbb{R}$ such that the two expectations $\mathbb{E}_P[h+1]$ and $\mathbb{E}_Q[e^h]$ are finite, and the optimal function is given by $h^* = \ln\frac{P(x)}{Q(x)}$. This representation is derived using the Fenchel convex duality [112–114], and called a dual representation of the KL divergence.

We derive the NEEP by assuming Markov jump processes. The entropy production rate can be written as the KL divergence [6]

$$\sigma(t) = D_{\mathrm{KL}}(p_t(x)r_t(x,x')||p_t(x')r_t(x',x)), \tag{6.7}$$

where $p_t(x)$ is the probability distribution, and $r_t(x,x')$ is the transition rate from x to x' at time t. Then, we get the NEEP by applying Eq. (6.6) as

$$\sigma(t) = \frac{1}{\mathrm{d}t}\max_{h\in\mathcal{F}'}\left\langle h - e^{-h} + 1\right\rangle, \tag{6.8}$$

where $\mathcal{F}'$ is a set of functions $h : \Omega\times\Omega \to \mathbb{R}$ which make the above expectation finite and satisfy $h(x,x') = -h(x',x)$. Here, the expectation is taken as

$$\langle f(x,x')\rangle := \mathrm{d}t\sum_{x,x'} p_t(x)r_t(x,x')f(x,x'), \tag{6.9}$$

and the optimal function is the entropy production $h^* = \ln \frac{p_t(x)r_t(x,x')}{p_t(x')r_t(x',x)}$. We can further derive Eq. (6.2) from Eq. (6.8) by using the fact that h^* can be written as the generalized current, and thus the generalized current can be adopted as the function h. Importantly, the NEEP holds for non-stationary dynamics since the stationarity is not assumed in Eq. (6.7). The derivation of Eq. (6.8) is as follows:

$$\begin{aligned}
\sigma &= D_{\mathrm{KL}}(p_t(x)r_t(x,x')||p_t(x')r_t(x',x)) && \text{(6.10a)}\\
&= \max_{h\in\mathcal{F}}\left[\sum_{x,x'} p_t(x)r_t(x,x')h(x,x') - \sum_{x,x'} p_t(x')r_t(x',x)e^{h(x,x')} + 1\right] && \text{(6.10b)}\\
&= \max_{h\in\mathcal{F}'}\left[\sum_{x,x'} p_t(x)r_t(x,x')h(x,x') - \sum_{x,x'} p_t(x')r_t(x',x)e^{h(x,x')} + 1\right] && \text{(6.10c)}\\
&= \max_{h\in\mathcal{F}'}\left[\sum_{x,x'} p_t(x)r_t(x,x')\left\{h(x,x') - e^{-h(x,x')} + 1\right\}\right] && \text{(6.10d)}\\
&= \frac{1}{\mathrm{d}t}\max_{h\in\mathcal{F}'}\left\langle h - e^{-h} + 1\right\rangle, && \text{(6.10e)}
\end{aligned}$$

where we used Eq. (6.6) in Eq. (6.10b), and added a new constraint $h(x',x) = -h(x,x')$ in Eq. (6.10c) using the fact that h^* satisfies the constraint. Note that we derived the NEEP by assuming Markov jump processes here, but it means that the NEEP also holds in overdamped Langevin dynamics through the jump process approximation (Eq. (3.15)).

6.3 Estimation method for non-stationary dynamics

In this section, we propose the continuous-time estimation scheme for non-stationary dynamics, which estimates the thermodynamic force continuously in time. In Sec. 6.3.1, we explain the main idea. In Sec. 6.3.2, we explain the implementation details of our method using feedforward neural networks.

6.3.1 General idea

A schematic of our estimation method is presented in Fig. 6.1. Our method is solely based on an ensemble of trajectories sampled from a non-stationary dynamics with sampling interval Δt:

$$\Gamma_i = \{\boldsymbol{x}_0, \boldsymbol{x}_{\Delta t}, ..., \boldsymbol{x}_{\tau_{\mathrm{obs}}}(=\boldsymbol{x}_{M\Delta t})\}_i \ \ (i = 1, ..., N), \tag{6.11}$$

where i is the index of trajectories, τ_{obs} is the observation time, M is the number of transitions, and N is the number of trajectories.

We can estimate the entropy production rate $\sigma(t)$ using only an ensemble of single transitions at time t: $\{\boldsymbol{x}_t, \boldsymbol{x}_{t+\Delta t}\}_i$ $(i = 1, ..., N)$ in the same manner as in Chap. 5. Concretely, we optimize a model function $\boldsymbol{d}(\boldsymbol{x}|\boldsymbol{\theta})$ with respect to the objective function $\widehat{\sigma}(t)|_{\mathrm{train}}$ calculated with only a half of the ensemble $\{\boldsymbol{x}_t, \boldsymbol{x}_{t+\Delta t}\}_i$ $(i = 1, ..., N/2)$. Here, $\widehat{\sigma}(t)$ denotes any

of $\widehat{\sigma}_{\rm TUR}(t), \widehat{\sigma}_{\rm NEEP}(t)$, and $\widehat{\sigma}_{\rm Simple}(t)$, and we use the hat symbol for estimated quantities. Then, we evaluate the trained model function $\boldsymbol{d}(\boldsymbol{x}|\boldsymbol{\theta})$ with the objective function $\widehat{\sigma}(t)|_{\rm test}$ calculated with the other half $\{\boldsymbol{x}_t, \boldsymbol{x}_{t+\Delta t}\}_i$ $(i = N/2+1, ..., N)$. Let us call this approach the instantaneous-time estimation.

However, as we have discussed in Sec. 6.1, the instantaneous-time estimation is not data efficient, since it discards information contained in the other single transitions. To overcome this problem, we consider to optimize a time-dependent model function $\boldsymbol{d}(\boldsymbol{x}, t|\boldsymbol{\theta})$ using the whole trajectories at once. Concretely, we construct an objective function as follows:

$$\widehat{f_{\mathcal{T}_k}}(\boldsymbol{\theta}) := \sum_{t\in\mathcal{T}_k} a(t)\widehat{\sigma}(t) \Big/ \sum_{t\in\mathcal{T}_k} a(t), \tag{6.12}$$

where $\mathcal{T}_k$ is a set of time instances, and $a(t)$ is any positive value defined for $t \in \mathcal{T}_k$ (see Sec. 6.3.2 for the details of $a(t)$). Here, a set of time instances is defined as $\mathcal{T}_k := \{0, k\Delta t, 2k\Delta t, ..., lk\Delta t\}$, where l is the maximum integer satisfying $lk+1 \leq M$. Similarly to the instantaneous-time estimation, we optimize the model function $\boldsymbol{d}(\boldsymbol{x}, t|\boldsymbol{\theta})$ with respect to the objective function $f_{\mathcal{T}_k}(\boldsymbol{\theta})|_{\rm train}$ calculated with a half of the ensemble Γ_i $(i = 1, ..., N/2)$, and evaluate it with $f_{\mathcal{T}_k}(\boldsymbol{\theta})|_{\rm test}$ calculated with the other half Γ_i $(i = N/2+1, ..., N)$. Here, $\widehat{\sigma}(t)$ is calculated by viewing

$$J_{\boldsymbol{d}} = \boldsymbol{d}\left(\frac{\boldsymbol{x}_t + \boldsymbol{x}_{t+\Delta t}}{2}, t + \frac{\Delta t}{2}\,\middle|\,\boldsymbol{\theta}\right)[\boldsymbol{x}_{t+\Delta t} - \boldsymbol{x}_t] \tag{6.13}$$

as a realization of the generalized current. Specifically, we perform the gradient ascent for $f_{\mathcal{T}_k}(\boldsymbol{\theta})|_{\rm train}$, and find the optimal parameters $\boldsymbol{\theta}^*$ which maximize $f_{\mathcal{T}_k}(\boldsymbol{\theta})|_{\rm test}$. Then, $\boldsymbol{d}(\boldsymbol{x}, t|\boldsymbol{\theta}^*)$ is expected to converge to the thermodynamic force $\boldsymbol{F}(\boldsymbol{x}, t)$ at least at $t \in \mathcal{T}_k$, and even at interpolating times if $k\Delta t$ is sufficiently small. Let us call this approach the continuous-time estimation.

We give some remarks on the set of time instances $\mathcal{T}_k$. First, we basically use an ensemble of single transitions $\{\{\boldsymbol{x}_0, \boldsymbol{x}_{\Delta t}\}_i, \{\boldsymbol{x}_{k\Delta t}, \boldsymbol{x}_{(k+1)\Delta t}\}_i, ..., \{\boldsymbol{x}_{lk\Delta t}, \boldsymbol{x}_{(lk+1)\Delta t}\}_i\}$ for both the training and the evaluation during the gradient ascent when $\mathcal{T}_k$ is adopted. Although $\mathcal{T}_k$ with $k \geq 2$ is not a natural data set, we introduce this notation (i) to study the convergence of the estimate as we increase the number of time instances (i.e., as we decrease k) contained in each trajectory, and (ii) to decrease the computational cost. Second, we sometimes use $\{\boldsymbol{x}_t, \boldsymbol{x}_{t+\tau}\}_i$ with $\tau = m\Delta t$ $(m \geq 2)$ to calculate $\widehat{\sigma}(t)$, i.e., use an ensemble of single transitions $\{\{\boldsymbol{x}_0, \boldsymbol{x}_\tau\}_i, \{\boldsymbol{x}_{k\Delta t}, \boldsymbol{x}_{k\Delta t+\tau}\}_i, ...\}$ for $\mathcal{T}_k$. This is because a smaller time interval does not necessarily lead to a better estimate as we have seen in Chap. 5.

6.3.2 Implementation with neural networks

Here, we explain the implementation details.

Basic algorithm

We adopt feedforward neural networks for the model function $\boldsymbol{d}(\boldsymbol{x}, t|\boldsymbol{\theta})$ to learn the thermodynamic force $\boldsymbol{F}(\boldsymbol{x}, t)$. This is because a neural network is suitable for expressing a

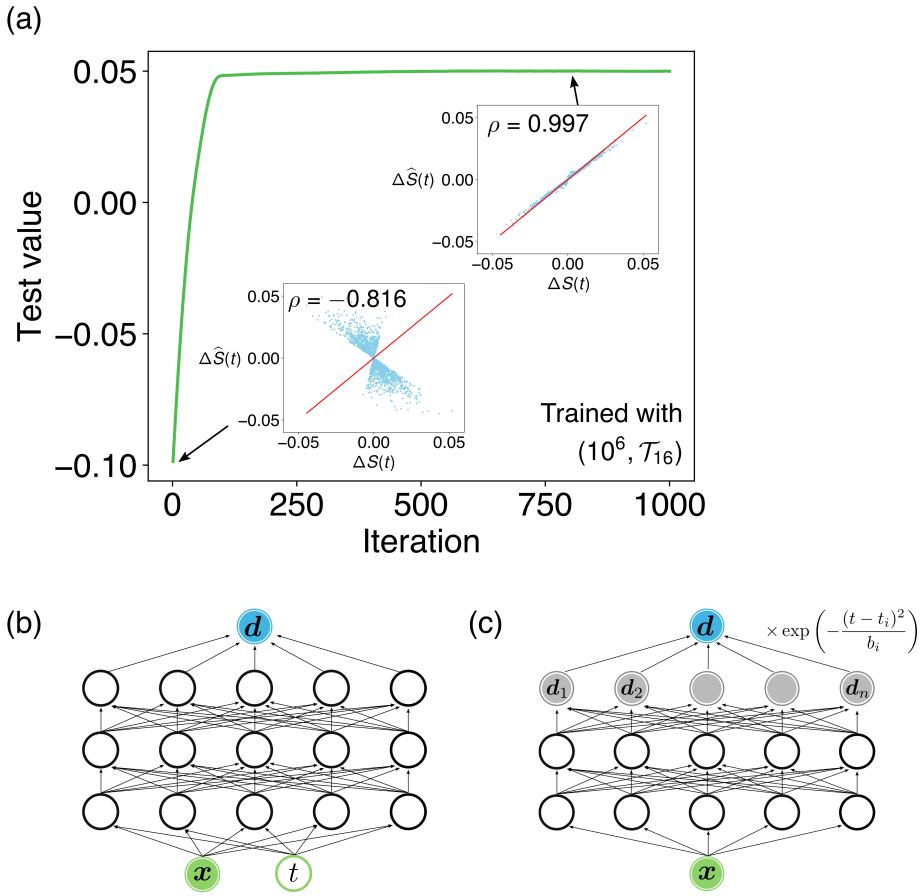

Figure 6.2: Training of the neural network. (a) An example of the learning curve of the test value for trajectories generated by the breathing parabola model. As the inset plots, we show scatter plots between the true (Eq. (6.21)) and the estimated (Eq. 6.20) single-step entropy production along a single trajectory, and ρ is the correlation between them evaluated along 100 trajectories. As the gradient ascent proceeds, the estimate becomes more accurate. The same system parameters as in Fig. 6.1 are used for the breathing parabola model. (b) Sketch of the feedforward neural network. We adopt a five-layer network with three hidden layers. (c) Sketch of the modified neural network. We adopt a four-layer network with two hidden layers, where the gray and the blue units are regarded as a single output layer. We basically use the normal neural network depicted in (b) unless explicitly stated otherwise.

nontrivial functional form of the thermodynamic force with time dependence [111, 116], and it is known to perform well for interpolation of discrete data [117], which is essential for the continuous-time estimation. Concretely, we mainly use a five-layer network depicted in Fig. 6.2(b). The network inputs $\boldsymbol{x}$ and t, and outputs the coefficient field $\boldsymbol{d}$. The ith layer is fully-connected to the $(i+1)$th layer, and the rectified linear function (ReLU) is adopted as the activation function for the hidden layers (i = 2, 3, 4). The hyperparameters of the neural network are the number of hidden layers $N_{\rm layer}$ and the number of units in each hidden layer $N_{\rm hidden}$, which are predetermined similarly to the previous chapter (see Sec. 6.6.2 for the details).

We update the parameters of the neural network $\boldsymbol{\theta}$ by the gradient ascent:

$$\boldsymbol{\theta} \to \boldsymbol{\theta} + \alpha \nabla_{\boldsymbol{\theta}} \widehat{f_{\mathcal{T}_k}}|_{\rm train}, \tag{6.14}$$

and evaluate the model function with $\widehat{f_{\mathcal{T}_k}}|_{\rm test}$. Here, we set $a(t)$ uniformly randomly from $0 < x \leq 1$ for $\widehat{f_{\mathcal{T}_k}}|_{\rm train}$ in every iteration to introduce stochasticity, which can be regarded as the stochastic gradient ascent [118]. On the other hand, we set $a(t) = 1$ for $\widehat{f_{\mathcal{T}_k}}|_{\rm test}$ to evaluate the model function with equal weight on $\widehat{\sigma}(t)$. $\widehat{f_{\mathcal{T}_k}}|_{\rm test}$ is an estimate of the time-averaged entropy production rate $\sum_{t\in\mathcal{T}_k} \widehat{\sigma}(t)/\sum_{t\in\mathcal{T}_k} 1$, and we describe it as the test value. Specifically, we implement an algorithm called Adam [101] for the gradient ascent to improve the convergence.

In Fig. 6.2(a), we show an example of the learning curve of the test value. We adopt the parameters $\boldsymbol{\theta}^*$ at the peak of the learning curve for the estimation, and regard $\boldsymbol{d}(\boldsymbol{x}, t|\boldsymbol{\theta}^*)$ as an estimate of the thermodynamic force. Note that we multiple $\boldsymbol{d}(\boldsymbol{x}, t|\boldsymbol{\theta}^*)$ by $2\widehat{\langle J_{\boldsymbol{d}}\rangle}/\widehat{\rm Var(J_{\boldsymbol{d}})}$, which is calculated using an ensemble of jumps $\{\boldsymbol{x}_t, \boldsymbol{x}_{t+\Delta t}\}_i$ $(i = N/2+1, ..., N)$, if the short-time TUR is used.

Further improvement

In the next section, we basically use the above algorithm (for Figs. 6.1, 6.3, and 6.4), while we consider two improvements in Fig. 6.5 to demonstrate the effectiveness of our method in practice. Concretely, we consider to use $\mathrm{Var}(J_{\boldsymbol{d}})/2\mathrm{d}t$ as an estimator of the entropy production rate and use a modified neural network depicted in Fig. 6.2(c).

First, $\mathrm{Var}(J_{\boldsymbol{d}})/2\mathrm{d}t$ gives an estimate of the entropy production rate when the coefficient is the thermodynamic force $\boldsymbol{d} = \boldsymbol{F}$ as shown in Eq. (5.22). We find that $\mathrm{Var}(J_{\boldsymbol{d}})/2\mathrm{d}t$ can significantly reduce the statistical error compared to the objective functions of the variational representations. This is because the estimated quantity $\widehat{\rm Var(J_{\boldsymbol{d}})}$ has a smaller variance than $\widehat{\langle J_{\boldsymbol{d}}\rangle}$ as follows:

$$\mathrm{Var}\left[\widehat{\langle J_{\boldsymbol{d}}\rangle}\right] \propto \mathrm{d}t, \tag{6.15}$$

$$\mathrm{Var}\left[\widehat{\mathrm{Var}(J_{\boldsymbol{d}})}\right] \propto \mathrm{d}t^2, \tag{6.16}$$

which can be derived using the fact that $\mathrm{Var}(J_{\boldsymbol{d}}) \propto \mathrm{d}t$, $\mathrm{Var}(J_{\boldsymbol{d}}^2) \propto \mathrm{d}t^2$ (see Eq. (5.23)), and these quantities are estimated by $\widehat{\langle J_{\boldsymbol{d}}\rangle} = \sum_i J_{\boldsymbol{d}}/N$, $\widehat{\mathrm{Var}(J_{\boldsymbol{d}})} = \sum_i J_{\boldsymbol{d}}^2/N - (\sum_i J_{\boldsymbol{d}}/N)^2$.

The use of $\mathrm{Var}(J_{\boldsymbol{d}})/2\mathrm{d}t$ is effective only for the continuous-time estimation with the NEEP and the simple dual representation. This is because the variance of the objective function $\widehat{\sigma}(t)$, which consists of $\widehat{\langle J_{\boldsymbol{d}}\rangle}$ and $\widehat{\mathrm{Var}(J_{\boldsymbol{d}})}$, inevitably leads to the similar variance of the estimated thermodynamic force $\boldsymbol{d}(\boldsymbol{x}, t|\boldsymbol{\theta}^*)$ in the instantaneous-time estimation. For the short-time TUR, $\widehat{\mathrm{Var}(J_{\boldsymbol{d}})}/2\mathrm{d}t$ becomes equivalent to the objective function $2\widehat{\langle J_{\boldsymbol{d}}\rangle}^2/\widehat{\mathrm{Var}(J_{\boldsymbol{d}})}\mathrm{d}t$ itself, which can be derived by substituting the model function with the correction term $2\widehat{\langle J_{\boldsymbol{d}}\rangle}/\widehat{\mathrm{Var}(J_{\boldsymbol{d}})}$ into $\widehat{\mathrm{Var}(J_{\boldsymbol{d}})}/2\mathrm{d}t$.

Second, we numerically find that the modified neural network depicted in Fig. 6.2(c) converges better than the normal neural network. The difference from the normal network is that the time-dependence appears only in the output layer, and the output is given by

$$\boldsymbol{d} = \sum_{k=1}^{N_{\mathrm{output}}} \boldsymbol{d}_k \exp\left[-\left(\frac{t-t_k}{b}\right)^2\right], \tag{6.17}$$

where N_{output} is the number of units in the output layer, $t_k = \frac{k-1}{N-1}\tau_{\mathrm{obs}}$, and $b = \frac{\tau_{\mathrm{obs}}}{N_{\mathrm{output}}-1}$. The idea of this neural network is that the unit $\boldsymbol{d}_k$ learns the thermodynamic force around time t_k. The modified network performs better since it implicitly assumes that the local thermodynamic force changes at a similar speed for all the position $\boldsymbol{x}$, which is the case in our setups. In practice, we can decide which network to use by comparing their test values as presented in Fig. 6.5(a).

6.4 Numerical experiments

In this section, we numerically demonstrate our method using the following two linear Langevin models: (i) a one-dimensional breathing parabola model, and (ii) a two-dimensional adaptation model. In the both models, a number of trajectories are sampled by repeating the same simulations many times, and we estimate the entropy production solely on the basis of the sampled trajectories. First, we show that our method gives an exact estimate of the entropy production rate, the entropy production along a single trajectory, and the thermodynamic force by comparing the estimation results with the analytical solutions. Next, we show that our method is data efficient since the estimate converges not only by increasing the number of trajectories but also by increasing the number of time instances. Finally, we study the practical effectiveness of our method in various setups. In this section, we only use the simple dual representation for the training of the model function, while we compare the performance of the variational representations in Sec. 6.6.1.

6.4.1 Main results

We first consider the breathing parabola model [120,121] that describes a Brownian particle inside a harmonic potential $V(x,t) = \frac{\kappa(t)}{2}x^2$. The system is in equilibrium at $t = 0$ and follows a Gaussian distribution, and it is driven out of equilibrium by the change in the stiffness of the potential as $\kappa(t) = \frac{1}{1+t}$. Its dynamics is described by the following Langevin equation:

$$\gamma\dot{x}(t) = -\kappa(t)x(t) + \sqrt{2\gamma T}\,\eta(t), \tag{6.18}$$

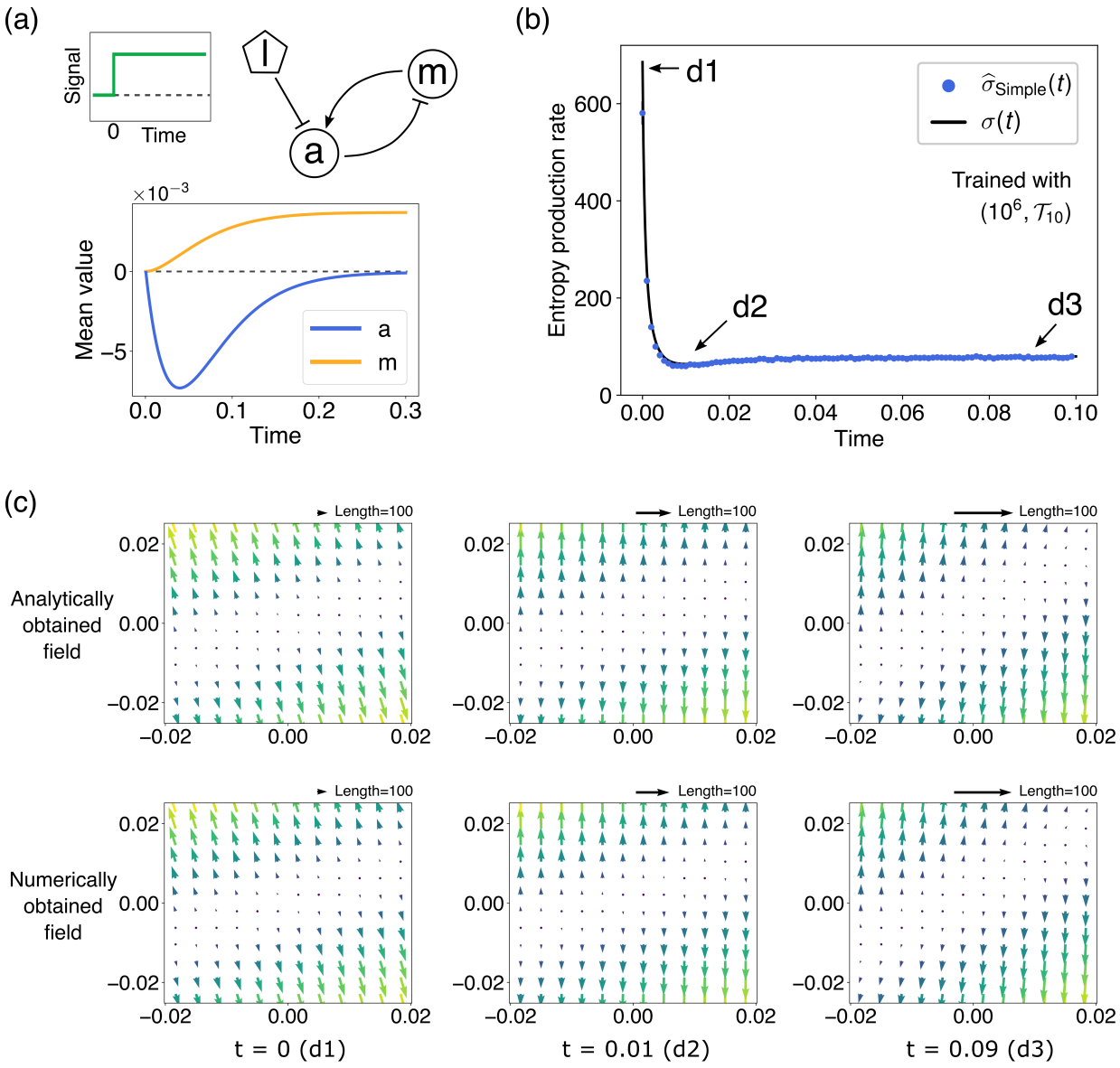

Figure 6.3: Estimation in the adaptation model. (a) Schematic of the model. The average dynamics of a and m after the inhibitory input by l are plotted. (b) Estimated entropy production rate. The blue circles are the estimated values using an ensemble of single transitions at $\mathcal{T}_{10}$ of 10^6 trajectories, and the black line is the true entropy production rate. The mean and its standard deviation of 10 independent trials are plotted. (c) Estimated thermodynamic force. The lower three figures are the estimated field at $t = 0, 0.01, 0.09$ by the model function trained with an ensemble of single transitions of size $(10^6, \mathcal{T}_{10})$, and the upper three figures are the corresponding analytical fields. The horizontal axis is the direction of a, and the vertical axis is that of m, and a reference vector with size 100 is shown at the top of each plot. For (a)-(c), the system parameters are set as $\tau_a = 0.02, \tau_m = 0.2, \alpha = 2.7, \beta = 1, \Delta_a = 0.005(t < 0), 0.5(t \geq 0), \Delta_m = 0.005, l(t) = 0(t < 0), 0.01(t \geq 0)$ which are taken from Refs. [105, 119] as realistic parameters of *E. coli* chemotaxis. The trajectories are sampled with $\Delta t = 10^{-4}, \tau_{\mathrm{obs}} = 0.1$, and the simple dual representation (Eq. (6.3)) is used for both the training and the evaluation.

where γ is the viscous drag and T is the temperature.

In Fig. 6.1, we show the estimation results for the breathing parabola model. We train the model function $\boldsymbol{d}(\boldsymbol{x}, t|\boldsymbol{\theta})$, which is the neural network depicted in Fig. 6.2(b), using an ensemble of single transitions at $\mathcal{T}_{16}$ of 10^5 or 10^6 trajectories. We estimate the entropy production along a single trajectory (Fig. 6.1(b)), and the entropy production rate (Fig. 6.1(c)) using the trained model function $\boldsymbol{d}(\boldsymbol{x}, t|\boldsymbol{\theta}^*)$. The estimation results are compared with the analytical solutions, which are obtained using the fact that the probability density becomes a Gaussian distribution, and its variance evolves according to the Riccati equation [47]. For example, the thermodynamic force is explicitly obtained as

$$F(x,t) = \frac{t(3+3t+3t^2)x}{(1+t)(3+6t+6t^2+2t^3)}. \tag{6.19}$$

As we can see, the thermodynamic force is linear in terms of the position x but nonlinear in terms of the time t. The entropy production $\widehat{S}(t)$ is estimated along a trajectory by summing the estimated single-step entropy production:

$$\Delta\widehat{S}(t) := \boldsymbol{d}\left(\frac{\boldsymbol{x}_t + \boldsymbol{x}_{t+\Delta t}}{2}, t + \frac{\Delta t}{2}\,\middle|\boldsymbol{\theta}^*\right)(\boldsymbol{x}_{t+\Delta t} - \boldsymbol{x}_t), \tag{6.20}$$

while the true entropy production $S(t)$ is calculated by summing the true single-step entropy production:

$$\Delta S(t) := \boldsymbol{F}\left(\frac{\boldsymbol{x}_t + \boldsymbol{x}_{t+\Delta t}}{2}, t + \frac{\Delta t}{2}\right)(\boldsymbol{x}_{t+\Delta t} - \boldsymbol{x}_t). \tag{6.21}$$

Note that they are stochastic variables which depend on the realization of $\boldsymbol{x}(t)$.

In Fig. 6.1(b), the entropy production is estimated along a trajectory, i.e., evaluated at $\mathcal{T}_1$, while the model function is trained using the single transitions at $\mathcal{T}_{16}$. The good agreement with the true entropy production shows that the model function estimates the thermodynamics force well even at the time instances where the training data are absent. In Fig. 6.1(c), the entropy production rate is estimated using 10^5 or 10^6 trajectories. We can see the convergence of the estimate as the number of trajectories increases.

Next, we demonstrate the thermodynamic force estimation using a two-dimensional Langevin model, which has been used to study adaptive behaviors of living systems [34, 105, 106, 119]. The model consists of the output activity a, the negative controller m, and the input signal l, which is regarded as a deterministic protocol here. The dynamics of a and m are described by the following Langevin equation:

$$\dot{a}(t) = -\frac{1}{\tau_a}\left[a(t) - \bar{a}(m(t), l(t))\right] + \sqrt{2\Delta_a}\,\eta_a(t), \tag{6.22a}$$

$$\dot{m}(t) = -\frac{1}{\tau_m}a(t) + \sqrt{2\Delta_m}\,\eta_m(t), \tag{6.22b}$$

where τ_a and τ_m are the time constants satisfying $\tau_m \gg \tau_a$. The stationary value of the activity is determined by $\bar{a}(m(t), l(t))$ for which we assume a linear function $\bar{a}(m(t), l(t)) = \alpha m(t) - \beta l(t)$ in this study.

In Fig. 6.3(a), the average dynamics of a and m after the switching of l is plotted. The activity responds to the change of the input l for a while, and relaxes to the signal-independent value, which is called the adaptation. The adaptation often appears in living systems to maintain their sensitivity and fitness under time-varying environments. Specifically, this model is used to describe *E. coli* chemotaxis, where the activity a controls the motion of *E. coli* to move towards the gradient of the input molecules l [122].

In Fig. 6.3(b) and (c), we show the estimation results using an ensemble of single transitions at $\mathcal{T}_{10}$ of 10^6 trajectories. In this model, the estimation is difficult because of the rapid change of the state at the beginning, which diminishes the benefit of the continuous-time estimation. Nonetheless, we find that the model function is trained well to accurately estimate the thermodynamic force in Fig. 6.3(c), and thus the entropy production rate as well in Fig. 6.3(b). Note that the analytical expression of the thermodynamic force is linear in terms of a and m but nonlinear in terms of t similarly to Eq. (6.19), while it is too complex to show here.

The thermodynamic force shows the spatial trend of the dynamics as well as the local dissipation since it is proportional to the mean local velocity when the noise is additive $\boldsymbol{F}(\boldsymbol{x}, t) \propto \boldsymbol{j}(\boldsymbol{x}, t)/p(\boldsymbol{x}, t)$. For example, the thermodynamic force at the beginning ($t = 0$) reflects that the state tends to expand outside due to the rapid increase in the noise intensity Δ_a. As the state relaxes to the stationary state, the thermodynamic force begins to circulate around the stationary distribution gradually. Interestingly, the thermodynamic force is aligned in the direction of m at $t = 0.01$, which suggests that the dynamics of a becomes dissipationless.

So far, we have demonstrated the working of our estimation method. Next, we show the benefit of the continuous-time estimation that it can reduce the number of necessary trajectories to achieve the convergence by increasing the sampling frequency. Concretely, we study the ensemble size dependence of the estimate using the breathing parabola model in Fig. 6.4. The performance of the estimation is measured by the correlation between the estimated (Eq. (6.20)) and the true (Eq. (6.21)) single-step entropy production at $\mathcal{T}_1$ or $\mathcal{T}_{64}$ of 100 trajectories.

In Fig. 6.4(a), we show the convergence by increasing the number of time instances. We find that the estimate of the thermodynamic force improves independently of the evaluation time, which suggests that the estimate becomes overall accurate for the whole time interval $[0, \tau_{\mathrm{obs}}]$. The increase of the correlation evaluated at $\mathcal{T}_{64}$ shows that the single transitions at other than $\mathcal{T}_{64}$ improves the estimate of the thermodynamic force at $\mathcal{T}_{64}$. This suggests that the continuous-time estimation improves the estimate at time t using information of single transitions at neighboring times. In Fig. 6.4(b), we show the convergence by increasing the number of trajectories. We find that the correlation increases in a similar manner to Fig. 6.4(a), while the increase is larger in (a).

Therefore, the continuous-time estimation is data efficient since it fully utilizes the information that trajectories have as a whole, and its estimate improves by increasing the number of time instances as well as the number of trajectories. We can increase the number of time instances, for example, by increasing the sampling frequency (i.e., decreasing Δt), which may be easier to realize in experiments.

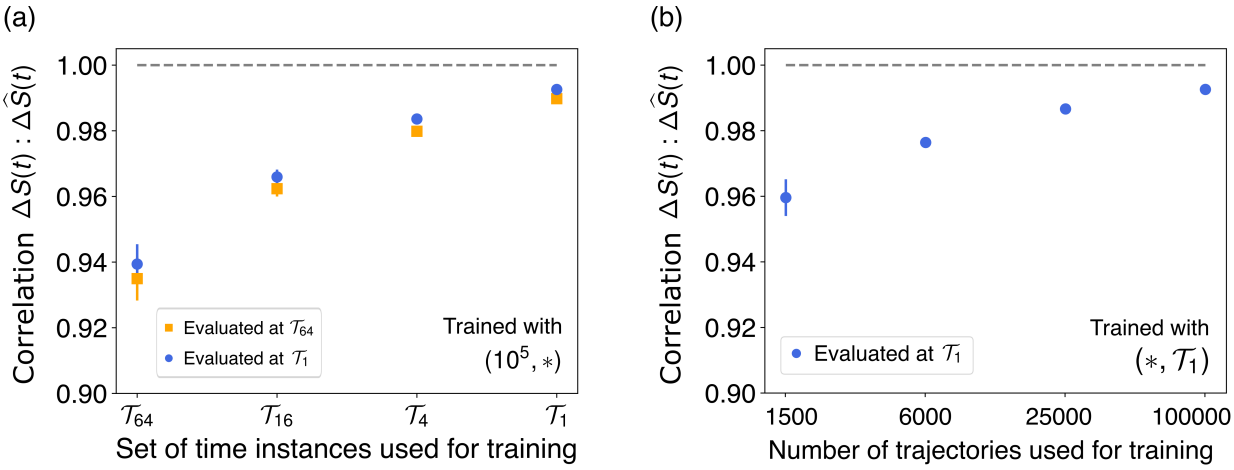

Figure 6.4: Convergence of the estimate by increasing (a) the number of time instances and (b) the number of trajectories used for training the model function. The blue circles (resp. orange squares) are the correlation between the estimated (Eq. (6.20)) and the true (Eq. (6.21)) single-step entropy production along $\mathcal{T}_1$ (resp. $\mathcal{T}_{64}$) of 100 trajectories. The number of trajectories is fixed to 10^5 in (a), and the set of time instances is fixed to $\mathcal{T}_1$ in (b). The trajectories are sampled from the breathing parabola model with the same system parameters as in Fig. 6.1, and the mean and its standard deviation of 10 independent trials are plotted.

6.4.2 Practical effectiveness

Here, we demonstrate the practical effectiveness of our method. Concretely, we consider the following four cases: (i) with a smaller number of trajectories, (ii) with a larger sampling interval, (iii) with a measurement error, and (iv) with a synchronization error. In Fig. 6.5, we show the results of the estimation with these changes using the adaptation model. Note that we consider a shorter observation time $\tau_{\rm obs} = 0.01$ to reduce the computational cost here.

In Fig. 6.5(a)-(c), we show the results of the estimation with 1000 trajectories. To improve the convergence, we consider to use the modified network depicted in Fig. 6.2(c). In Fig. 6.5(a), we compare the performance of the normal and the modified networks. We find that the modified network performs better at the beginning ($t = 0$), while they perform equally well at later times. Since we have the criterion that the higher test value is the better, we can choose the modified network in practice on the basis of the estimate at $t = 0$.

In addition, we consider to use $\mathrm{Var}(J_{\boldsymbol{d}})/2\mathrm{d}t$ as an estimator of the entropy production rate. In Fig. 6.5(b) and (c), we compare the continuous-time estimation with the instantaneous-time estimation using (b) $\sigma_{\rm Simple}$ and (c) $\mathrm{Var}(J_{\boldsymbol{d}})/2\mathrm{d}t$ as estimators of the entropy production rate. These estimators are used after training the model function with the simple dual representation. For the instantaneous-time estimation, we use the normal neural network that drops t from the input layer (see Table 6.2 for the hyperparameters), and perform the gradient ascent for each time t independently. As expected, we find that the use of $\mathrm{Var}(J_{\boldsymbol{d}})/2\mathrm{d}t$ significantly reduces the statistical error for the continuous-time estimation, while this is not the case for the instantaneous-time estimation.

Next, we study the effect of a larger sampling interval Δt. In Fig. 6.5(d), we show the estimation results with three choices for Δt and the time interval of the generalized current $\tau = m\Delta t$ ($m \geq 1$). We find that the estimate becomes lower than the true entropy production rate as we increase τ. Since the bias becomes small as the time variation of the entropy production rate vanishes, the lower estimate would be caused by the averaging due to the large time interval.

However, a larger time interval τ is sometimes beneficial. In Fig. 6.5(e), we study the effect of a measurement error by changing its strength Λ and the time interval with $\tau = \Delta t$. Here, the measurement error is added to the trajectory data in the same manner as in Sec. 5.5.3:

$$\boldsymbol{y}_{i\Delta t} = \boldsymbol{x}_{i\Delta t} + \sqrt{\Lambda}\boldsymbol{\eta}^i, \tag{6.23}$$

where Λ is the strength of the error, and $\boldsymbol{\eta}^i$ is the Gaussian white noise satisfying $\left\langle \eta_a^i \eta_b^j \right\rangle = \delta_{a,b}\delta_{i,j}$. The strength Λ is compared to $\Lambda_0 = 0.03$ which approximates the standard deviation of m. We find that the measurement error makes the estimate lower than the true entropy production rate, while a larger time interval τ can mitigate this effect. This result is in accordance with the result in Sec. 5.5.3.

Lastly, we study the effect of a synchronization error in Fig. 6.5(f). Here, we introduce the synchronization error by starting the sampling of each trajectory at time

$$\tilde{t} = \left\lfloor \frac{\mathrm{uni}(0, \Pi)}{\Delta t} \right\rfloor \Delta t, \tag{6.24}$$

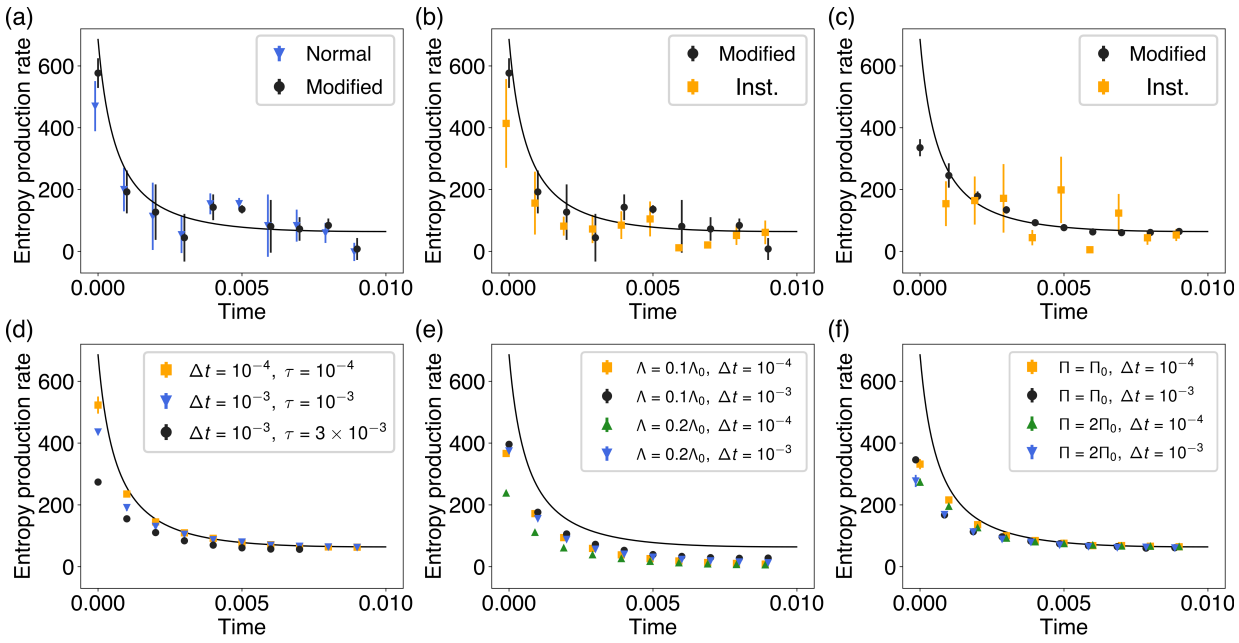

Figure 6.5: Practical effectiveness of the continuous-time estimation in the adaptation model. (a) Comparison between the normal and the modified neural networks. The modified network shows the better convergence at the initial time. (b) Comparison between the instantaneous-time estimation and the continuous-time estimation with the modified network. (c) The same comparison using $\widehat{\mathrm{Var}(J_{\boldsymbol{d}})}/2\mathrm{d}t$ as an estimator of the entropy production rate. Only the continuous-time estimation improves. The orange square is missing at $t = 0$ since the value becomes much higher. (d) Effect of the larger sampling interval. Δt is the sampling interval of the trajectories, and τ is the time interval of the generalized current. As τ increases, the estimate becomes lower than the true value. The black circles are missing at $t = 0.008, 0.009$ since a pair of $\{\boldsymbol{x}_{i\Delta t}, \boldsymbol{x}_{(i+3)\Delta t}\}$ is used for calculating the generalized current. (e) Effect of the measurement error. As the measurement error Λ increases, the estimate becomes lower than the true value. A larger time interval τ can mitigate this effect (τ is set to Δt in this plot). (f) Effect of the synchronization error. The estimate becomes an averaged value in the time direction, and this effect is small when the dynamics is close to stationary. In contrast to (e), the time interval τ does not affect this effect ($\tau = \Delta t$). For (a)-(c), 1000 trajectories with $\mathcal{T}_1$ are used for the estimation with $\tau = \Delta t = 10^{-4}$. For (d)-(f), 10000 trajectories with $\mathcal{T}_1$ are used for the estimation, and the modified neural network is used for the model function, and $\widehat{\mathrm{Var}(J_{\boldsymbol{d}})}/2\mathrm{d}t$ is used for estimating $\widehat{\sigma}$ after the learning. For (a)-(f), the simple dual representation is used for the training, and the black line is the true entropy production rate, and the mean and its standard deviation of four independent trials are plotted. The system parameters are the same as in Fig. 6.3 except $\tau_{\mathrm{obs}} = 0.01$.

where $\mathrm{uni}(0, \Pi)$ returns a value x uniformly randomly from $0 < x \leq \Pi$, and the brackets denote the floor function. For example, when $\tilde{t} = 3\Delta t$, we obtain a trajectory for $t = 0, \Delta t, ...$ as $\{\boldsymbol{x}_{3\Delta t}, \boldsymbol{x}_{4\Delta t}, ...\}$. The strength of the error Π is compared to $\Pi_0 = 5 \times 10^{-4}$ which approximately satisfies $\sigma(\Pi_0) \approx \sigma(0)/2$. We find that the effect of the synchronization error appears as an averaging in the time direction similarly to Fig. 6.5(d). In this case, the choice of the time interval τ does not affect the estimation much.

In contrast to the stationary case, we need to carefully choose the time interval τ for the generalized current in non-stationary dynamics. This is because when the true entropy production rate increases in time, a larger time interval may lead to a higher estimate of the entropy production rate as suggested by Fig. 6.5(d), which is incompatible with our criterion to select the higher test value.

6.5 Conclusions

In this chapter, we have developed an efficient estimation method for the non-stationary entropy production by extending the method in Chap. 5. First, we have established the theoretical relationship among the variational representations in terms of the range of applicability, the optimal coefficient, and the tightness of the bound as summarized in Table 6.1. Specifically, we have derived the simple dual representation in Eq. (6.3), which reveals the tightness of the bounds as in Eq. (6.4). In addition, we have shown that the NEEP is related to a dual representation of the KL divergence in Eq. (6.8), and it is applicable to non-stationary dynamics.

On the basis of the result, we have proposed the continuous-time estimation scheme which trains a model function continuously in time using the objective function defined in Eq. (6.12). We have demonstrated the effectiveness of our method using the two linear Langevin models. Our method gives an exact estimate on the entropy production and the thermodynamic force as presented in Figs. 6.1 and 6.3. In addition, we have shown that the estimate converges not only by increasing the number of trajectories but also by increasing the number of time instances in Fig. 6.4, which would lower the hurdle for the experimental realization. Finally, we have tested our method in various setups, for example, with errors in measurement and synchronization in Fig. 6.5.

Our method is of practical significance since it requires only an ensemble of trajectories, and it is data efficient. One of the prominent fields for the future application would be the study of biological [109] or active matter systems [123].

6.6 Supplementary to Chapter 6

In this section, we show supplementary results. In Sec. 6.6.1, we compare the performance of the variational representations. In Sec. 6.6.2, we show an example of the hyperparameter tuning of the neural networks.

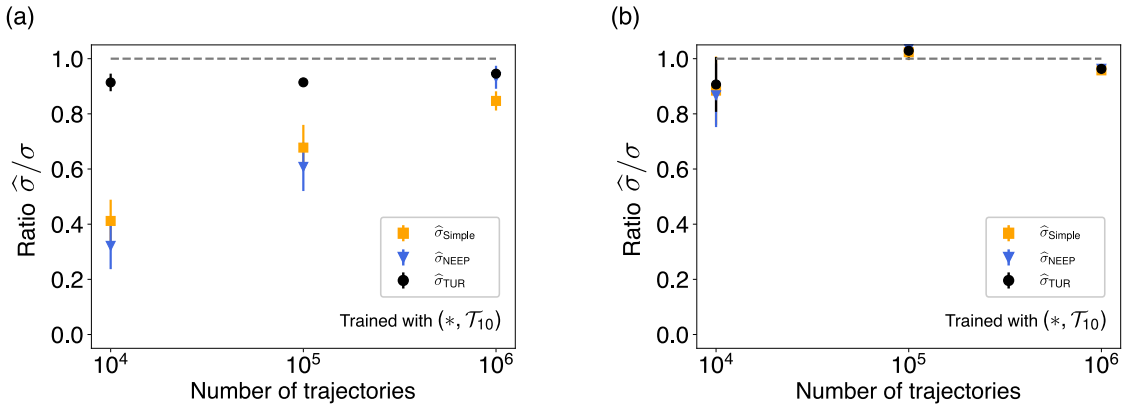

Figure 6.6: Comparison of the convergence among $\widehat{\sigma}_{\mathrm{Simple}}$ (orange squares), $\widehat{\sigma}_{\mathrm{NEEP}}$ (blue triangles), and $\widehat{\sigma}_{\mathrm{TUR}}$ (black circles) in the adaptation model at time (a) $t = 0$ and (b) $t = 0.09$. The system parameters are the same as in Fig. 6.3, and the mean and its standard deviation of 10 independent trials are plotted.

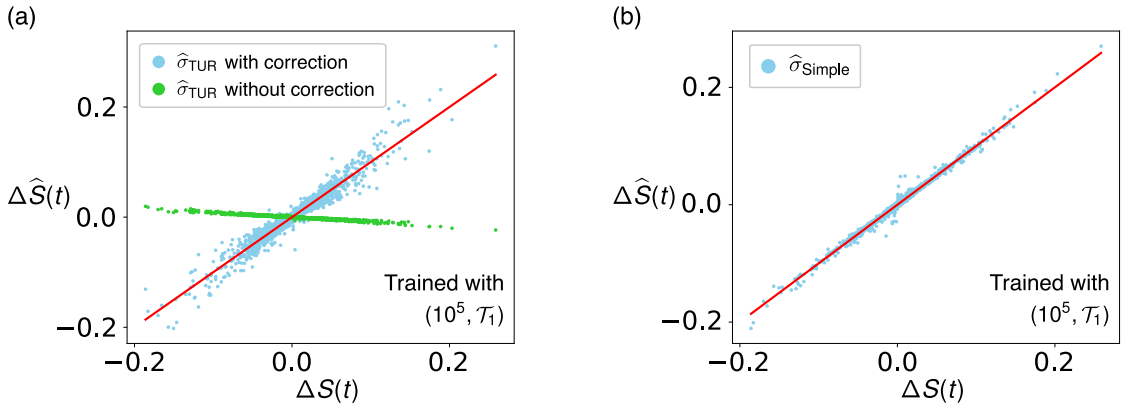

Figure 6.7: Comparison of the thermodynamic force estimation between (a) the short-time TUR and (b) the simple dual representation. The scatter plots between the estimated (Eq. (6.20)) and the true (Eq. (6.21)) entropy production along 20 trajectories are shown. In panel (a), the green dots are the estimation before the correction of the constant factor $c(t)$, while the blue dots are after the correction. As shown in (a), the correction of $c(t)$ typically increases the statistical error. The system parameters are the same as in Fig. 6.1 except $\Delta t = 10^{-2}$ and $\tau_{\mathrm{obs}} = 2.0$ to suppress the bias of σ_{TUR}.

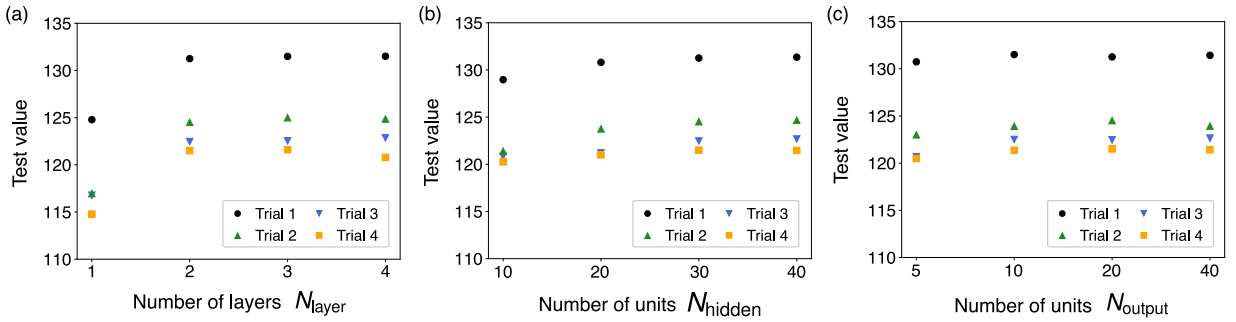

Figure 6.8: Hyperparameter tuning of the modified network in the adaptation model. The test values of four independent trials are plotted with different markers respectively. These plots suggest that, for example, we can safely choose N_{layer} larger than 1 even if we only have access to a single set of trajectories, which is the case in practice. The system parameters are the same as in Fig. 6.5 with $\tau = \Delta t = 10^{-4}$, and 10000 trajectories are used.

6.6.1 Comparison among the variational representations

Here, we compare the performance of the variational representations in terms of the estimation of the entropy production rate (Fig. 6.6) and the thermodynamic force (Fig. 6.7).

In Fig. 6.6, we show the convergence of the estimated entropy production rate at (a) $t = 0$ and (b) $t = 0.09$ of the adaptation model. We find that the short-time TUR realizes the fastest convergence, while the NEEP and the simple dual representation show similar convergence, which is in accordance with the discussion in Sec. 6.2. The convergence at $t = 0$ is slow since the estimation is difficult due to the rapid change in the state, which diminishes the benefit of the continuous-time estimation.

In Fig. 6.7, we show the scatter plots between the estimated (Eq. (6.20)) and the true (Eq. (6.21)) single-step entropy production evaluated along 20 trajectories when (a) the short-time TUR and (b) the simple dual representation are used for training the model function. In Fig. 6.7(a), the scatter plot before the correction of the constant factor $c(t)$ is shown with the green dots. Interestingly, we find that $c(t)$ is almost constant in this case. We can see that the dots after the correction in (a) has a larger statistical error than those before the correction and those in (b). It is an interesting future issue to estimate the constant factor $c(t)$ with small statistical error. For example, if we can ensure that $c(t)$ is constant independent of t, we can use the whole trajectories to estimate $c(t)$, which would significantly decrease the statistical error.

6.6.2 Hyperparameter tuning

Here, we explain the hyperparameter tuning of the neural networks. In Fig. 6.8, we show an example of the hyperparameter tuning in the modified network. The test values of four independent trials, each of which uses 10000 trajectories, are shown in these plots. As explained in Chap. 5, we adopt the hyperparameter values that maximize the test value. On the basis of these plots, we adopt $N_{\mathrm{layer}} = 2, N_{\mathrm{hidden}} = 30, N_{\mathrm{output}} = 20$ for the modified

Model	Neural network	N_{layer}	N_{hidden}	N_{output}	N_{step}
Breathing parabola model	normal	3	10		1000
Adaptation model	normal	3	30		50000
	time-independent	2	20		50000
	modified	2	30	20	5000

Table 6.2: Hyperparameters used for the neural networks. N_{layer} is the number of hidden layers, and N_{hidden} is the number of units in each hidden layer, and N_{output} is the number of units in the output layer for the modified network (gray units in Fig. 6.2(c)), and N_{step} is the iteration number of the gradient ascent. The normal network is depicted in Fig. 6.2(b), and the modified network is depicted in Fig. 6.2(c), and the time-independent network is the normal network that drops t from the input layer. Since we find that the step size of the gradient ascent α does not affect the performance much in these model functions, $\alpha = 1$ is used in this chapter.

neural network in this study. In Table 6.2, we summarize the hyperparameter values used in this study.

Chapter 7

Conclusions and future perspectives

7.1 Conclusions

In this thesis, we have established the variational estimation method of the entropy production. As for the theoretical results, we have formulated the variational representations of the entropy production. On the basis of the results, we have made a platform for applying machine learning to the estimation problem. Our method is of practical significance since all it requires are trajectory data and it is applicable to a broad class of stochastic dynamics out of equilibrium. Specifically, we have shown that our method is effective for non-linear, high-dimensional, and non-stationary dynamics.

In Chapter 5, we have investigated the theoretical framework for estimation of the entropy production using the short-time TUR along with machine learning techniques. First, we have formulated the short-time TUR both for Markov jump processes (Eq. (5.9)) and overdamped Langevin dynamics (Eq. (5.18)), and proved their equality conditions. As a result, we have found that the equality of the short-time TUR is always achievable in Langevin dynamics, while this is not the case in general Markov jump processes. Next, we have proposed the variational estimation method for stationary entropy production by employing ideas from machine learning such as the gradient ascent and the data splitting scheme. We have constructed the learning estimators [the binned learning estimator $\widehat{\sigma}^{\lambda}[\boldsymbol{d}_{\mathrm{bin}}]$ as in Eq. (5.49), the Gaussian learning estimators $\widehat{\sigma}[\boldsymbol{d}_{\mathrm{Gauss}}]$, $\widehat{\sigma}[\boldsymbol{d}_{\mathrm{Gauss}}]$ as in Eqs. (5.55) and (5.56)] for Langevin dynamics and compared them with the KDE estimators defined in Sec. 4.2. We have found that the learning estimators outperform the KDE estimators especially at high-dimensional and non-linear setups as shown in Figs. 5.5 and 5.7. We have also formulated the estimation in Markov jump processes and proposed the learning estimator $\widehat{\sigma}^{M}[d]$ in Sec. 5.2.3. The learning estimator $\widehat{\sigma}^{M}[d]$ gives only a lower bound on the entropy production rate in general. However, as an advantage of the learning estimator, we have found that it is robust against the choice of the sampling interval as shown in Fig. 5.9. In summary, we have established the variational estimation scheme using the short-time TUR and resolved the three remaining issues presented in Sec. 4.4.2.

In Chapter 6, we have developed the continuous-time estimation method for non-stationary entropy production, extending the learning algorithm developed in Chapter 5. First, we have established the theoretical relationship between the variational representa-

tions in terms of the range of applicability, the optimal coefficient, and the tightness of the bound as summarized in Table 6.1. Especially, we have derived the simple dual representation in Eq. (6.3) from the NEEP and revealed the tightness of the bounds as in Eq. (6.4). Next, we have proposed the continuous-time estimation that trains the model function continuously in time with an objective function defined by Eq. (6.12) using an ensemble of trajectories. For the model function, we have adopted the neural networks depicted in Fig. 6.2. We have numerically demonstrated our method using linear Langevin models and comparing the estimation results with the analytical solutions. We have checked that the continuous-time estimation gives an exact estimate on the entropy production and the thermodynamic force as shown in Figs. 6.1 and 6.3. We have shown that the continuous-time estimation is data efficient since the estimate converges not only by increasing the number of trajectories but also by increasing the number of time instances contained in each trajectory in Fig. 6.4. Finally, we have demonstrated the practical effectiveness of our method by considering various perturbations to the setup in Fig. 6.5.

7.2 Future perspectives

We discuss some future perspectives. First, an application of the estimation method for biological experimental data would be the most important future issue. In the last few years, several methods have been proposed to estimate the entropy production on the basis of trajectory data [44, 93, 100, 124], while there are only a few successful applications beyond the detection of the broken detailed balance [39–41]. This may be because it is often the case in experiments that only a part of the total system is observable. The estimation in coarse-grained dynamics leads to an estimate lower than the total entropy production [42, 125, 126], which makes the meaning of the estimated entropy production unclear. Thus, it is interesting to apply our method to easily tractable systems such as F_1-ATPase first, where the estimation of the information-thermodynamic dissipation would deepen our understanding on the energetics as discussed in Appendix A. On the other hand, it is a fundamentally important issue to extract useful information on the system from the entropy production of the coarse-grained dynamics.

To directly tackle the coarse-graining problem, a further development of our machine learning method is desirable. For example, a new estimation scheme that can fully utilize the information contained in multiple transitions has been recently proposed [96]. It is shown that the proposed method can estimate the entropy production of hidden dynamics to a great extent, while it is only applicable to a few state systems. On the other hand, it is shown in Ref. [111] that the machine learning method with the NEEP representation can be applied to the estimation using multiple transitions. However, their relationship is not clear, and it is interesting to explore the direction in between them.

Another interesting direction would be the problem of the free energy estimation [127–129]. The aim of this problem is to estimate the free energy difference between two thermodynamic states by simulating multi-particle Langevin dynamics given the energy function of the thermodynamic states. The free energy difference is calculated by the equality called free energy perturbation [127], which is a special limit of the Jarzynski equality [1]. Although this problem has a long history, it has been still actively studied from the machine

learning perspective [129]. Since the problem setting is somewhat similar to the entropy production estimation and our method can be directly applied to this problem in principle, it is interesting to consider a connection between these two streams of research. For this purpose, it will be helpful to deepen our understanding on the TUR and stochastic thermodynamics of multi-particle systems.

Appendix A

Information thermodynamics of F_1-ATPase

In this appendix, we investigate the information-thermodynamic efficiencies of F_1-ATPase (or F_1). In Sec. A.1, we give a short introduction to this subject. In Sec. A.2, we explain the setup of our study based on a reaction-diffusion model of F_1. In Secs. A.3 and A.4, we show numerical and analytical results on the behavior of information-thermodynamic quantities. We find that the rotational degree of freedom plays the role of Maxwell's demon, which leads to a small amount of internal heat dissipation. We also find that the information-thermodynamic efficiencies increase as we apply an external force against the rotation. As a result, the internal heat dissipation can be even negative, which is analogous to artificial systems realizing Maxwell's demon [27, 28, 50]. The results presented in this appendix are based on our manuscript in preparation [130].

A.1 Introduction

As we have reviewed in Sec. 1.1, our understanding on the relation between the thermodynamic entropy and information flow has been deepened recently, which is formulated as information thermodynamics. Information propagation and energetic consumption are the essential aspects of biological systems, and information thermodynamics is expected to reveal fundamental limits of biological phenomena from these perspectives. In fact, it has been applied, for example, to chemotaxis of *E. coli* [119], and information propagation in reaction networks [131] and in sensory systems [132, 133], to reveal the effect of information flow on thermodynamic quantities. We are now in a good position to study information thermodynamics of molecular motors [134,135], which work in non-equilibrium steady states and whose motions are elaborately controlled, suggesting the existence of information flow.

ATP synthase is a molecular motor that produces adenosine triphosphate (ATP), the energy currency of a cell, in almost all organisms including bacteria, plants, and animals [136]. In addition to its importance in biological systems, the elegant mechanics and energetic properties of F_1 have attracted much attention. In experiments, we often focus on a subpart of ATP synthase called F_1-ATPase (or F_1) [134, 137], whose central γ shaft

rotates within a cylinder consisting of three α and β subunits [138, 139]. F_1 works as an enzyme of ATP hydrolysis, and its 120° rotation is tightly coupled to the following reaction in a reversible manner: ATP $\rightleftarrows$ ADP + phosphate (P_i) [140, 141] (see Fig. A.1 for a schematic). In the free rotation setup, the reaction goes to the ATP hydrolysis direction if there are sufficient ATP molecules, while it can be reversed to the ATP synthesis direction by rotating the γ shaft in the opposite direction with external force.

F_1 is known to be thermodynamically efficient [142, 143]. In experiments, a probe bead is attached to the γ shaft, and the chemical free energy ($\Delta\mu$) extracted from the ATP hydrolysis is dissipated through the rotation of the bead ($Q_{\rm ext}$) or the main body's conformational change ($Q_{\rm int}$). Interestingly, according to recent experiments [50, 89, 144], the internal heat dissipation $Q_{\rm int}$ is almost zero in all the free rotation setups [50]. As we apply external force against the rotation, $Q_{\rm ext}$ decreases while keeping $Q_{\rm int}$ close to zero, and 100% efficiency is realized for the energy conversion from $\Delta\mu$ to the extracted work in the stall force limit [89, 144].

In previous theoretical studies [145–147], it has been shown that a reaction-diffusion model explains the experimental results well. Especially, the model called TASAM (totally asymmetric allosteric model) well reproduces the above energetic properties of F_1 [147]. This model describes the motion of the bead as a Brownian particle in three potentials, each of which corresponds to an internal state (see Fig. A.1). On the basis of this model, the small internal heat dissipation can be explained by the fact that the internal state jumps when the position of the bead is close to the potential intersection points. Since such feedback structure usually entails information flow, F_1 is interesting from the information-thermodynamic perspective. However, a quantitative understanding of the interplay between the heat dissipation and information flow has been still lacking.

In the following, we study information thermodynamics of F_1-ATPase. After we introduce the reaction-diffusion model and information-thermodynamic quantities in Sec. A.2, we show our results in Sec. A.3.

A.2 Setup

In this section, we introduce the reaction-diffusion model of F_1. We also formulate information thermodynamics on the basis of this model.

A.2.1 Reaction-diffusion model

We introduce the reaction-diffusion model proposed in Refs. [146, 147]. The model consists of two degrees of freedom, the angular position of the probe bead x, and the state of the main body's conformation n. The model is described as a one-dimensional system with $x \in (-\infty, \infty)$ and $n \in \mathbb{Z}$, where $\mathbb{Z}$ is the set of integers. We interpret it as a model of F_1 by identifying x and $x+2\pi$, n and $n+3$, which maps the state space as $(-\infty, \infty) \to [0, 2\pi)$ and $\mathbb{Z} \to \{0, 1, 2\}$. There are three trapping potentials at 0, $2\pi/3, 4\pi/3$ rad, and n represents the potential in which the bead is trapped. The bead shows a Brownian motion inside a potential, and at some point the potential is switched to the next potential. Then, the bead moves towards the center of the next potential. As we describe below, these processes

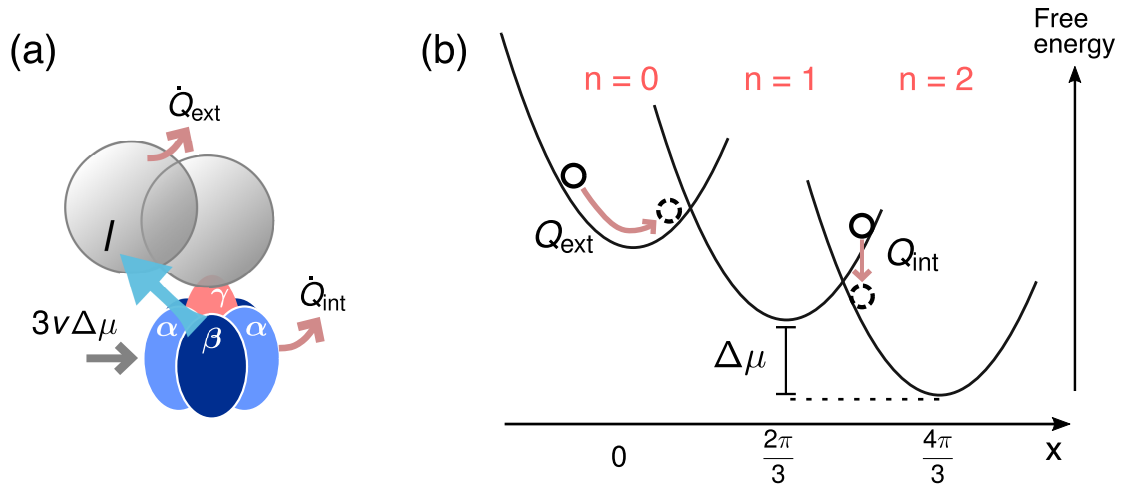

Figure A.1: Energetics of F_1-ATPase in the free rotation. (a) The rate of energy flow. We study the effect of information flow l on the heat dissipation $\dot{Q}_{\rm int}$ and $\dot{Q}_{\rm ext}$. (b) The free-energy landscape of the reaction-diffusion model. The probe bead is described as a Brownian particle inside a potential, and the potential switches to the next potential stochastically depending on the free energy difference. Because of the chemical free energy $\Delta\mu$, the bead tends to move in the positive direction.

occur stochastically.

The dynamics of x is described by an overdamped Langevin equation:

$$\Gamma\dot{x}(t) = -\frac{\partial}{\partial x}U_n(x(t)) - F + \sqrt{2\Gamma T}\eta(t), \tag{A.1}$$

where $\eta(t)$ is a Gaussian white noise with unit variance, Γ is the friction coefficient, F is an external force applied against the free rotation direction, and T is the temperature of the medium. $U_n(x)$ is the nth potential given by

$$U_n(x) = \frac{k}{2}\left(x - nL\right)^2, \tag{A.2}$$

where k is the spring constant, and L is the distance between the potentials $L = 2\pi/3$ rad.

On the other hand, the dynamics of n is described by a Markov jump process whose transition rates satisfy the detailed balance condition:

$$\frac{R_n^+(x)}{R_{n+1}^-(x)} = \exp\left\{\frac{1}{T}\left[U_n(x) - U_{n+1}(x) + \Delta\mu\right]\right\}, \tag{A.3}$$

where $R_n^+(x)$ is the forward transition $(n \to n+1)$ rate at x, and $R_{n+1}^-(x)$ is the backward transition $(n+1 \to n)$ rate at x. $\Delta\mu$ is the free energy difference between a single molecule ATP and ADP + Pi, which can be expressed as $\Delta\mu = \Delta\mu_0 + T\log\left(n_{\rm ATP}/n_{\rm ADP}n_{\rm Pi}\right)$ using the concentrations of the nucleotides n_i. In experiments, these concentrations can be varied, and thus $\Delta\mu$ is a control parameter.

We further express the transition rates explicitly introducing parameters $0 \leq q \leq 1$ and $W > 0$ as

$$R_n^+(x) = W \exp\left\{ \frac{q}{k_B T} \left[U_n(x) - U_{n+1}(x) + \Delta\mu \right] \right\}, \tag{A.4}$$

$$R_{n+1}^-(x) = W \exp\left\{ \frac{q-1}{k_B T} \left[U_n(x) - U_{n+1}(x) + \Delta\mu \right] \right\}. \tag{A.5}$$

The switching rate W depends on the concentrations of the nucleotides, and if we scale n_{ATP} as cn_{ATP} while fixing $\Delta\mu$ constant, W also scales linearly cW [146]. It has been shown that the model with $q = 0 \sim 0.1$ well reproduces the energetic properties of F_1, and especially the model with $q = 0$ is called TASAM [147]. In this model, the forward transition occurs independently of the position x, while its backward transition is strongly dependent on the position.

We note that the model introduced here is a simplified version. It is known that there is a substate at around $nL + 2L/3$ ($= 80°$) between the potentials [148, 149]. The first $2L/3$ substep is associated with ATP binding and ADP release, while the next $L/3$ substep is associated with Pi release and ATP hydrolysis. However, since the latter substep is very fast, it cannot be detected unless a mutated F_1 is used [150–152]. In the previous study [147], the effect of this substep is taken into account by modifying the harmonic potential (Eq. (A.2)), while it does not change the energetic properties so much from the harmonic potential case. Thus, we adopt the model with three harmonic potentials in this study.

In the numerical experiments, we vary W as a control parameter and consider the stationary state. The stationary distribution $p(n, x)$ is normalized as

$$\sum_{n=0,1,2} \int_{-\infty}^{\infty} \mathrm{d}x p(n, x) = 1. \tag{A.6}$$

Then, the rotational velocity v can be calculated by

$$v = \int_{-\infty}^{\infty} \mathrm{d}x \Lambda_n(x), \tag{A.7}$$

$$\Lambda_n(x) := p(n, x) R_n^+(x) - p(n+1, x) R_{n+1}^-(x), \tag{A.8}$$

where $\Lambda_n(x)$ is the local flux in n for a given position x. There is a saturation velocity $v_{\max}$ in the limit of $W \to \infty$ (see Sec. A.4.1), and F_1 follows the Michaelis-Menten like curve in terms of W. It should be noted that the diffusion of the bead serves as the rate-limiting process in this model. However, the actual rate-limiting process is considered to be the $L/3$ substep [152], which becomes non-negligible in the fast switching limit.

A.2.2 Information thermodynamics

In this subsection, we formulate information thermodynamics of F_1 on the basis of the reaction-diffusion model. Note that we only consider averaged quantities in this chapter.

First, we introduce heat dissipation. There are two types of heat dissipation $Q_{\rm int}$ and $Q_{\rm ext}$ associated with the dynamics of n and x, respectively (see Fig. A.1 for a schematic). $Q_{\rm int}$ is the internal heat dissipation during the potential switching. Its rate $\dot{Q}_{\rm int}$ can be calculated using the local flux $\Lambda_n(x)$ as

$$\dot{Q}_{\rm int} := \sum_{n=0,1,2} \int_{-\infty}^{\infty} {\rm d}x \Lambda_n(x) \left[U_n(x) - U_{n+1}(x) + \Delta\mu \right]. \tag{A.9}$$

$Q_{\rm ext}$ is the external heat dissipation during the rotation of the probe bead. Its rate $\dot{Q}_{\rm ext}$ is calculated by

$$\dot{Q}_{\rm ext} := \left\langle \dot{x} \left(-\frac{\partial}{\partial x} U_n(x) - F \right) \right\rangle, \tag{A.10}$$

which is the definition introduced in Sec. 2.1. Since the chemical free energy $\Delta\mu$ is consumed per $2\pi/3$ rotation and the extracted work during the process is FL, the first law of thermodynamics holds as follows:

$$\dot{Q}_{\rm int} + \dot{Q}_{\rm ext} = |3v(\Delta\mu - FL)|. \tag{A.11}$$

In the numerical experiments, we use Eq. (A.11) rather than Eq. (A.10) to calculate $\dot{Q}_{\rm ext}$ since Eq. (A.9) is easier to calculate than Eq. (A.10) numerically.

Next, we introduce the learning rate and the information-thermodynamic dissipation. The learning rate is a measure of information flow in bipartite systems. Since the reaction-diffusion model satisfies the bipartite condition (Eq. (2.63)), we define the learning rate l_x and l_n as in Eq. (2.70), which satisfy

$$l_x = -l_n \tag{A.12}$$

in the stationary state. Note that we use the small letters here by viewing x and n as stochastic variables unlike Eq. (2.70). We also define the information-thermodynamic dissipation as in Eq. (2.67):

$$\sigma_n = \frac{\dot{Q}_{\rm int}}{T} - l_n, \tag{A.13}$$

$$\sigma_x = \frac{\dot{Q}_{\rm ext}}{T} - l_x, \tag{A.14}$$

which take non-negative values $\sigma_x \geq 0$ and $\sigma_n \geq 0$. In the next section, we show that $l_x > 0$ ($l_n < 0$) holds for the model with $q = 0$, which means that x plays the role of Maxwell's demon or the feedback controller. In this case, we define the information-thermodynamic efficiencies as

$$\eta_n := \frac{\dot{Q}_{\rm int}}{T l_n}, \tag{A.15}$$

$$\eta_x := \frac{T l_x}{\dot{Q}_{\rm ext}}, \tag{A.16}$$

which satisfy $\eta_n \leq 1$ and $\eta_x \leq 1$.

We explain the meaning of the information-thermodynamic efficiencies. As explained in Sec. 2.3, the learning rate l_x (resp. l_n) quantifies the increase of the mutual information between x and n by the transition of x (resp. n). The positive learning rate $l_x > 0$ means that x gets information on n, which requires the positive heat dissipation $\dot{Q}_{\rm ext} > 0$. Thus, η_x quantifies the efficiency of acquiring information with necessary heat dissipation. On the other hand, the negative learning rate $l_n < 0$ means that the dynamics of n consumes the correlation, which can decrease the internal heat dissipation. Especially, when $\dot{Q}_{\rm int}$ is negative, η_n is meaningful since it quantifies how efficiently the feedback control performed by x on n converts the correlation into the heat absorption, which is a phenomenon unique to information-thermodynamic setups.

A.3 Main results

We now show our main results. We study the behavior of the information-thermodynamic quantities with and without external force by changing the switching rate W. We find that the rotational degree of freedom plays the role of Maxwell's demon ($l_x > 0$) for the realistic model $q = 0, 0.1$, and the effect of the feedback is relevant in the slow rotation regime. The information-thermodynamic dissipation shows monotonic behavior unlike the heat dissipation, which provides us a clear understanding on the small internal heat dissipation. We also find that the external force only decreases the information-thermodynamic dissipation while keeping the learning rate almost constant, which means that F_1 becomes information-thermodynamically efficient. As a result, we find that even the negative heat dissipation is realized.

In Fig. A.2, we show the relation between the rotational velocity and the information-thermodynamic quantities. Here, we use the following parameters $k_B = 1, \Delta\mu = 19 k_B T, \Gamma = k_B T/3.3L^2, k = 50 k_B T/L^2$ [147], and calculate the information-thermodynamic quantities numerically using the stationary distribution obtained by the exact diagonalization of the transition matrix. The information-thermodynamic quantities are normalized by $3v\Delta\mu/T$ so that $\tilde{\sigma}_x + \tilde{\sigma}_n = |1 - FL/\Delta\mu|$ holds. Here, we denote the normalization by the tilde symbol. For example, $\tilde{\sigma}_x$ quantifies the information-thermodynamic dissipation of x per potential switching.

We find that the learning rate of x becomes positive for the realistic model $q = 0, 0.1$, which means that the rotational degree of freedom behaves as Maxwell's demon. The normalized learning rate becomes large in the slow rotation limit, and its sign changes depending on q. In fact, in this limit, we can calculate the learning rate analytically as

$$\tilde{l}_x = \frac{kL^2(1-2q)}{2T\Delta\mu}, \tag{A.17}$$

and thus its sign changes at $q = 0.5$ (see Sec. A.4.1 for the analytical calculation). We note that since the velocity goes to zero in this limit, the learning rate also vanishes when it is not normalized.

Next, we find that the information-thermodynamic dissipation changes monotonously as the velocity increases. We analytically show that $\tilde{\sigma}_x = 0$ and $\tilde{\sigma}_n = 0$ hold in the slow and

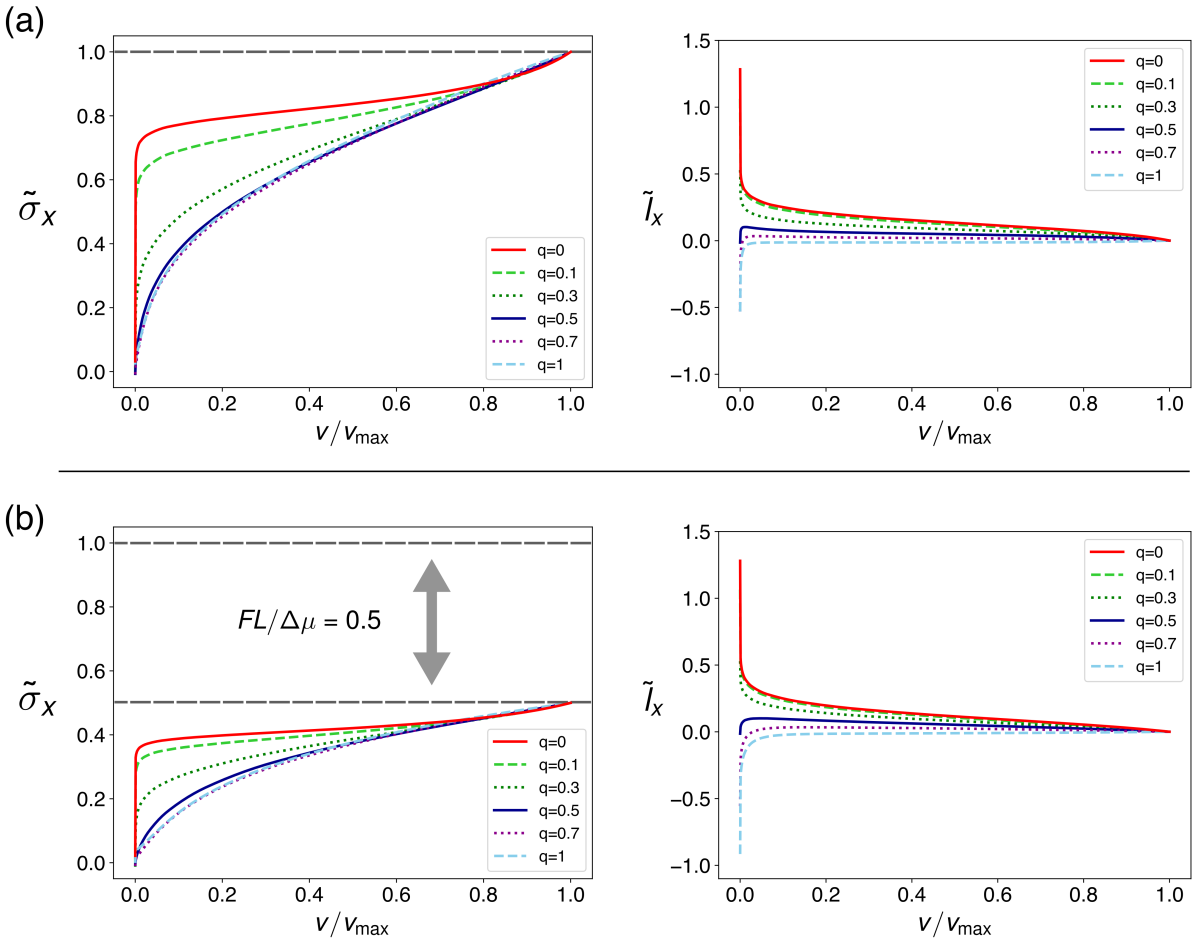

Figure A.2: Information-thermodynamic dissipation and learning rate. (a)(b) The rotational velocity versus the information-thermodynamic dissipation and the learning rate (a) in the free rotation and (b) with external force ($F = 0.5\Delta\mu/L$) for various choice of q. The information-thermodynamic quantities are normalized by $3v\Delta\mu/T$ so that $\tilde{\sigma}_x + \tilde{\sigma}_n = |1 - FL/\Delta\mu|$ holds, and the rotational velocity is normalized by the saturation velocity $v_{\max}$. The rotational velocity is varied by changing W from 10^{-10} to 10^{6}. The information-thermodynamic dissipation is decreased by the external force, while the learning rate is not affected much.

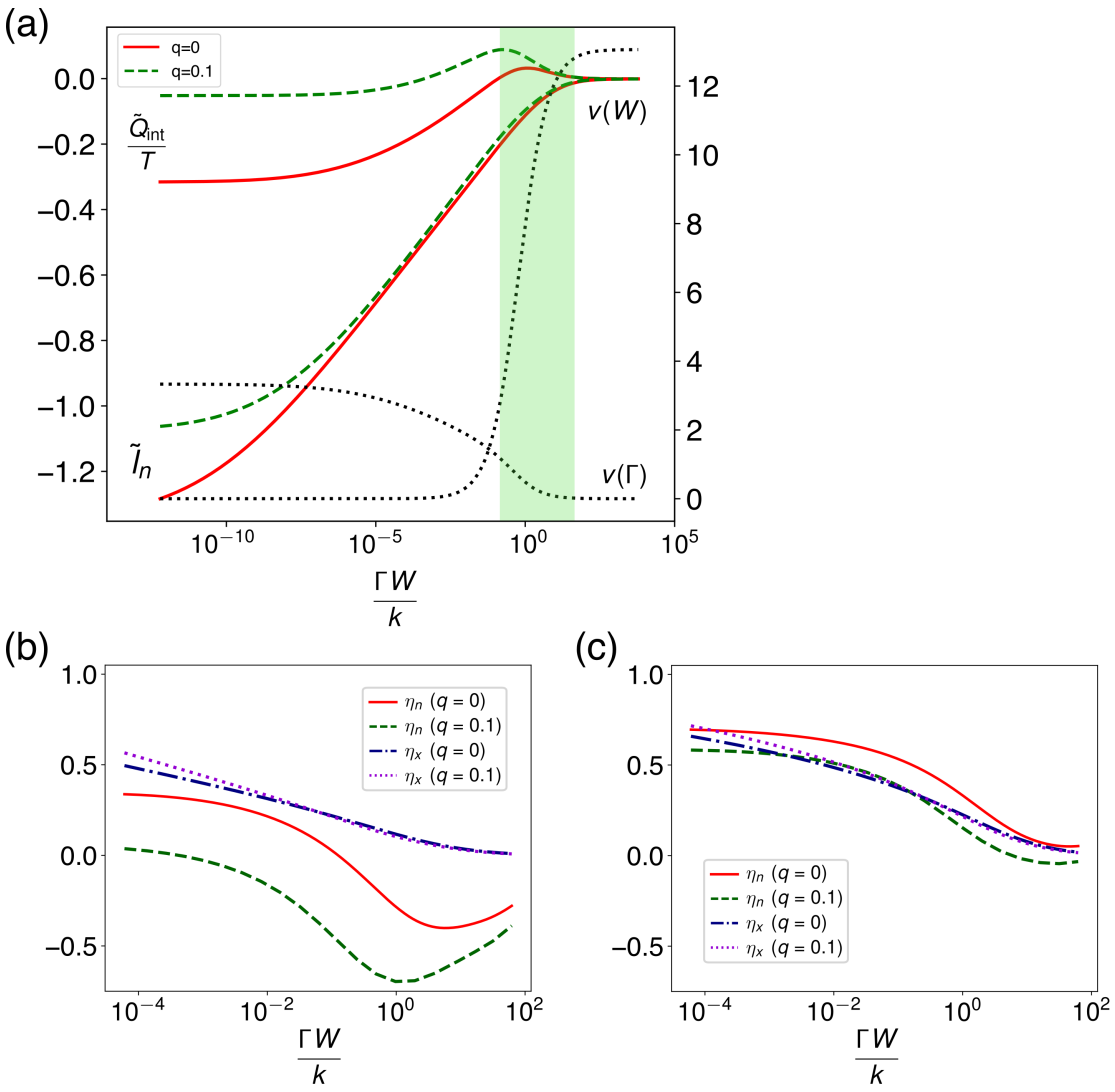

Figure A.3: Negative internal heat dissipation and information-thermodynamic efficiencies. (a) The time scale ratio versus the internal heat dissipation, the learning rate of n, and the velocity in the free rotation for $q = 0$ and $q = 0.1$. $v(\Gamma)$ (resp. $v(W)$) is the rotational velocity when Γ (resp. W) is varied. The left axis is for $\tilde{Q}_{\rm int}/T$ and $\tilde{l}_n$, and the right axis is for $v(\Gamma)$ and $v(W)$. The behavior of $\tilde{Q}_{\rm int}$ has been tested with experimental data for the green shaded region in Ref. [147]. (b)(c) The time scale ratio versus the information-thermodynamic efficiencies (b) in the free rotation and (c) with external force ($F = 0.5\Delta\mu/L$) for $q = 0$ and $q = 0.1$. As can be seen from $\eta_n > 0$, the internal heat dissipation is negative for most of the parameter values in (c). We note that Γ and W are varied, while k is fixed in these plots.

the fast switching limits respectively and they hold independently of the potential shape $U_n(x)$ (see Sec. A.4.1). Thus, we expect that the monotonic behavior of the information-thermodynamic dissipation reflects the change of the time scale ratio between x and n, while the monotonicity is not proved analytically in the intermediate regime.

It is experimentally shown that $\tilde{Q}_{\rm ext}/T \sim 1$ (or equivalently $\tilde{Q}_{\rm int}/T \sim 0$) holds independently of the velocity in the free rotation [50]. In the previous study [147], this result is explained by the fact that the potential switches when the bead is close to the potential intersection points for the $q = 0$ model. From the information-thermodynamic perspective, this result can be explained using the relation $\tilde{Q}_{\rm ext}/T = \tilde{\sigma}_x + \tilde{l}_x$ as follows. $\tilde{Q}_{\rm ext}/T$ basically follows the information-thermodynamic dissipation $\tilde{\sigma}_x$ especially in the fast rotation regime. On the other hand, in the slow rotation regime, the learning rate $\tilde{l}_x$ compensates for the decrease of $\tilde{\sigma}_x$. As a result, the external heat dissipation $\tilde{Q}_{\rm ext}/T$ becomes almost constant for all the velocity regime.

We find that this decomposition of the heat dissipation is useful to understand its dependence on the external force. Interestingly, when the external force is applied against the free rotation, only the information-thermodynamic dissipation decreases while the learning rate remains almost constant as shown in Fig. A.2(b). Indeed, the analytical expression of the learning rate in the slow switching limit (Eq. (A.17)) is independent of the external force. This result suggests that the information-thermodynamic efficiencies increase as we apply the external force, and even the negative internal heat dissipation can be realized since $\tilde{Q}_{\rm int}/T \sim \tilde{l}_n = -\tilde{l}_x$ when $\tilde{\sigma}_n \sim 0$.

In Fig. A.3, we investigate these points in detail. In Fig. A.3(a), we show the relation between the time scale ratio and the behavior of the internal heat dissipation, the learning rate of n, and the velocities $v(W)$ and $v(\Gamma)$ (see Sec. A.4.1 for the derivation of the time scale ratio $\Gamma W/k$, and the discussion on the equivalence of changing Γ and W). Here, $v(W)$ (resp. $v(\Gamma)$) denotes the velocity when W (resp. Γ) is varied. As expected, the internal heat dissipation becomes negative in the slow switching or the fast diffusion limit ($\Gamma \to 0$). We note that although unnormalized $\dot{Q}_{\rm int}$ vanishes in the slow switching limit, $\dot{Q}_{\rm int}$ can take a strictly negative value in the fast diffusion limit, since the velocity $v(\Gamma)$ does not vanish in this limit.

In Fig. A.3(b) and (c), we show the relation between the time scale ratio and the information-thermodynamic efficiencies. Since the reaction-diffusion model has been verified with experimental data only in the green shaded region, we show the results around this region. As expected, we find that the information-thermodynamic efficiencies increase when the external force is applied. Especially, $\eta_n > 0$ holds for most of the region, which means that the internal heat dissipation becomes negative $\tilde{Q}_{\rm int} < 0$.

A.4 Analytical results

In this section, we show the results of the analytical calculation using the time scale separation. We also show that the Stokes efficiency proposed in the context of molecular motors [146, 153] is related to the short-time TUR.

A.4.1 Time scale separation

First, we explain that $\Gamma W/k$ determines the time scale ratio between x and n [147]. We start from the Fokker-Planck equation of the reaction-diffusion model:

$$\begin{aligned}\frac{\partial}{\partial t}p_t(n,x) &= R^+_{n-1}(x)p_t(n-1,x)+R^-_{n+1}(x)p_t(n+1,x)-(R^+_n(x)+R^-_n(x))p_t(n,x)\\ &\quad+\frac{1}{\Gamma}\frac{\partial}{\partial x}\left\{\left(\frac{\partial}{\partial x}U_n(x)+F\right)p_t(n,x)+T\frac{\partial}{\partial x}p_t(n,x)\right\},\end{aligned} \tag{A.18}$$

where the time dependence of the probability density is written explicitly. We non-dimensionalize the equation by replacing the variables as $\tilde{t}=Wt$, $\tilde{x}=x/l_v$:

$$\begin{aligned}\frac{\partial}{\partial \tilde{t}}p_t(n,x) &= f^+_{n-1}(x)p_t(n-1,x)+f^-_{n+1}(x)p_t(n+1,x)-(f^+_n(x)+f^-_n(x))p_t(n,x)\\ &\quad+\frac{1}{\varepsilon}\frac{\partial}{\partial \tilde{x}}\left\{\frac{l_v^2}{T}\left[k\left(\tilde{x}-\frac{Ln}{l_v}\right)+\frac{F}{l_v}\right]p_t(n,x)+\frac{\partial}{\partial \tilde{x}}p_t(n,x)\right\},\end{aligned} \tag{A.19}$$

where l_v is a typical length scale, and ε and $f^\pm_n(x)$ are defined as $\varepsilon := \Gamma W l_v^2/T$ and $f^\pm_n(x) := R^\pm_n(x)/W$. We can see that ε determines the time scale ratio between x and n, and get $\varepsilon = \Gamma W/k$ by choosing $l_v=\sqrt{T/k}$. Since Γ and W appear only at ε in Eq. (A.19), the information-thermodynamic quantities depend on Γ and W in the same manner when they are normalized (see Fig. A.3).

In the following, we show the analytical calculation of the model in the slow and the fast switching limits.

Slow switching limit

In the slow switching limit $W\to 0$, the rotational degree of freedom equilibrates. In this case, the conditional probability density $p(x|n)$ is given by

$$p(x|n)=\sqrt{\frac{k}{2\pi T}}\exp\left[-\frac{1}{T}U_n(x)\right], \tag{A.20}$$

and the probability $p(n)$ obeys an effective master equation with rates $\overline{R^+_n}$ and $\overline{R^-_n}$ given by

$$\overline{R^+_n} = \int R^+_n(x)p(x|n)\mathrm{d}x = W\exp\left[\frac{kL^2}{2T}q(q-1)+\frac{\Delta\mu}{T}q\right], \tag{A.21}$$

$$\overline{R^-_n} = \int R^-_n(x)p(x|n)\mathrm{d}x = W\exp\left[\frac{kL^2}{2T}q(q-1)+\frac{\Delta\mu}{T}(q-1)\right], \tag{A.22}$$

which are independent of the internal state n. We can calculate the learning rate l_n using the conditional probability density as

$$l_n=-\sum_n\int \mathrm{d}x\Lambda_n(x)\ln\frac{p(x|n)}{p(x|n+1)}=3v\frac{kL^2}{2T}(2q-1), \tag{A.23}$$

where v is the rotational velocity obtained as

$$v = p(n)\overline{R_n^+} - p(n+1)\overline{R_{n+1}^-} \tag{A.24}$$

$$= \frac{W}{3}\exp\left[\frac{kL^2}{2T}q(q-1)\right]e^{q\frac{\Delta\mu}{T}}\left(1-e^{-\frac{\Delta\mu}{T}}\right). \tag{A.25}$$

In addition, we can show that $\tilde{\sigma}_x = 0$ holds regardless of the potential shape in this limit. This can be derived by calculating σ_n as

$$\sigma_n = \frac{\dot{Q}_{\rm int}}{T} - l_n \tag{A.26a}$$

$$= \sum_n \int \mathrm{d}x \Lambda_n(x)\left\{\frac{1}{T}\left[U_n(x) - U_{n+1}(x) + \Delta\mu\right] + \ln\frac{p(x|n)}{p(x|n+1)}\right\} \tag{A.26b}$$

$$= \sum_n \int \mathrm{d}x \Lambda_n(x)\left\{\frac{1}{T}\left[U_n(x) - U_{n+1}(x) + \Delta\mu\right] + \frac{1}{T}\left[U_{n+1}(x) - U_n(x)\right]\right\} \tag{A.26c}$$

$$= 3v\frac{\Delta\mu}{T}, \tag{A.26d}$$

and by using the first law $\sigma_x + \sigma_n = 3v\Delta\mu/T$, where $F = 0$ is assumed for simplicity. We note that $\tilde{\sigma}_x = 0$ is not so trivial, since this is a normalized quantity and it means $\sigma_x \propto v^\alpha$ with $\alpha > 1$, which cannot be derived from the time scale separation straightforwadly.

Fast switching limit

In the fast switching limit $W \to \infty$, the internal degree of freedom equilibrates. In this case, the conditional probability $p(n|x)$ is given by

$$p(n|x) = \frac{\exp\left\{-[U_n(x) - n\Delta\mu]/T\right\}}{\sum_{m=-1}^{m=1}\exp\left\{-[U_n(x) - (n+m)\Delta\mu]/T\right\}}. \tag{A.27}$$

As a result, the local flux vanishes $\Lambda_n(x) = 0$, which leads to the vanishing of the information-thermodynamic quantities $\sigma_n = l_n = l_x = 0$. Thus, $\tilde{\sigma}_n = 0$ holds regardless of the potential shape.

The dynamics of x is described by an overdamped Langevin equation under the effective conservative force F^* given by

$$F^*(x) = \sum_n p(n|x)\frac{\partial U_n(x)}{\partial x}. \tag{A.28}$$

The saturation velocity $v_{\max}$ can be calculated using the effective Langevin equation. It is clear that $v_{\max}$ remains finite in the fast switching limit $W \to \infty$ because the diffusion takes finite time.

A.4.2 Stokes efficiency

Here, we show the relation between the Stokes efficiency [146, 153] and the short-time TUR. We note that the results in this subsection are independent of the main results in

this chapter.

In the reaction-diffusion model, the Stokes efficiency η_S is defined by [146]

$$\eta_S := -\frac{kL\langle y\rangle}{\Delta\mu}, \tag{A.29}$$

where $y := x - nL$ is the relative position from the potential center. It has been shown that η_S satisfies $\eta_S \leq 1$ in the absence of the external force [153]. However, the meaning of the Stokes efficiency may not be clear compared to the other efficiencies such as η_x, since its thermodynamic origin is not very clear.

We find that the Stokes efficiency is a combination of the short-time TUR and the second law of information thermodynamics. Concretely, we can derive the Stokes efficiency on the basis of the following inequality:

$$\begin{aligned} 2\langle\dot{x}\rangle^2 &\leq \mathrm{d}t\mathrm{Var}(\dot{x})\sigma_x & \text{(A.30)}\\ &\leq \mathrm{d}t\mathrm{Var}(\dot{x})\frac{3v\Delta\mu}{T}, & \text{(A.31)} \end{aligned}$$

where we used the short-time TUR in the first line, and $\sigma_n \geq 0$ in the second line. Then, we can derive the Stokes efficiency as

$$\begin{aligned} \frac{2\langle\dot{x}\rangle^2}{\mathrm{d}t\mathrm{Var}(\dot{x})}\frac{T}{3v\Delta\mu} &= -6vL\frac{k\langle y\rangle}{\Gamma}\frac{\Gamma}{2T}\frac{T}{3v\Delta\mu} & \text{(A.32)}\\ &= -\frac{kL\langle y\rangle}{\Delta\mu} & \text{(A.33)}\\ &= \eta_S, & \text{(A.34)} \end{aligned}$$

where we used $\mathrm{d}t\mathrm{Var}(\dot{x}) = 2T/\Gamma$ and $\langle\dot{x}\rangle = -k\langle y\rangle/\Gamma = 3vL$. Thus, $\eta_S \leq 1$ holds.

A.5 Conclusions

In this appendix, we study information thermodynamics of F_1. We investigate the rotational velocity versus the information-thermodynamic quantities in Fig. A.2, and the time scale ratio versus the information-thermodynamic efficiencies in Fig. A.3. We find that the rotational degree of freedom behaves as Maxwell's demon, which leads to a small amount of internal heat dissipation. We also find that the information-thermodynamic efficiencies increase by the external force, and as a result even the negative internal heat dissipation is realized.

Since we can estimate the information-thermodynamic dissipation by the method developed in Chap. 5, these results can be experimentally tested. Furthermore, we can even estimate the learning rate by using the heat dissipation already obtained in the previous studies [50, 89]. Therefore, this is an interesting future issue, which can validate both the estimation method and the reaction-diffusion model.

Bibliography

[1] C. Jarzynski, Phys. Rev. Lett. **78**, 2690 (1997).

[2] G. E. Crooks, Phys. Rev. E **60**, 2721 (1999).

[3] C. Jarzynski, J. Stat. Phys. **98**, 77 (2000).

[4] T. Hatano and S. Sasa, Phys. Rev. Lett. **86**, 3463 (2001).

[5] K. Sekimoto, *Stochastic Energetics* (Springer, 2010).

[6] U. Seifert, Rep. Prog. Phys. **75**, 126001 (2012).

[7] I. A. Martínez, É. Roldán, L. Dinis, D. Petrov, J. M. R. Parrondo, and R. A. Rica, Nat. Phys. **12**, 67 (2016).

[8] M. Esposito, K. Lindenberg, and C. Van den Broeck, EPL **85**, 60010 (2009).

[9] U. Seifert, EPJ E **34**, 26 (2011).

[10] P. Gaspard, J. Chem. Phys. **120**, 8898 (2004).

[11] T. Schmiedl and U. Seifert, J. Chem. Phys. **126**, 44101 (2007).

[12] J. Liphardt, S. Dumont, S. B. Smith, I. Tinoco, and C. Bustamante, Science **296**, 1832 (2002).

[13] G. M. Wang, E. M. Sevick, E. Mittag, D. J. Searles, and D. J. Evans, Phys. Rev. Lett. **89**, 50601 (2002).

[14] D. Collin, F. Ritort, C. Jarzynski, S. B. Smith, I. Tinoco, and C. Bustamante, Nature **437**, 231 (2005).

[15] T. Sagawa and M. Ueda, Phys. Rev. Lett. **100**, 080403 (2008).

[16] T. Sagawa and M. Ueda, Phys. Rev. Lett. **104**, 090602 (2010).

[17] J. M. Horowitz and S. Vaikuntanathan, Phys. Rev. E **82**, 61120 (2010).

[18] T. Sagawa and M. Ueda, Phys. Rev. Lett. **109**, 180602 (2012).

[19] J. M. Horowitz and M. Esposito, Phys. Rev. X **4**, 031015 (2014).

[20] J. M. Horowitz and H. Sandberg, New J. Phys. **16**, 125007 (2014).

[21] J. M. R. Parrondo, J. M. Horowitz, and T. Sagawa, Nat. Phys. **11**, 131 (2015).

[22] J. C. Maxwell, *Theory of Heat* (Appleton London, 1871).

[23] L. Szilard, Zeitschrift für Physik **53**, 840 (1929).

[24] S. Toyabe, T. Sagawa, M. Ueda, E. Muneyuki, and M. Sano, Nat. Phys. **6**, 988 (2010).

[25] A. Bérut, A. Arakelyan, A. Petrosyan, S. Ciliberto, R. Dillenschneider, and E. Lutz, Nature **483**, 187 (2012).

[26] J. V. Koski, V. F. Maisi, J. P. Pekola, and D. V. Averin, P. Natl. Acad. Sci. USA **111**, 13786 (2014).

[27] J. Koski, A. Kutvonen, I. Khaymovich, T. Ala-Nissila, and J. Pekola, Phys. Rev. Lett. **115**, 260602 (2015).

[28] S. Ciliberto, Phys. Rev. X **7**, 21051 (2017).

[29] G. Paneru, S. Dutta, T. Sagawa, T. Tlusty, and H. K. Pak, Nat. Commun. **11**, 1012 (2020).

[30] A. E. Allahverdyan, D. Janzing, and G. Mahler, J. Stat. Mech. P09011 (2009).

[31] S. Ito and T. Sagawa, Phys. Rev. Lett. **111**, 180603 (2013).

[32] N. Shiraishi, S. Ito, K. Kawaguchi, and T. Sagawa, New J. Phys. **17**, 045012 (2015).

[33] D. Hartich, A. C. Barato, and U. Seifert, Phys. Rev. E **93**, 022116 (2016).

[34] T. Matsumoto and T. Sagawa, Phys. Rev. E **97**, 042103 (2018).

[35] A. C. Barato and U. Seifert, Phys. Rev. Lett. **114**, 158101 (2015).

[36] T. R. Gingrich, J. M. Horowitz, N. Perunov, and J. L. England, Phys. Rev. Lett. **116**, 120601 (2016).

[37] J. M. Horowitz and T. R. Gingrich, Phys. Rev. E **96**, 020103(R) (2017).

[38] J. M. Horowitz and T. R. Gingrich, Nat. Phys. **16**, 15 (2019).

[39] D. S. Seara, V. Yadav, I. Linsmeier, A. P. Tabatabai, P. W. Oakes, S. M. A. Tabei, S. Banerjee, and M. P. Murrell, Nat. Commun. **9**, 4948 (2018).

[40] C. Battle, C. P. Broedersz, N. Fakhri, V. F. Geyer, J. Howard, C. F. Schmidt, and F. C. MacKintosh, Science **352**, 604 (2016).

[41] J. C. Kimmel, A. Y. Chang, A. S. Brack, and W. F. Marshall, PLoS Comput. Biol. **14**, e1005927 (2018).

[42] J. M. Horowitz, J. Chem. Phys. **143**, 044111 (2015).

[43] T. R. Gingrich, G. M. Rotskoff, and J. M. Horowitz, J. Phys. A Math. Theor. **50**, 184004 (2017).

[44] J. Li, J. M. Horowitz, T. R. Gingrich, and N. Fakhri, Nat. Commun. **10**, 1666 (2019).

[45] S. K. Manikandan, D. Gupta, and S. Krishnamurthy, Phys. Rev. Lett. **124**, 120603 (2020).

[46] R. E. Spinney and I. J. Ford, Phys. Rev. E **85**, 051113 (2012).

[47] H. Risken, *The Fokker-Planck Equation* (Springer, 1996).

[48] N. Shiraishi and T. Sagawa, Phys. Rev. E **91**, 012130 (2015).

[49] M. L. Rosinberg and J. M. Horowitz, EPL **116**, 10007 (2016).

[50] S. Toyabe, T. Okamoto, T. Watanabe-Nakayama, H. Taketani, S. Kudo, and E. Muneyuki, Phys. Rev. Lett. **104**, 198103 (2010).

[51] A. Dechant and S. Sasa, J. Stat. Mech. 063209 (2018).

[52] P. Pietzonka, F. Ritort, and U. Seifert, Phys. Rev. E **96**, 012101 (2017).

[53] T. Van Vu and Y. Hasegawa, Phys. Rev. E **100**, 32130 (2019).

[54] J. S. Lee, J.-M. Park, and H. Park, Phys. Rev. E **100**, 062132 (2019).

[55] G. Paneru, S. Dutta, T. Tlusty, and H. K. Pak, Phys. Rev. E **102**, 032126 (2020).

[56] L. P. Fischer, H.-M. Chun, and U. Seifert, Phys. Rev. E **102**, 012120 (2020).

[57] T. V. Vu and Y. Hasegawa, J. Phys. A Math. Theor. **53**, 075001 (2019).

[58] P. P. Potts and P. Samuelsson, Phys. Rev. Lett. **124**, 120603 (2019).

[59] A. C. Barato and U. Seifert, Phys. Rev. X **6**, 41053 (2016).

[60] A. C. Barato, R. Chetrite, A. Faggionato, and D. Gabrielli, New J. Phys. **20**, 103023 (2018).

[61] T. Koyuk, U. Seifert, and P. Pietzonka, J. Phys. A Math. Theor. **52**, 02LT02 (2019).

[62] K. Proesmans and C. Van Den Broeck, EPL **119**, 20001 (2017).

[63] S. Pigolotti, I. Neri, É. Roldán, and F. Jülicher, Phys. Rev. Lett. **119**, 140604 (2017).

[64] A. Dechant and S. Sasa, P. Natl. Acad. Sci. USA **117**, 6430 (2020).

[65] A. Dechant, J. Phys. A Math. Theor. **52**, 035001 (2019).

[66] Y. Hasegawa and T. Van Vu, Phys. Rev. E **99**, 62126 (2019).

[67] Y. Hasegawa and T. Van Vu, Phys. Rev. Lett. **123**, 110602 (2019).

[68] G. Falasco, M. Esposito, and J.-C. Delvenne, New J. Phys. **22**, 053046 (2020).

[69] K. Liu, Z. Gong, and M. Ueda, Phys. Rev. Lett. **125**, 140602 (2020).

[70] V. T. Vo, T. Van Vu, and Y. Hasegawa, Phys. Rev. E **102**, 062132 (2020).

[71] A. Dechant and S. Sasa, Phys. Rev. E **97**, 062101 (2018).

[72] S. Ito, Phys. Rev. Lett. **121**, 30605 (2018).

[73] S. Ito and A. Dechant, Phys. Rev. X **10**, 021056 (2020).

[74] D. H. Wolpert, Phys. Rev. Lett. **125**, 200602 (2020).

[75] A. M. Timpanaro, G. Guarnieri, J. Goold, and G. T. Landi, Phys. Rev. Lett. **123**, 090604 (2019).

[76] P. Pietzonka, A. C. Barato, and U. Seifert, J. Stat. Mech. 124004 (2016).

[77] P. Pietzonka and U. Seifert, Phys. Rev. Lett. **120**, 190602 (2018).

[78] T. Koyuk and U. Seifert, Phys. Rev. Lett. **122**, 230601 (2019).

[79] J. M. R. Parrondo, Phys. Rev. E **57**, 7297 (1998).

[80] R. D. Astumian, P. Natl. Acad. Sci. USA **104**, 19715 (2007).

[81] N. A. Sinitsyn and I. Nemenman, EPL **77**, 58001 (2007).

[82] L. Bertini, A. Faggionato, and D. Gabrielli, Stoch. Process Their Appl. **125**, 2786 (2015).

[83] C. Gardiner, *Stochastic Methods* (Springer, 2009).

[84] N. Shiraishi, K. Saito, and H. Tasaki, Phys. Rev. Lett. **117**, 190601 (2016).

[85] D. M. Busiello and S. Pigolotti, Phys. Rev. E **100**, 060102, (2019).

[86] T. Harada and S. Sasa, Phys. Rev. Lett. **95**, 130602 (2005).

[87] T. Harada and S. Sasa, Phys. Rev. E **73**, 26131 (2006).

[88] S. Toyabe, H.-R. Jiang, T. Nakamura, Y. Murayama, and M. Sano, Phys. Rev. E **75**, 11122 (2007).

[89] S. Toyabe and E. Muneyuki, New J. Phys. **17**, 015008 (2015).

[90] T. Ariga, M. Tomishige, and D. Mizuno, Phys. Rev. Lett. **121**, 218101 (2018).

[91] D. Mizuno, C. Tardin, C. F. Schmidt, and F. C. MacKintosh, Science **315**, 370 (2007).

[92] B. Lander, J. Mehl, V. Blickle, C. Bechinger, and U. Seifert, Phys. Rev. E **86**, 030401(R) (2012).

[93] A. Frishman and P. Ronceray, Phys. Rev. X **10**, 21009 (2020).

[94] I. Roldán and J. M. Parrondo, Phys. Rev. Lett. **105**, 150607 (2010).

[95] I. A. Martínez, G. Bisker, J. M. Horowitz, and J. M. Parrondo, Nat. Commun. **10**, 3542 (2019).

[96] D. J. Skinner and J. Dunkel, arXiv:2011.08765 (2020).

[97] A. W. Bowman and A. Azzalini, *Applied Smoothing Techniques for Data Analysis: The Kernel Approach with S-Plus Illustrations*, Vol. 18 (OUP Oxford, 1997).

[98] T. M. Cover and J. A. Thomas, *Elements of Information Theory* (Wiley-Interscience, 2006).

[99] S. K. Manikandan and S. Krishnamurthy, J. Phys. A Math. and Theor. **51**, 11LT01 (2018).

[100] S. Otsubo, S. Ito, A. Dechant, and T. Sagawa, Phys. Rev. E **101**, 062106 (2020).

[101] K. Diederik and J. L. Ba, arXiv:1412.6980 (2014).

[102] T. Van Vu, V. T. Vo, and Y. Hasegawa, Phys. Rev. E **101**, 042138 (2020).

[103] F. Ritort, Journal of Physics: Condensed Matter **18**, R531 (2006).

[104] S. Otsubo, S. K. Manikandan, T. Sagawa, and S. Krishnamurthy, arXiv:2010.03852 (2020).

[105] F. Tostevin and P. R. Ten Wolde, Phys. Rev. Lett. **102**, 218101 (2009).

[106] G. Lan, P. Sartori, S. Neumann, V. Sourjik, and Y. Tu, Nat. Phys. **8**, 422 (2012).

[107] A. Goldbeter, Nature **420**, 238 (2002).

[108] U. Alon, *An Introduction to Systems Biology* (CRC Press, 2006).

[109] S. Zambrano, I. De Toma, A. Piffer, M. E. Bianchi, and A. Agresti, eLife **5**, e09100 (2016).

[110] T. Koyuk and U. Seifert, Phys. Rev. Lett. **125**, 260604 (2020).

[111] D.-K. Kim, Y. Bae, S. Lee, and H. Jeong, Phys. Rev. Lett. **125**, 140604 (2020).

[112] A. Keziou, Comptes Rendus Mathematique **336**, 857 (2003).

[113] X. Nguyen, M. J. Wainwright, and M. I. Jordan, IEEE Trans. Inf. Theory **56**, 5847 (2010).

[114] M. I. Belghazi, A. Baratin, S. Rajeshwar, S. Ozair, Y. Bengio, A. Courville, and D. Hjelm. Proceedings of Machine Learning Research (PMLR, Stockholmsmässan, Stockholm, Sweden, 2018), pp. 531.-540

[115] A. Ruderman, M. D. Reid, D. García-García, and J. Petterson. Proceedings of the 29th International Conference on International Conference on Machine Learning (Omnipress, Madison, WI, USA, 2012), pp. 1155-1162.

[116] K. Hornik, M. Stinchcombe, and H. White, Neural Netw. **2**, 359 (1989).

[117] T. Moon, S. Hong, H. Y. Choi, D. H. Jung, S. H. Chang, and J. E. Son, Comput. Electron. Agric **166**, 105023 (2019).

[118] K. P. Murphy, *Machine learning: a probabilistic perspective* (Cambridge, MA:MIT Press, 2012).

[119] S. Ito and T. Sagawa, Nat. Commun. **6**, 7498 (2015).

[120] D. M. Carberry, J. C. Reid, G. M. Wang, E. M. Sevick, D. J. Searles, and D. J. Evans, Phys. Rev. Lett. **92**, 140601 (2004).

[121] S. K. Manikandan and S. Krishnamurthy, EPJ B **90**, 258 (2017).

[122] K. Nakamura and T. J. Kobayashi, arXiv:2005.13208 (2020).

[123] S. Ramaswamy, Annu. Rev. Condens. Matter Phys. **1**, 323 (2010).

[124] F. S. Gnesotto, G. Gradziuk, P. Ronceray, and C. P. Broedersz, Nat. Commun. **11**, 5378 (2020).

[125] M. Esposito, Phys. Rev. E **85**, 041125 (2012).

[126] K. Kawaguchi and Y. Nakayama, Phys. Rev. E **88**, 022147 (2013).

[127] R. W. Zwanzig, J. Chem. Phys. **22**, 1420 (1954).

[128] C. Jarzynski, Phys. Rev. E **65**, 046122 (2002).

[129] P. Wirnsberger, A. J. Ballard, G. Papamakarios, S. Abercrombie, S. Racaniére, A. Pritzel, D. J. Rezende, and C. Blundell, J. Chem. Phys. **153**, 144112 (2020).

[130] S. Otsubo, C.-B. Li, S. Bo, and T. Sagawa, Manuscript in preparation (2021).

[131] S. Otsubo and T. Sagawa, arXiv:1803.04217 (2018).

[132] S. Bo, M. D. Giudice, and A. Celani, J. Stat. Mech. P01014 (2015).

[133] T. E. Ouldridge, C. C. Govern, and P. R. ten Wolde, Phys. Rev. X **7**, 21004 (2017).

[134] P. D. Boyer, Biochim. Biophys. Acta **1140**, 215 (1993).

[135] R. D. Vale, Cell **112**, 467 (2003).

[136] P. D. Boyer, Annu. Rev. Biochem. **66**, 717 (1997).

[137] J. P. Abrahams, A. G. W. Leslie, R. Lutter, and J. E. Walker, Nature **370**, 621 (1994).

[138] H. Noji, R. Yasuda, M. Yoshida, and K. Kinosita, Nature **386**, 299 (1997).

[139] R. Yasuda, H. Noji, K. J. Kinosita, and M. Yoshida, Cell **93**, 1117 (1998).

[140] H. Itoh, A. Takahashi, K. Adachi, H. Noji, R. Yasuda, and M. Yoshida, Nature **427**, 465 (2004).

[141] Y. Rondelez, G. Tresset, T. Nakashima, Y. Kato-Yamada, H. Fujita, S. Takeuchi, and H. Noji, Nature **433**, 773 (2005).

[142] E.-i. Saita, T. Suzuki, K. Kinosita, and M. Yoshida, P. Natl. Acad. Sci. USA **112**, 9626 (2015).

[143] N. Soga, K. Kimura, K. Kinosita, M. Yoshida, and T. Suzuki, P. Natl. Acad. Sci. USA **114**, 4960 (2017).

[144] S. Toyabe, T. Watanabe-Nakayama, T. Okamoto, S. Kudo, and E. Muneyuki, P. Natl. Acad. Sci. USA **108**, 17951 (2011).

[145] H. Wang and G. Oster, Nature **396**, 279 (1998).

[146] E. Zimmermann and U. Seifert, New J. Phys. **14**, 103023 (2012).

[147] K. Kawaguchi, S. Sasa, and T. Sagawa, Biophysical Journal **106**, 2450 (2014).

[148] R. Yasuda, H. Noji, M. Yoshida, K. Kinosita, and H. Itoh, Nature **410**, 898 (2001).

[149] Y. Hirono-Hara, H. Noji, M. Nishiura, E. Muneyuki, K. Y. Hara, R. Yasuda, K. Kinosita, and M. Yoshida, P. Natl. Acad. Sci. USA **98**, 13649 (2001).

[150] R. Watanabe, D. Okuno, S. Sakakihara, K. Shimabukuro, R. Iino, M. Yoshida, and H. Noji, Nat. Chem. Biol. **8**, 86 (2012).

[151] K. Adachi, K. Oiwa, M. Yoshida, T. Nishizaka, and K. Kinosita, Nat. Commun. **3**, 1022 (2012).

[152] C.-B. Li, H. Ueno, R. Watanabe, H. Noji, and T. Komatsuzaki, Nat. Commun. **6**, 10223 (2015).

[153] H. Wang and G. Oster, EPL **57**, 134 (2002).